PERFORMANCE COMPARISON OF FUNCTIONAL AND EFFECTIVE BRAIN CONNECTIVITY METHODS

Robert Spangler
Dipl.-Math. (FH)

Submitted in fulfilment of the requirements for the
Degree of Doctor of Philosophy

Institute of Neuroscience & Psychology
College of Medical, Veterinary & Life Sciences
University of Glasgow

May 2020

Abstract

Functional and effective connectivity estimates based on electroencephalography (EEG) and magnetoencephalography (MEG) are widely used to understand and reveal new insight into the dynamic behaviour of the brain. However, with a large number of different connectivity methods that are currently available, there is a lack of systematic comparative studies including a statistical evaluation of their performance to understand the strengths and shortcomings of competing methods.

Here, we present a simulation framework to evaluate and compare the performance of connectivity estimators on simulated, yet realistic electromagnetic recordings. We assess the ability of various methods to reconstruct cortical networks, while systematically varying specific parameters which are of significant importance during the simulation, preprocessing or inverse source reconstruction of realistic EEG recordings. A decisive advantage of this simulation framework, when compared with models utilised in other studies, is the integration of volume conduction artifacts. This is achieved by modelling the propagation of electric or magnetic fields from an electric primary current source through biological tissue towards measurement sensors. Subsequently, inverse source reconstruction approaches are applied to estimate the temporal activity patterns of underlying network nodes. The implementation of these concepts enabled the analysis of parameters involved during forward modelling and source reconstruction which may affect the estimation of connectivity on the source level.

The experiments carried out in this work unfold the behaviour of estimators regarding the effect of signal-to-noise ratio (SNR), length of data sets, various phase shifts between correlated signals, the impact of regularization used in inverse source reconstruction, errors in the localization and varying network sizes. For each simulation, strengths and weaknesses of methods are pointed out. Furthermore, pitfalls and obstacles researchers might come across when applying particular estimators on EEG recordings are discussed.

Building on the insight gained from simulation studies, the final part of the thesis analyses the performance of connectivity estimators when applied to resting-state EEG recordings. Network reconstructions with priority on the alpha frequency band reveal a default-mode-network (DMN) with dominant posterior-to-anterior information flow. We detected no significant variations in the amount of correctly identified network links between

connectivity methods. However, we discuss differences in connectivity spectra that emerged, which affect the interpretability and applicability of methods.

Contents

List of Tables

List of Figures

List of Abbreviations

AAL	Automated Anatomical Labeling
ADC	Analog to Digital Converter
AIC	Akaike Information Criterion
ANOVA	Analysis of Variance
AR	Autoregressive
AUC	Area Under Curve
BEM	Boundary Element Method
BIC	Bayesian Information Criterion
BOLD	Blood-Oxygen-Level Dependent
CLARA	Classical LORETA Analysis Recursively Applied
CMS	Common Mode Sense
COR	Correlation
CR	Conductivity Ratio
CSD	Cross-Spectral Density
CSF	Cerebrospinal Fluid
dDTF	direct Directed Transfer Function
DICS	Dynamic Imaging of Coherent Sources
dMRI	Diffusion Magnetic Resonance Imaging
DTF	Directed Transfer Function
DTI	Diffusion Tensor Imaging

EC	Effective Connectivity
EEG	Electroencephalography
eLORETA	Exact Low Resolution Tomography
FC	Functional Connectivity
FEM	Finite Element Method
ffDTF	full frequency Directed Transfer Function
fMRI	functional Magnetic Resonance Imaging
FPE	Akaike Final Prediction Error Criterion
FPR	False Positive Rate
GABA	γ-Aminobutyric Acid
GC	Granger Causality
H	Transfer Function
hdEEG	High-Density EEG
Hz	Hertz
IQR	Interquartile Range
LCMV	Linearly Constrained Minimum Variance
LFP	Local Field Potentials
LORETA	Low Resolution Electromagnetic Tomography
MEG	Magnetoencephalography
MNE	Minimum-Norm Estimate
MRI	Magnetic Resonance Imaging
MVAR	Multivariate Autoregressive
NMM	Neural Mass Model
PDC	Partial Directed Coherence
PET	Positron Emission Tomography

PLV	Phase-Locking Value
PTE	Phase Transfer Entropy
RC	Regularization Constant
RG	Region Growing
ROC	Receiver Operating Characteristic
ROI	Region of Interest
RSN	Resting-State Network
S-FLEX	Sparse Basis Field Expansions
SaM	Split-and-Merge
SC	Structural Connectivity
SNR	Signal-to-Noise Ratio
sPDC	squared Partial Directed Coherence
SSLOFO	Standardized Shrinking LORETA-FOCUSS
T	Cycle Length
TFree	Threshold free approach
TMax	Maximum connectivity thresholds
TMean	Mean connectivity thresholds
TPR	True Positive Rate
TRGC	Time Reversed Granger Causality
TSVD	Truncated Singular Value Decomposition

Acknowledgements

Undertaking this PhD has been a tremendous experience for me and it would not have been possible to accomplish without a great deal of support and guidance that I received from many people.

I would like to thank my thesis supervisor Professor Dr. Joachim Gross for his support, advice and patience during the entire course of my PhD studies. The door to Joachims' office was always open whenever I faced difficulties or had a question about my research or writing. When working from abroad, he was just a Skype call away to help me with valuable suggestions and comments to improve my research and thesis.
I would also like to express my gratitude to Professor Dr. Christoph Kayser as the second supervisor of my thesis, and I am thankful for his valuable comments on this work.

I would like to thank the BESA GmbH, and in particular Dr. Tobias Scherg, for giving me the opportunity to accept a PhD position while working for BESA and to provide the funding for my PhD.

My deep appreciation goes out to my colleagues from the "Research" team at BESA: Abinash, Andre, Harald, Jae-Hyun, and Mateusz. Thank you for your excellent help and your assistance that have made an invaluable contribution towards my PhD In particular, I also want to thank my former colleagues Isabella and Todor who convinced me that I should pursue my doctoral degree and supported me to obtain this PhD position at the University of Glasgow.

In addition, I would like to thank my friends and family for their support and understanding. Finally I must express my very profound gratitude to Simone, who has been supporting me throughout this PhD and without her, I would not have had the courage and persistence to successfully confront all challenges that I came across during this work.

Author's Declaration

I declare that, except where explicit reference is made to the contribution of others, that this dissertation is the result of my own work and has not been submitted for any other degree at the University of Glasgow or any other institution.

_____

Robert Spangler

Chapter 1

Introduction

1.1 Brain Connectivity Analysis

In recent years, connectivity analysis of neuroimaging data has played a key-role in understanding the structure and organization of the human brain. Constant development in the field of neuroimaging techniques and analytical methods allowed deeper and more comprehensive insights into the complex nature of brain networks and the interaction between specialised populations of neurons. Brain connectivity is based on two central principles that form the functional organization of the brain. These principles are characterized by segregation and integration of information being processed.

Evidence for the proposal that specific functional specialisations are realized by local regions has been presented by a number of studies (Kolb and Whishaw, 1990, Zeki et al., 1991, Caramazza, 1992, Tononi, Sporns, and Edelman, 1994). Particular emphasis may be given to the pioneering work performed by the French researcher Pierre Paul Broca (1824 - 1880). His research led to the first anatomical indications of specialised information processing in local brain structures. During his studies of brains of patients suffering from aphasia, he discovered that lesions in the left frontal region were the cause of the disorder and lead to the subjects inability to comprehend and formulate language. This findings for the specific functional specialisation can be confirmed by a number of studies (Duncan and Owen, 2000, Eickhoff et al., 2007, Amunts et al., 2014) that demonstrate that specific brain areas subserved specific functions.

However, during the last decades, new data have questioned the limitations of that notion and have uncovered more complex mechanisms of the working brain. A prominent example is that a coherent perception of the reality cannot be obtained by a collection of specialised functions alone (Zeki and Shipp, 1988, Tononi, 1998). For that, distributed areas of the brain need to communicate and their information needs to be combined. This principle of coordinated functional integration and information transfer (Sporns, 2013) of local neuronal groups enables the emergence of coherent cognitive and behavioural states.

The synthesis of both principles creates the framework of complex, large-scale brain networks with specialised cortical areas that are strongly connected within themselves, but only share sparse connections to brain areas with different fields of specialisations (Sporns, 2013).

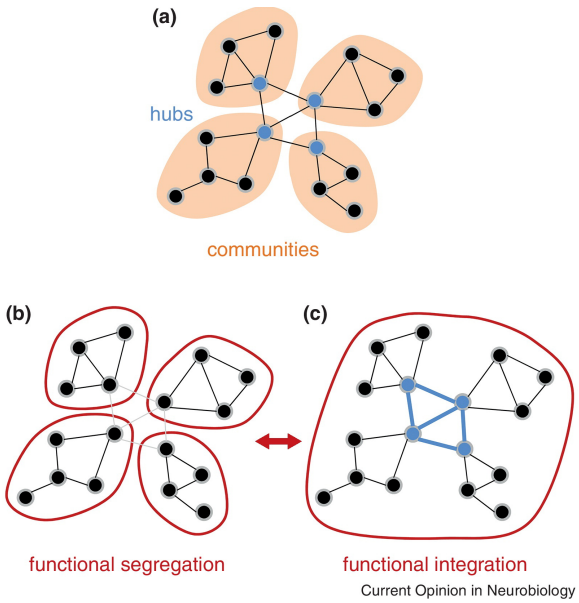

Figure 1: Schematic illustration of a brain network with specialised strongly connected cortical areas (b) and sparse connections to different brain areas (c). Reprinted from Current Opinion in Neurobiology, Volume 23, Issue 2, Sporns Olaf, Network attributes for segregation and integration in the human brain, Pages 162-171, Copyright (2013), with permission from Elsevier.

Modes of brain connectivity of large-scale brain networks are divided up into three separate, but related aspects: structural connectivity, functional connectivity and effective connectivity (Friston, 1994).

- Structural connectivity (SC), also called anatomical connectivity refers to the anatomical structure of the brain. The connections between neighbouring neurons and spatially distant brain regions are defined by white-matter tracts (fibres). These tracks can be measured by diffusion magnetic resonance imaging (dMRI), also referred to as diffusion tensor imaging (DTI).
  The ability to replicate anatomical connections of an individual, living brain, based on non-invasive methods has been a major breakthrough in neuroscience. Recent neuroimaging studies (Iturria-Medina, Sotero, Canales-Rodríguez, Alemán-Gómez, and Melie-García, 2008, Gong et al., 2009) have shown that separate cortical areas are highly connected via an extensive network of pathways.
  The network of synaptic connections is by no means static and invariable, as changes

in the physical pattern of structural links have been observed on longer time scales (hours, days).

- Functional connectivity (FC) is defined as the temporal correlation of spatially separated brain areas. It reveals statistical dependencies between distinct neuronal populations and can be estimated by measuring correlation or covariance, spectral coherence or phase-locking. The listed methods indicate a certain interaction between elements of a network, but are not able to point out the direction of the information flow. However, estimating the direction of information flow is of fundamental importance for the analysis of brain networks and for the identification and distinction of transmitting and receiving network nodes.
  In contrast to structural connectivity, functional connectivity is highly time dependent as statistical dependencies may fluctuate on multiple time scales ranging from milliseconds to seconds.

- Effective connectivity (EC) enhances the information from functional connectivity about statistical dependencies between neuronal areas, as it provides a measure for the directional influence of one neural system over another. Causality can be estimated from network perturbations or time series analysis. EC methods can be divided into two groups: methods that make use of assumptions and are based on an underlying theoretical model and methods that can be seen as model-free. Some techniques also require the definition of structural information to allow estimation of effective connectivity.

The main focus of this thesis is on methods estimating functional or effective connectivity collected from electroencephalography (EEG) and magnetoencephalography (MEG) recordings. To analyse and evaluate interactions between distinct brain regions from the recorded electrophysiological data, neuroscientists face the considerable challenge of selecting a suitable approach from a vast number of functional and effective connectivity methods. Although most of the methods originated from probability theory and related fields to describe certain time-varying stochastic or random processes, some are based on completely different approaches which makes it difficult to compare these methods. Furthermore, each connectivity estimator has its own benefits and limitations and may require specific conditions to be met in order to provide valid and reliable results. Another aggravating aspect are the difficulties with regards to the meaningfulness and interpretability of the outcome of the method applied.
Bearing all this in mind, researchers will find themselves in a situation where they are in need of reliable and comprehensive scientific sources which are meant as guideposts to support them in their decision-making process.

1.2 Critical Discussion

Simulation studies are well suited for this purpose of systematically and objectively evaluating competing existing and newly proposed algorithms. The key challenge in simulating real-world systems is the deliberate choice between appropriate approximations and generalisations of essential features and attributes of the chosen process. In this regard, an introduction of simplifications to eliminate or reduce dependencies is vital in order to focus on particular conditions under which different methods perform better. However, an over-simplification of the real-world model may obscure the fidelity and reliability of simulations and will lead to difficulties to transfer conclusions from simulation results to real-world applications.

This chapter will provide an overview and comparison of selected simulation studies to evaluate the strengths and weaknesses of each study. The publications will be presented in chronological order, beginning with the earliest paper, which was published in 2007 by Ursino et al. (Ursino, Zavaglia, Astolfi, and Babiloni, 2007). This paper consists of a simulation study where cortical activity in several regions of interest (ROI) was modelled based on a neural mass model (NMM) proposed by Wendling et al. (Wendling, Bartolomei, Bellanger, and Chauvel, 2002) and an experimental study to estimate the weights of the synaptic links between six ROIs during a finger-movement task. Although forward modelling and source localization of the simulated cortical activity were not taken into consideration, the analysis process of experimental data could serve as a guideline for a comprehensive simulation study. Inverse source localization of experimental EEG data implied a 4-compartment (brain, skull, scalp and air) boundary element method (BEM; Fuchs, Kastner, Wagner, Hawes, and Ebersole, 2002) to calculate the cortical activation at approximately 3000 source locations. To reduce data dimensionality and calculate waveforms for each region, the activation of sources that are geometrically included in each ROI were averaged. This approach of applying brain parcellation based on atlases or functional magnetic resonance imaging (fMRI) research as a basis for whole-brain connectivity analysis has attracted growing interest in recent years (Fischl et al., 2004, Eickhoff, Thirion, Varoquaux, and Bzdok, 2015, Fan et al., 2016). It offers a promising mechanism to evaluate functional and effective connectivity from results obtained by distributed source analysis methods. In this paper, connectivity strength was estimated via reconstructing the weight of the synaptic link using normalized power spectra. These were computed using Welch's average modified periodogram method (Welch, 1967). Results indicate the possibility of successfully reconstructing NMMs from power spectral densities. However, the estimated connectivity strengths have not been contrasted with results of other connectivity methods, thus making it difficult to assess the performance of the suggested method.

In the same year Astolfi et al. (Astolfi et al., 2007) published a paper that follows the exact same strategy for the generation of the simulated signals using the NMM by Wendling et al. The network incorporates five ROIs, which are sparsely connected by direct as well as indirect links with realistic connection strength values as observed in other studies (Büchel and Friston, 1997). In contrast to the paper by Ursino et al. (Ursino et al., 2007), three estimators of cortical, effective connectivity were applied to retrieve the correlation factors between every pair of ROIs: the directed transfer function (DTF; Kamiński and Blinowska, 1991) and its modification the direct directed transfer function (dDTF; Korzeniewska, Mańczak, Kamiński, Blinowska, and Kasicki, 2003) as well as the partial directed coherence (PDC; Baccalá and Sameshima, 2001). Similar to Ursino et al. (Ursino et al., 2007), connectivity estimation was calculated directly using the simulated waveforms from the NMM without projecting cortical activity to the surface of the scalp and subsequently applying source reconstruction algorithms. To measure the performance of the connectivity estimators in varying conditions, the effects of different SNR levels (variation from 1 to 10) and the length of the datasets (2500 to 15000 samples) was investigated. Fifty repetitions of each simulation scenario were carried out to ensure sufficient robustness of subsequent statistical evaluation using analysis of variance (ANOVA). This detailed statistical evaluation is essential and must be carried out as this allows a qualitative assessment and comparison of methods. For this reason, this publication can serve as a reference for simulation studies, however, only a fairly limited number of connectivity methods was taken into account and the extent of testing potentially significant factors must be expanded.

In 2010, Florin et al. (Florin, Gross, Pfeifer, Fink, and Timmermann, 2010) investigated the effect of filtering, data decimation and interpolation on multiple connectivity estimators: transfer function (H), DTF, dDTF, PDC and squared partial directed coherence (sPDC; Astolfi et al., 2006). In contrast to Ursino et al. (Ursino et al., 2007) and Astolfi et al. (Astolfi et al., 2007), MEG sensor time-series (96 sensors) were modelled based on multivariate autoregressive (MVAR) models as suggested by Kus et al. (Kuś, Kamiński, and Blinowska, 2004). Four different types of filters (Butterworth, Chebyshev I and II and elliptic filters) were applied on the data followed by a statistical analysis using the Mann-Whitney U-test including Bonferroni correction to correct for an increased number of false positives (type I errors) due to multiple comparisons. Although this paper was designed with more emphasis on analysing preprocessing effects on connectivity results, it is worth pointing out the conception and implementation of the simulations as well as the elaborated subsequent statistical evaluation.

In contrast to this, the study presented by Wu et al. (Wu, Frye, and Zouridakis, 2011) focuses entirely on the comparison of multivariate causality measures. Similar to Florin et al. (Florin et al., 2010), MVAR models were used to generate time-series for 3, 7, 10 and 20 source networks. The model order, which defines the number of considered preceding time points

to simulate dependencies between nodes was varied (4, 8, 12 and 16). Moreover, the ratio of direct and indirect connections between nodes was changed to alter the degree of complexity for each network size. Besides these parameters, the influence of SNR was investigated. Connectivity measures considered in this study were Granger Causality (GC; Granger, 1969), DTF, dDTF, PDC, sPDC and full frequency directed transfer function (ffDTF; Korzeniewska et al., 2003). This simulation study is an excellent example for measuring and comparing the impact of multiple parameters on the performance of different connectivity methods. However, there is no reference to any statistical evaluation of connectivity results to add mathematical proof for the significance of findings. Furthermore, like all of the studies introduced so far, Wu et al. (Wu et al., 2011) did not perform forward-modelling of brain activity on the scalp surface and subsequently apply source reconstruction algorithms to recover source waveforms. This step is not necessarily required to compare the performance of connectivity estimators, however this detour involves several problems that also come into play when looking at real EEG and MEG data. One of these problems is referred to as volume conduction (Sarvas, 1987), which causes a smearing effect by propagation of the source signal from the cortex to the outside of the scalp. This is apparently another critical issue for neuroscientics looking for a suitable connectivity method to analyse their data. Therefore, it is vital to take the complexity of inverse source reconstruction into account when designing an appropriate simulation model and not to neglect this problem for reasons of simplification.

A comparable paper was published in 2012 by Silfverhuth et al. (Silfverhuth, Hintsala, Kortelainen, and Seppänen, 2012). The performance of six connectivity estimators, Correlation (COR), magnitude-squared coherence (COH), phase-slope index (PSI; Nolte et al., 2008), DTF, PDC and transfer entropy (TE; Schreiber, 2000) was compared. Equivalent to Wu et al. (Wu et al., 2011) and Florin et al. (Florin et al., 2010), time-courses for the activity pattern of eight ROIs were generated using MVAR models. The effect of SNR (levels 1, 5 and 10) was examined, as well as the influence of the sampling rate starting with a maximum rate of 1000 Hz to down-sampled rates of 500 Hz and 250 Hz. Significance of results was tested by Chi-square tests. However, as already highlighted in the previous section, Silfverhuth et al., 2012 also reconstructed the connectivity pattern directly on the generated source waveforms without forward modelling and inverse source reconstruction.

In contrast to all previously introduced publications, the following studies performed forward modelling to obtain simulated EEG and MEG recordings from known underlying cortical networks. In his PhD thesis, Drakesmith (Drakesmith, 2012) applies a source model that strongly differs from the MVAR and NMM presented so far. He simulated a straightforward cortical network of 1454 dipoles distributed over the whole brain space and oriented orthogonally to the head surface. Gaussian white noise was added to the waveforms of all of these sources to model cortical background activity. Bilateral dipoles

in the two occipital lobes were used to carry 33 Hz sinusoidal waves without any phase lag between the sources. A smoothing factor was applied to smear activity to surrounding dipoles. Forward calculations were performed for 64 electrodes for EEG data using a BEM head model, as well as 148 axial gradiometer sensors for MEG data considering a single-shell head-model. For estimation of coherence across all voxel combinations, dynamic imaging of coherent sources (DICS), introduced by Gross et al. (Gross et al., 2001) was applied. With this approach, the quality of the reconstructed network can be measured by comparing the connectivity matrices of the original, simulated network and the reconstructed network. The resulting statistical indicators true positive rate (TPR) and log false positive rate (FPR) were calculated for a range of thresholds. In order to establish an easy comparison of the calculated statistics, the log receiver-operating characteristics (ROC) curve was created by plotting the TPR against the log FPR and integrated to obtain a single value quantifying the accuracy of each network reconstruction. This statistical approach has the advantage that it can be seen as threshold-free and it also enables the comparability of network reconstructions from various connectivity methods.

A set of simulations has been explored in the paper by Haufe et al. (Haufe, Nikulin, Müller, and Nolte, 2013). This paper covers four experiments that are all based on a source model with two interacting cortical regions. The first experiment deals with the application of connectivity estimators (GC, PDC and PSI) on unmixed time series to examine their performance on noise-free data and also excluding effects of volume conduction. Both of these effects are included in the second experiment, where 10 additional noise sources were added to the model. Forward modelling to calculate the signal of 59 EEG sensors was carried out with a realistically shaped head model (Holmes et al., 1998). For connectivity analysis on sensor level using GC and PDC, either all 59 channels, or only a subset of 19 electrodes were used. The third experiment covers the influence of the chosen reference electrode on connectivity estimators. Therefore, the signal of TP9 or TP10 electrode was subtracted from data generated in the second experiment to re-reference signals. Besides, the influence of noise was evaluated with results from PSI, adding noise of 2 different SNR levels (0.24 and 0.75). Finally, the fourth experiment included three distributed source reconstruction algorithms: weighted minimum norm (WMN; Hämäläinen and Ilmoniemi, 1994), sparse basis field expansions (S-FLEX; Haufe, Nikulin, Ziehe, Müller, and Nolte, 2009) and linearly constrained minimum variance (LCMV) beamforming (Van Veen, Van Drongelen, Yuchtman, and Suzuki, 1997). To reduce the extent of connectivity analysis on distributed source localizations, ROIs were defined by dividing the voxel space in relation to their respective distance to 19 EEG electrode positions.

Reduction of source space via ROIs using a standard anatomical or histological brain atlas or a data-driven technique (Liu, Belliveau, and Dale, 1998, Beckmann, DeLuca, Devlin, and Smith, 2005, Hauk, Wakeman, and Henson, 2011) is a technique that is often applied

to retrieve temporal activity pattern for distinct brain areas (Schoffelen and Gross, 2009, Hassan et al., 2014, Colclough, Brookes, Smith, and Woolrich, 2015, Mahjoory et al., 2017). A recent study by Farahibozorg et al. (Farahibozorg, Henson, and Hauk, 2018) focussed on the effect of different anatomical parcellations on connectivity estimation. In his study, Farahibozorg simulated EEG (70 scalp sensors) and MEG (204 gradiometer, 102 magnetometer) recordings based on cortical networks involving 3, 5, 10 and 15 active nodes. Temporal activity of sources was defined by sinusoidal signals and random noise with a SNR of 1 and 3. A three-shell (scalp, outer skull surface and inner skull surface) BEM head model was used for forward modelling to compute the simulated sensor recordings and during inverse source reconstruction based on $L2$ minimum norm (MNE) estimator with loose orientation constraint (Lin et al., 2004). Subsequently, two adaptive parcellation algorithms, split-and-merge (SaM) and region growing (RG), described by Gonzalez and and Woods (Gonzalez and Woods, 2006) were applied on either different average sizes of brain atlas parcels (Desikan-Killiany, Desikan et al., 2006 and Destrieux, Destrieux, Fischl, Dale, and Halgren, 2010) or without prior parcellation to reduce source space. Significant connections of connectivity spectra estimated from magnitude-squared coherence and imaginary part of Coherency were identified using one-tailed permutation tests. Performance of each method for the underlying parameter set was evaluated by computing true positive and false positive rates. Based on this simulation framework, Farahibozorg analysed the similarity between different parcellation approaches in absence of any significant connectivity patterns and looked at the accuracy of network reconstructions for random source positions and connections. Furthermore, it was examined whether results obtained from non-zero-lag connectivity estimators benefit from data-based parcellation algorithms. This present study addresses the relation between adaptive source space reduction and connectivity estimation in a high level of detail and an extent that has so far been lacking in the literature. The simulation section takes a variety of parameters into account that affect the accuracy and quality of the connectivity methods. However, as mentioned in the paper, the parcellation algorithms are heavily dependent on the EEG/MEG data set, the volume conduction model and the inverse source reconstruction method. Therefore, the results of connectivity estimation and statistical analysis of a simulation study must be viewed in the overall context.

The most-recent paper that was taken into account was published in 2019 by Anzolin et al. (Anzolin et al., 2019). In this paper, a comprehensive simulation pipeline to consolidate research on the effect of source mixing and to demonstrate the effect of source position, SNR level and inverse source reconstruction methods on connectivity estimation is presented. A brain network including three network nodes (sender, receiver and a non-interacting cortical region) was simulated by using MVAR models. Forward modelling to project activity onto 108 EEG sensors and inverse source reconstruction made use of a highly detailed FEM model

(Huang, Parra, and Haufe, 2016). The ICBM-NY, or New York Head model is a standardized volume conductor modelling six different brain tissues (scalp, skull, CSF, gray matter, white matter and air cavities) based on the *ICBM*152 anatomical template (Fonov, Evans, McKinstry, Almli, and Collins, 2009, Fonov et al., 2011). This results in a considerably increased degree of realism of the conducted simulations, leading to more detailed models and a more accurate reproduction of real world applications. Source-waveforms of simulated network sources were reconstructed by applying two distributed inverse source analysis methods: LCMV beamforming and eLORETA (Pascual-Marqui, 2007). Subsequently, the exact dipole positions of the simulated sources were used to extract the reconstructed activity from the distributed solutions at the respective voxel position. However, it should be noted that both methods provide blurry solutions which diminishes the overall activity at each voxel. This affects the resulting time-course of active brain regions and therefore will also affect any connectivity estimation. It is pointed out in the present paper that this issue can be addressed by reducing the source space via ROIs or data-driven clustering as recently proposed by Wang et al. (Wang et al., 2018). Similar to the performance measures presented by Drakesmith (Drakesmith, 2012), connectivity spectra of multivariate Granger causality and time reversed Granger causality (Haufe et al., 2013, Winkler, Panknin, Bartz, Müller, and Haufe, 2016) were evaluated using false positive rate (FPR), false negative rate (FNR), and area under ROC curve (AUC).

While all of the above-mentioned studies imply innovative and advanced approaches, the studies by Drakesmith (Drakesmith, 2012), Haufe (Haufe et al., 2013), Farahibozorg (Farahibozorg et al., 2018) and Anzolin (Anzolin et al., 2019) exemplify the importance of a simulation design with high degree of realism to highlight the pitfalls and obstacles of connectivity analysis. Building on this, it is of great interest to analyse the influence of a number of other parameters on functional and effective connectivity analysis.

Further details on all papers introduced in this section can be found in table A1 with respect to the aspects of source localization, connectivity methods, statistical analysis and examined parameters.

1.3 Scientific Proposal

Despite the significance of connectivity methods, comprehensive studies comparing the performance of functional and effective brain connectivity indicators by means of simulated datasets are either lacking or not sufficiently comprehensive.

The main objective of this work is to fill in this gap by implementing and testing the performance of a subset of functional, as well as effective connectivity methods under comprehensive simulated but realistic sets of EEG data. In this context, several scenarios will be compiled to examine the effect of factors like SNR, data length, network size

or source reconstruction accuracy. Since connectivity and causality measures based on multi-channel electrophysiological data are biased by volume conduction artifacts, the realistic simulation not only covers the generation of lifelike recordings, but also implies inverse source localization to transform the EEG/MEG recordings into source space for subsequent connectivity estimation. For easier evaluation and comparison of connectivity methods, performance indicators will be introduced to enable a clear and informative presentation of analysis results. Furthermore, a statistical evaluation will help to understand the strengths and shortcomings of competing methods and will provide assistance in coming to more informed decisions about which connectivity estimator to employ for a specific task.

1.4 Outline of the Thesis

Following the introduction and problem formulation, chapter 2 provides an overview on electrophysiological signal generation and how these signals can be recorded with EEG and MEG. This chapter also presents mathematical concepts and approaches of inverse source reconstruction and concludes with an overview of functional and effective connectivity measures. Chapter 3 illustrates the structure and functionality of the simulation framework. It provides details on the software and open-source toolboxes used throughout the entire simulation and analysis process. Furthermore, the possibilities and modular options to generate electrophysiological signals with specific and desired characteristics are presented. In the following chapter (chapter 4) the impact of decisive factors on connectivity estimators is investigated using the presented simulation framework. These factors emerge and affect results during data acquisition, but also play an important role at further stages of connectivity analysis. Therefore, parameters influencing data simulation, like SNR and data length will be taken into account as well as other factors like network size, regularization and source analysis accuracy. In chapter 5 a connection is established between simulations and real-life conditions by transferring findings and conclusions derived from analysis of simulated data on real EEG recordings. Finally, the results of this thesis will be summarized and critically commented in chapter 6. Remaining analytical questions are discussed and potential for future research is suggested here.

Chapter 2

Fundamentals

In this chapter, essential principles to understand the formation and composition of neurophysiological data are presented. It covers the structure and functionality of the human brain and describes methods and procedures to measure brain activity. Furthermore, mathematical concepts to analyse cortical recordings are discussed. The strategies to estimate and reconstruct source activity from neurophysiological data sets are explained in more detail. On that basis, statistical or causal relationships among distinct brain regions can be calculated by applying different methods of connectivity estimators. The mathematical description of these methods, as well as their similarities and differences are covered in this section.

2.1 Neurophysiology

The electroencephalographic (EEG) or magnetoencephalographic (MEG) signal that is recorded from the outside of the head implies cortical activity caused by voltage fluctuations within the neurons of the brain, but also certain types of physiological and non-physiological artifacts. This section describes the origins of brain signals and their propagation to the surface of the scalp.

2.1.1 Neural Circuits and Systems

Neurons are the principal cellular elements that consist of a central cell body (soma), an axon that transfers information via synapses to other neurons, dendrites for receiving signals from other neurons and an enclosing membrane. Synapses can be excitatory or inhibitory and either increase or decrease activity in the receiving neuron, respectively. The dendrites receive information through synapses via neurotransmitters like glutamate, γ-aminobutyric acid (GABA) or dopamine. When receiving a stimulus, an electric potential is generated by depolarization of post-synaptic membranes. Figure 2 schematically shows

signal transmission between two neurons. The current arising from the activation of a single neuron cannot be detected through the scalp. However, synchronous activation of large populations of neurons have an additive effect due to their parallel organization. The strength of the current flow is directly proportional to the number of activated neurons and produces a detectable electroencephalographic signal.

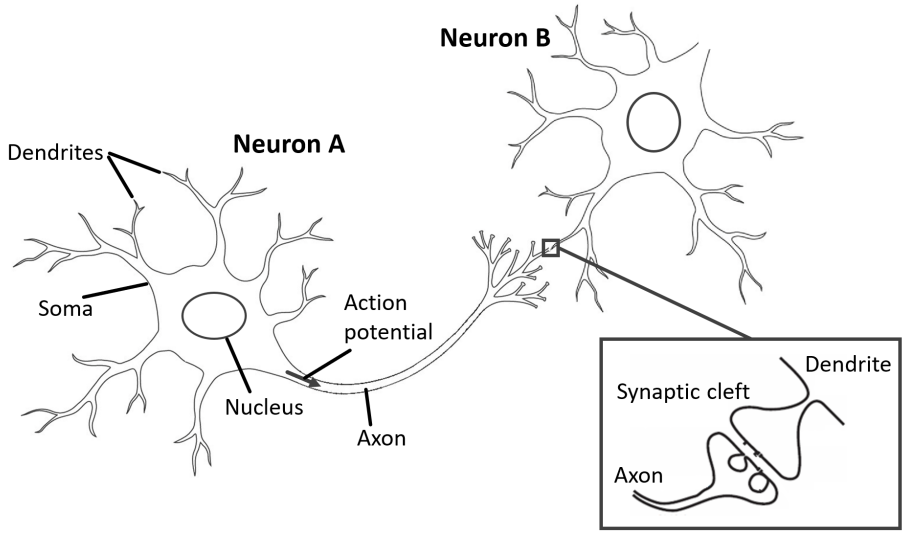

Figure 2: Neuron A transfers information to neuron B through the axon. The magnified part shows a synapse connecting both neurons.

The propagation of the current flow from populations of neurons through the brain, scull and scalp tissues and the cerebrospinal fluid (CSF) to the outside of the head is called volume conduction. The most significant factors influencing the spreading of currents from the sources are the geometries and conductivities of the traversed tissues. Mathematical models can be applied to estimate the propagation of a given cortical activity (see section 2.2.1).

2.1.2 Imaging Methods

EEG sensors placed along the scalp observe the electric potential to non-invasively record neural activity relative to a reference electrode. Basically, the distribution of electric potentials depends on the number of neurons that are activated simultaneously and the similarity of their spatial orientation, as opposed currents would otherwise cancel out each other (Shibasaki, 2008). Furthermore, activation in deeper cortical areas will result in a more widespread activation pattern on the scalp due to the aforementioned effect of volume conduction. Often 64 to 128 recording electrodes are used in research (Oostenveld and Praamstra, 2001), however, state-of-the-art EEG systems provide electrode caps with up to 256 channels (Suarez, Viegas, Adjouadi, and Barreto, 2000). With its high temporal resolution of about 1 millisecond, EEG is able to measure the fast dynamic changes of active cortical areas that change in the 10 to 100 millisecond range.

MEG records magnetic flux generated by electrical currents using either magnetometers or gradiometers (planar or radial) placed above the scalp surface (Cohen, 1968). The magnetic fields originate from the same underlying voltage fluctuations that evoke the EEG signal, however, they are less affected by volume conduction than EEG (Hämäläinen, Hari, Ilmoniemi, Knuutila, and Lounasmaa, 1993). This is mainly due to the fact that MEG is comparatively insensitive to secondary currents that propagate through the volume conductor to balance the primary current flow at the neuronal source. Modern MEG systems contain up to 300 sensors in a helmet shaped sensor array covering most of the head. Magnetic shielded rooms and active shielding systems are often used to reduce external noise and enable clear recordings of the magnetic signals emitted by the brain. Like EEG, MEG systems also record at a high temporal resolution and are therefore also well suited for analysing time-courses of neurophysiological activity.

Although signals of both neuroimaging techniques originate from the same cortical processes, MEG sensors are sensitive to magnetic fields perpendicular to the generating cortical patch, whereas EEG is more sensitive to electric currents flowing orthogonal to the EEG electrodes.

Besides EEG and MEG, there are other imaging methods that are sensitive to changes in cerebral blood flow related to neural activity. An increase in cortical activation will lead to a higher demand for glucose and oxygen in the particular area and therefore trigger an increased cerebral blood flow to the active region. Positron emission tomography (PET) detects radiation emitted by a radionuclide (tracer). The concentration of radionuclides indicates metabolic activity as it corresponds to glucose uptake and the activity at serotonin and dopamine receptors (Bunge and Kahn, 2009). Functional magnetic resonance imaging (fMRI) is another imaging method that has become more popular since it does not require the administration of tracers and provides a higher spatial resolution than PET. It measures the blood-oxygen-level dependent (BOLD) contrast that is refers to magnetisation changes of variations of blood oxygenation (Logothetis and Wandell, 2004).

The crucial distinction between PET and fMRI compared to EEG and MEG is the respective domain in which each technique has the highest resolution (Xue, Chen, Lu, and Dong, 2010). PET and fMRI benefit from a high spatial resolution, which is in the order of millimetres, at the cost of a very low temporal resolution, which is in the order of seconds. fMRI is an indirect, differential measurement since it measures the changes in blood oxygenation in veins and capillaries surrounding the active brain region, while electromagnetic recording methods acquire absolute neuronal activity. Moreover, EEG/MEG recordings provide a very high temporal resolution, as described in the previous section. Their spatial resolution, however, is in the order of several millimetres or even centimetres depending on the cortical regions that are to be localized. Furthermore, both imaging methods poorly measure activity arising below superficial neural structures, whereas fMRI records activity within

the entire brain volume. Nevertheless, EEG and MEG techniques are more suited for the analysis of rapid changing cortical networks due to their high temporal resolution. For this reason, electromagnetic recording methods are of key importance for this work to measure the performance of various connectivity estimators. However, reconstructing the temporal changes of brain activity from EEG and MEG recordings is essential to enable the calculation of correlation between active areas on the level of cortical regions. The next section of this chapter focusses on this problem and introduces a range of different methods and techniques.

2.2 Source Reconstruction

Non-invasive electromagnetic recording techniques are significant tools for imaging the temporal dynamics of neuronal currents. As discussed in the previous section, EEG systems measure the electrical potentials of the propagated neural current flows on the skin surface, whereas MEG measures the magnetic flux generated by these electrical currents in a distance of a few centimetres from the head. The estimation of the location of active cortical patches and their temporal evolution from the recorded current or magnetic field distribution is referred to as source reconstruction and is obtained by solving the so-called inverse problem (Mosher and Leahy, 1999, Baillet, Mosher, and Leahy, 2001; Nunez and Srinivasan, 2006).

2.2.1 Forward Modelling and Inverse Problem

Solving the inverse problem requires the simulation of the electric field potentials for a set of unit dipoles in a volume conductor model of the head. This approach is called forward modelling and estimates the contribution of each dipole using the quasi-static approximation of Maxwell's equations (Sarvas, 1987, Plonsey and Heppner, 1967, Baillet et al., 2001) for frequencies below 1000 Hz.
The forward solution to calculate the recorded electric scalp potential $V_S(r,t)$ for time t and sensor position r can be expressed as

$$V_S(r,t) = \iiint_{\Omega} L(r,r')G(r',t)^T \delta\Omega \tag{2.1}$$

where G is the cortical activity at position r' for a volume model Ω and L is the lead field matrix defining the contribution of a unit dipole at $G(r',t)$ to the scalp potential $V_S(r,t)$. L contains all geometric and conductive information about the different head volume conductor tissues (scalp, skull, CSF, gray matter and white matter) and needs to be modelled in great detail to allow accurate and realistic estimations of the measured electromagnetic signals.
Early numerical approaches to solve the forward problem for EEG included volume conductors using a single homogeneously conducting compartment (Frank, 1952) to model

the head. Later, models incorporating three (Geselowitz, 1967) and four (Hosek, Sances, Jodat, and Larson, 1978) concentric spheres, that model the skin, CSF, skull and brain layers were published. For MEG, a simpler model can be assumed since magnetic fields are less sensitive to secondary electric currents that propagate through the volume conductor to level primary electric currents generated by active cortical areas. Based on the assumption that the volume conductor model is spherically symmetric, an analytical solution for the forward problem can be derived (Sarvas, 1987).

State-of-the-art algorithms for the numerical calculation of realistic electromagnetic forwards models usually rely on the boundary element method (BEM; Fuchs, Wagner, and Kastner, 2001, Akalin-Acar and Gençer, 2004) and the finite element method (FEM; Yan, Nunez, and Hart, 1991, Wolters et al., 2006). Although both methods make use of subject-specific anatomical information obtained from magnetic resonance imaging (MRI) recordings, standardised age-appropriate BEM or FEM head models (Richards and Xie, 2015) can be applied as reasonable approximations for subjects where this information is not available.

For BEM, the volume between tissues are assumed to be homogeneous and isotropic conducting, which significantly reduces the computational effort of the forward model. However, the influence of conductivity inhomogeneities within compartments, e.g., in the skull compacta and spongiosa or white and gray matter compartment, on source reconstruction has been shown in several studies (Chauveau et al., 2004, Wolters et al., 2006, Güllmar, Haueisen, and Reichenbach, 2010). Incorporating anisotropic conductivities in BE models will lead to an increase in computational power and memory requirement. Most FE models also assume homogeneity and isotropy within tissues, but can extended more easily to model anisotropy from e.g. DTI recordings as well as more complex and accurate geometries.

Solving the inverse problem is inextricably linked to forward modelling and therefore affected by the degree of realism and accuracy of the head volume conductor model. Despite the challenges and difficulties arising from the process of source reconstruction, this step is mandatory for the estimation of connectivity on the source level. The next two sections present this topic in more detail and give an overview of discrete and distributed source reconstruction methods.

2.2.2 Discrete Source Reconstruction

The approach of discrete source reconstruction, also often referred to as dipole fitting, is primarily based on the fact that neural currents flow predominantly perpendicular to the surface of the cortex due to the perpendicular alignment of the pyramidal cells. A large number of adjoining, parallel currents are linearly summed up to one current vector representing the overall neural activity in the respective cortical area (figure 3).

This activation can be very accurately modelled by a single equivalent dipole (Scherg, 1990). It is defined by three parameters: its position, which is the according centre of the modelled cortical patch, its orientation, given by the direction of the neuronal current flow, perpendicular to the surface of the modelled cortical patch and magnitude. The magnitude of the dipole is expressed as a function of time and describes the neural dynamics of the modelled region. Due to the high temporal resolution of electromagnetic recording methods, the quickly changing connectivity patterns of neural networks can then be analysed using functional and effective connectivity methods.

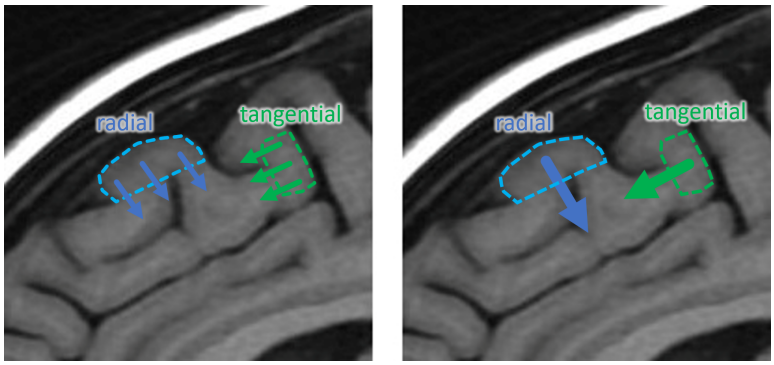

Figure 3: Example of activation at the cortical convexity (blue) having a predominantly radial orientation and activation in cortical fissures with a predominantly tangential orientation (green).

Discrete source localization approaches require a much smaller number of dipoles than distributed localization methods, as it is assumed that the largest part of the brain is not active (Scherg and Ebersole, 1993, Baillet et al., 2001).
The forward model for N dipoles can then be formulated as a linear sum from all contributing, active sources

$$V_S(r,t) = \sum_{n=1}^{N} L(r,n)S_n(t) \tag{2.2}$$

with $S_n(t)$ describing the source waveform of dipole n at time t. The resulting cost function is then defined as

$$min \left\| V_S(r,t) - \sum_{n=1}^{N} L(r,n)S_n(t) \right\|_2^2 \tag{2.3}$$

When performing inverse source reconstruction using dipoles, it is recommended to perform a sequential dipole fitting approach (Scherg, 1992, Scherg and Berg, 1996), which means that modelling each active cortical regions by a dipole will be performed sequentially. Thereby it is attempted to find points in time or time intervals in which only one brain area (or a pair of bilateral brain areas) is active. Assuming a given head model and a random

starting dipole location and orientation, the initial source waveform of the first dipole is estimated by applying the inverse of the leadfield matrix $L(r,n)$ to the data $V_S(r,t)$

$$S_{est,n}(t) = L^{-1}(r,n)V_S(r,t) \tag{2.4}$$

However, the matrix inversion $L^{-1}(r,n)$ is only defined if the number of columns (given by the number of sensors in the data matrix $V_S(r,t)$) and number of rows (number of modelled sources) of the leadfield matrix L would be identical and it would have a maximal rank. Thus, the pseudo-inverse L^+ of the leadfield matrix needs to be computed, which can be expressed as

$$L^+ = L^T(LL^T + \lambda I)^{-1} \tag{2.5}$$

using Tikhonov regularization (Tikhonov, Leonov, and Yagola, 1998) with the noise regularization parameter λ and the identity matrix I to resolve ambiguities and prevent over-fitting.

The estimated source waveform $S_{est,n}(t)$ is projected to the scalp surface using the forward model to calculate the modelled electrical distribution. In an iterative process, the dipole location and orientation is adjusted until the difference between the modelled data and measured data in the respective point in time or time interval is minimized by means of non-linear optimization. Genetic (Goldberg, 1989) or simplex algorithms (Press, Teukolsky, Vetterling, and Flannery, 2007) are applied to avoid solutions to converge on a local minimum, but to find the global minimum of equation 2.3. If the measured data requires fitting more dipoles to model activity in other cortical areas at later time points, the location and orientation of the fitted dipole will be fixed in the ongoing process.

When modelling brain areas that are in close proximity to each other, but differ by the direction of the neuronal current flow regional sources can be applied. For the EEG case, regional sources are dipoles with three orthogonal orientations. In contrast, regional sources for MEG consist of only two orientations due to the fact that MEG is mainly sensitive to tangentially oriented sources and is unable to detect radial sources (Hämäläinen et al., 1993, Baillet et al., 2001). A source localization strategy based on regional sources makes it possible to separate and model multiple source currents in any direction (Scherg and Berg, 1996).

2.2.3 Distributed Source Reconstruction

Like discrete source reconstruction approaches, distributed source imaging methods also use dipoles or regional sources as fundamental elements to model cortical activity. However, the number of sources differs greatly between those two approaches. As already mentioned

in the previous section, discrete source analysis only models larger cortical areas using a single dipole per patch to explain activity originating from the respective region. Contrary to this, in distributed imaging methods dipoles are placed at many locations within the brain to simultaneously estimate the activity at all those locations. This is further illustrated in figure 4.

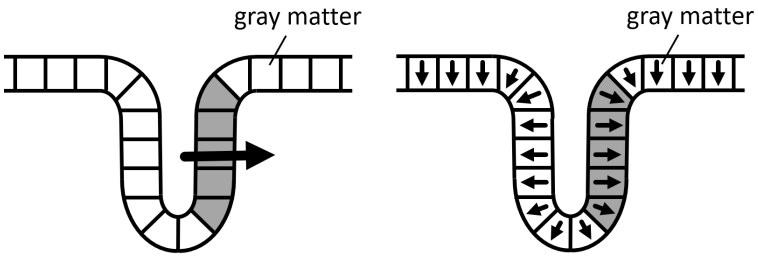

Figure 4: Modelling of cortical brain activity: on the left-hand side the cortical area in a fissure is modelled by a single dipole (discrete source), whereas on the right-hand side each small brain segment is represented by a current dipole (distributed source).

Frequently, the dipoles are also arranged in a 3-dimensional grid, where two or three dipoles with orthogonal orientations represent the activity in a voxel. This is an advantage compared to discrete imaging methods, since the number of active sources does not have to be estimated, but will be defined by the density of the grid. For this reason, distributed source models usually contain significantly more sources than recording sensors. Therefore, the system in equation 2.2 becomes highly under-determined and requires side constraints to be defined that allow the preferential selection of optimal solutions. The pseudo-inverse leadfield matrix is then defined by

$$L^{+} = (L^{T}L)^{-1}L^{T} \tag{2.6}$$

Distributed source reconstruction results obtained by applying minimum-norm estimate (MNE; Hämäläinen and Ilmoniemi, 1984) tend to be blurred as no spatial filtering is considered in this method. This is because solutions with the smallest overall energy, represented by the most superficial sources, are favoured. To overcome this bias, additional depth weighting may be implemented. This modified method is called weighted-minimum norm (WMN; Hämäläinen and Ilmoniemi, 1994) and normalizes all sources by a measure of their amplitudes to reduce localization errors.

Low resolution electromagnetic tomography (LORETA; Pascual-Marqui, Michel, and Lehmann, 1994) also implies depth weighting and provides images with high smoothness, due to the use of the 3D Laplace operator.

One major handicap that is common by almost all distributed source imaging methods is the fact that reconstructed 3D images are blurred and non-focal due to a smearing effect and crosstalk between neighbouring voxels. This is also the case for electromagnetic recordings

that represent focal brain activity. To resolve this problem, further imaging methods that determine a solution iteratively were proposed. These include, among others, standardized shrinking LORETA-FOCUSS (SSLOFO; Liu et al., 2005) and classical LORETA analysis recursively applied (CLARA; Iordanov, Hoechstetter, and Berg, 2014, Kovac et al., 2014). In both approaches, the spatial weighting matrix V reflects the solution found in the previous iteration step to eliminate activity in grid points that does not exceed a certain threshold. This process is repeated until a required accuracy or predefined number of iterations is reached.

In contrast to discrete source reconstruction, results obtained using distributed imaging methods generally cannot be used directly for subsequent connectivity analysis due to the large number of dipoles. Therefore, data dimensionality in source space needs to be reduced. This can be achieved by defining ROIs using a standard anatomical or histological brain atlas (Babiloni et al., 2005 and Astolfi et al., 2007) or a data-driven technique (Liu et al., 1998, Beckmann et al., 2005 and Hauk et al., 2011).

An alternative approach to solve the ill-posed inverse problem is to independently scan for sources within a regular three dimensional grid containing possible dipoles positions in every single grid point. Like in other inverse source reconstruction methods, a spatial filter is used. However, beamforming techniques use different spatial filter for each brain voxel to avoid crosstalk from other areas to affect the estimate of the region of interest as little as possible. Among the scan approaches, a popular solution can be obtained using linearly constrained minimum variance (LCMV) beamformers (Van Veen et al., 1997). The LCMV beamformer attempts to minimize the beamformer output power subject to a unity gain constraint:

$$\min_{W_r} \quad tr\left(W_r^T C W_r\right) \tag{2.7}$$

provided $W_r^T L_r = I_3$. W_r denotes the d_m by 3 spatial filtering matrix, C is the data covariance matrix and L_r is the d_m by 3 leadfield matrix of the model at target location r. The spatial filter satisfying this equation can be calculated by:

$$W_r^T = \left(L_r^T C^{-1} L_r\right)^{-1} L_r^T C^{-1} \tag{2.8}$$

The beamformer output provides an estimate for the source power X at location r by:

$$X_r = G_r W_r \tag{2.9}$$

To compute a distributed map of activity, this solution can be applied at each source point of interest.

2.3 Brain Connectivity Measures

Results obtained from discrete or distributed source analysis methods provide insights on the spatio-temporal dynamics of cortical areas. They enable modelling and estimating the number of active brain regions, as well as their location and temporal changes in magnitude. Building upon this knowledge, various functional and effective brain connectivity estimators have been proposed to reconstruct and quantify neuronal interactions.
This section presents an overview on commonly used connectivity methods and describes the main characteristics and features for each of the estimators. The various methods are grouped into non-directed (functional) connectivity metrics, that provide information on the statistical dependence between signals without implying information on the directionality, and, on the other hand, directed (effective) connectivity measures which indicate causal dependencies among sources.

2.3.1 Autoregressive Modelling

Most methods of effective connectivity are based on the definition that causes must precede their effects. Wiener (Wiener, 1956) defined the notion of causality as the prediction of a time-series from another time-series, stressing temporal ordering. He first addressed the approach to reproduce statistical causal relationships from data, which was later adopted and applied by Granger (Granger, 1969) to linear bivariate regression modelling in order to analyse time-series that originated in economics. He also introduced the term of Granger causality. It was later extended by Geweke (Geweke, 1982) to examine time-series in the spectral domain. Many effective connectivity methods that have been developed in recent years are based on interpretations or modifications of this concept.
Due to its limitation to two time-series, the bivariate approach is not applicable to more complex systems. Simultaneous analysis of multichannel networks is particularly essential in neuroscience where, in the majority of cases, several active brain regions are interacting via numerous connections. A multidimensional approach reduces the possibility of erroneous causality estimations in comparison to a pair-wise analysis, as causality between two channels can only be calculated correctly if they are not influenced by a third channel (Granger, 1980).
Moreover, data stationarity is preconditioned to employ autoregression (AR) models. Electrophysiological signals including EEG and local field potentials (LFPs) are however highly non-stationary processes. In order to overcome these problems, and to apply AR models to non-stationary multidimensional datasets, a variety of algorithms have been established that assemble multivariate regression modelling with overlapping sliding-window approaches (Ding, Bressler, Yang, and Liang, 2000) and time-variant

Granger causality (Hesse, Möller, Arnold, and Schack, 2003) have been established. Multivariate regression modelling offers the possibility to examine the links between all sources simultaneously. Further, other extensions and modifications of Granger causality were suggested, that involve non-linear Granger causality (Marinazzo, Pellicoro, and Stramaglia, 2006).

According to Granger (Granger, 1969), a time-series x_i Granger-causes time-series x_j if incorporating past values of x_i in the prediction of x_j leads to a better prediction above and beyond consideration of only past values of signal x_j alone (Granger, 1969, Ding, Chen, and Bressler, 2006). This causal influence between time-series $x(t)$ an be measured using multivariate-autoregressive (MVAR) models. For illustration, a bivariate AR model with variables x_i and x_j and N past time points is represented as

$$\begin{aligned} x_i(t) &= \sum_{n=1}^{N} a_{1,n} x_i(t-n) + \sum_{n=1}^{N} a_{2,n} x_j(t-n) + \varepsilon_i(t) \\ x_j(t) &= \sum_{n=1}^{N} a_{3,n} x_i(t-n) + \sum_{n=1}^{N} a_{4,n} x_j(t-n) + \varepsilon_j(t) \end{aligned} \tag{2.10}$$

with uncorrelated noise terms $\varepsilon_i(t)$ and $\varepsilon_j(t)$ and AR model coefficients $a_{k,n}$ describing the contribution of $x_i(t)$ and $x_j(t)$ at past time points.

The correct order N of an AR model can be determined by minimizing the Akaike Information Criterion (AIC; Akaike, 1974) or applying other commonly used criteria like the Bayesian Information Criterion (BIC; Schwarz, 1978) or Akaike Final Prediction Error Criterion (FPE; Niedzwiecki and Ciolek, 2017). Depending on the distribution of the noise terms, approaches like ordinary least squares regression or Yule-Walker equations may be implemented to estimate the coefficients of AR models (Schlögl, 2006).

The concept of Granger causality can also be applied in the frequency domain (Geweke, 1982) by Fourier transforming equation 2.10

$$\begin{pmatrix} a_1(f) & a_2(f) \\ a_3(f) & a_4(f) \end{pmatrix} \begin{pmatrix} x_i(f) \\ x_j(f) \end{pmatrix} = \begin{pmatrix} E_i(f) \\ E_j(f) \end{pmatrix} \tag{2.11}$$

where the components of the coefficient matrix $A(f)$ are defined as

$$\begin{aligned} a_1(f) &= 1 - \sum_{j=1}^{\infty} a_{1j} e^{-ifj} & a_2(f) &= -\sum_{j=1}^{\infty} a_{2j} e^{-ifj} \\ a_3(f) &= -\sum_{j=1}^{\infty} a_{3j} e^{-ifj} & a_4(f) &= 1 - \sum_{j=1}^{\infty} a_{4j} e^{-ifj} \end{aligned} \tag{2.12}$$

To obtain the so called spectral transfer matrix or transfer function $H(f)$, equation 2.11 can be rearranged as

$$\begin{pmatrix} x_i(f) \\ x_j(f) \end{pmatrix} = \begin{pmatrix} H_{ii}(f) & H_{ij}(f) \\ H_{ji}(f) & H_{jj}(f) \end{pmatrix} \begin{pmatrix} E_i(f) \\ E_j(f) \end{pmatrix} \tag{2.13}$$

The transfer function is the inverse of the coefficient matrix $H(f) = A^{-1}(f)$ with the components

$$\begin{aligned} H_{ii}(f) &= \frac{1}{det(A)} a_4(f) \qquad H_{ij}(f) = -\frac{1}{det(A)} a_2(f) \\ H_{ji}(f) &= -\frac{1}{det(A)} a_3(f) \quad H_{jj}(f) = \frac{1}{det(A)} a_1(f) \end{aligned} \tag{2.14}$$

and the elements $H_{ij}(f)$ of the transfer matrix describing the information transfer of the network from channel i to channel j.

Granger causality in the frequency domain as introduced in the preceding section is based on parametric methods (AR models). An alternative approach is the derivation with non-parametric methods using Fourier transformation or wavelet based methods. Non-parametric estimation of the transfer matrix builds upon the factorization of the cross-spectral density (CSD) matrix (Wilson, 1972) into a noise covariance matrix Σ and transfer function $H(f)$

$$S(f) = H(f)\Sigma H^*(f) \tag{2.15}$$

where $*$ denotes matrix adjoint. A comparison between parametric and non-parametric estimation of Granger causality for simulated data with comparable results was done by Dhamala et al. (Dhamala, Rangarajan, and Ding, 2008). However, non-parametric methods have the distinct advantage that they do not depend on the estimation of the AR model order. The choice of an eligible model order can be challenging as it is strongly data dependent (Kamiński and Liang, 2005). On the downside, the factorization of the transfer function with non-parametric methods requires smooth gradients of the CSD matrix to assure stability and convergence.

2.3.2 Measures of Functional Connectivity

A fundamental and widely used method to detect synchronized activation of cortical areas is coherency. It is defined as the normalized cross-spectrum of two zero-mean time series $x_i(t), x_j(t)$ and their Fourier transforms $x_i(f), x_j(f)$ of channels i and j, respectively (Nunez et al., 1997).

With the cross-spectrum defined as

$$S_{ij}(f) = \left\langle x_i(f) x_j^*(f) \right\rangle \tag{2.16}$$

where $\langle\rangle$ means expected value, coherency is complex valued $Chy_{i,j}(f) \in \mathbb{C}$ and is written

as

$$Chy_{i,j}(f) = \frac{S_{ij}(f)}{\sqrt{S_{ii}(f)S_{jj}(f)}} \tag{2.17}$$

Lachaux et al. (Lachaux, Rodriguez, Martinerie, and Varela, 1999) pointed out that coherency can only be applied to stationary signals since it is usually computed over multiple trials with the same spectral properties. However, it is rather the interpretation of coherency results that must consider a stationary as well as a non-stationary process (Nolte et al., 2004). Furthermore, coherency is a measure that is sensitive to phase and amplitude correlation. Although the two parameters are mathematically independent from each other, the phase structure of weak signals can be distorted by noise leading to erroneous connectivity estimations (Nolte et al., 2004).
Coherence, also known as magnitude-squared coherency, is defined as the absolute value of coherency

$$Coh_{ij}(f) = \left|Chy_{ij}(f)\right|^2 = \frac{\left|S_{ij}(f)\right|^2}{S_{ii}(f)S_{jj}(f)} \tag{2.18}$$

The normalization of coherence compensates for large values in the cross-spectral density matrix that result from large amplitudes. Coherence has a value range bounded by 0 to 1, with lower values indicating less correlation and is used to identify the connection strength between two signals, but does not discriminate between instantaneous (zero time lag) correlation and actual time-delayed correlation (Nunez et al., 1997, Haufe et al., 2013). Another disadvantage of coherence, just as coherency, is its inability to differentiate between direct and indirect connections. Direct connections describe the information flow from source 1 to source 2 without an interposed third source, whereas indirect connections indicate information flow via a third source 3 (figure 5). In order to distinguish, whether channels are associated by a direct or indirect connection, different techniques are required.

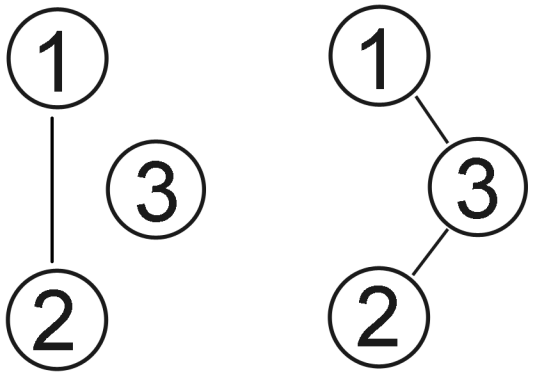

Figure 5: Direct (left side) and indirect (right side) information flow between two source 1 and 2.

One of the methods that is able to differentiate between direct and indirect links, is partial coherence. It was introduced by Franaszczuk (Franaszczuk, Blinowska, and Kowalczyk, 1985) and is defined as

$$PCoh_{ij}(f) = \frac{M_{ij}(f)}{\sqrt{M_{ii}(f)M_{jj}(f)}} \tag{2.19}$$

where $M_{ij}(f)$ denotes the minor of the cross-spectral density matrix $S_{ij}(f)$. $M_{ij}(f)$ is obtained by calculating the determinant of a sub-matrix formed by deleting the i-th row and j-th column of $S_{ij}(f)$.
The above-mentioned functional connectivity methods refer to the cross-spectral density $S_{ij}(f)$

$$S_{ij}(f) = r_i r_j e^{i(\phi_i - \phi_j)} = r_i r_j e^{i\Delta\phi_{ij}} \tag{2.20}$$

with $\Delta\phi_{ij}$ being the phase difference between the signals $x_i(f)$ and $x_j(f)$ at a specific frequency f. As the CSD matrix is weighted with the product of the signals amplitudes r_i and r_j, the connectivity estimations based on the CSD matrix are also amplitude-weighted. However, it can be helpful to separate the phase component from the amplitude component in order to investigate how each part effects the relationship between two signals independently. The phase-locking value (PLV), introduced by Lachaux (Lachaux et al., 1999) is based on this approach. It is defined as the sum of phase differences between two signals at time t, averaged over N trials

$$PLV_{ij}(f) = \frac{1}{N}\left|\sum_{n=1}^{N} e^{i(\varphi_{i,n} - \varphi_{j,n})}\right| \tag{2.21}$$

with $\varphi_{i,n}$ defining the phase angle of signal i and n indexing the N trials. PLV measures the variability of the phase difference between two signals within trials. If the phase difference is stable across the trials, PLV is close to 1, on the other hand, if the signals are independent, the phase angle will have a uniform distribution and lead to a PLV of 0. As stated earlier in this section, the phase of a signal is mathematically independent from its amplitude. However, applying simulated and real data examples, it can be demonstrated that noise can destroy the phase information of weak signals (Nolte et al., 2004). Therefore, it is possible that coherence might give better results for the estimation of the phase synchrony between two signals than the phase-locking value.

2.3.3 Measures of Effective Connectivity

The connectivity methods introduced in the preceding section examine the similarity of two time-series in a statistical manner and serve as estimators for functional connectivity. However, they do not disclose the directionality of information flow and cannot estimate

causal relationships.

Nolte (Nolte et al., 2004) proposed an effective connectivity method to reconstruct causal relations that is derived from coherency. He suggested to neglect the "volume-conducted" real part of coherency and only to look at the imaginary part, because this component necessarily reflects time lagged interaction between sources and ignores instantaneous correlation. Furthermore, he states that the imaginary part is insensitive to artifacts of volume conduction, as volume conduction cannot create an imaginary part. The method denominated as imaginary part of coherency is expressed as

$$iChy_{ij}(f) = imag\left(Chy_{ij}(f)\right) \tag{2.22}$$

Values of imaginary part of coherency range between -1 and 1, with positive values indicating that x_i occurs earlier than x_j and therefore information seems to flow from source x_i to x_j. However, the estimation of the directionality for a specific frequency may be ambiguous in its interpretation, since, for example, a 10 ms advance cannot be distinguished from a 90 ms delay for a 10 Hz frequency. To overcome this problem, Nolte proposed another estimator that sums up the information within a frequency band of interest to robustly determine the direction of causal relationships between time-courses (Nolte et al., 2008). This estimator is called phase slope index (PSI) and is written as

$$\Psi_{ij} = imag\left(\sum_{f\in F} Chy^{*}_{ij}(f)Chy_{ij}(f+\delta f)\right) \tag{2.23}$$

where F denotes the set of frequencies, with frequency resolution δf, over which the slope is summed. Due to the fact that the PSI is based on the imaginary part of coherency, it is insensitive to mixtures of non-interacting sources (Nolte et al., 2004, Nolte et al., 2008). Furthermore, Nolte compares PSI to Granger causality and points out that PSI is superior in cases where unidirectional flow and undirected noise are simulated, since Granger causality fails to differentiate between the two effects.

The following effective connectivity methods are based on the transfer matrix $H(f)$ and the noise covariance matrix Σ. Depending on how these matrices are calculated, the respective methods are seen as model-based (if the matrices are calculated using AR models) or non-parametric (if Fourier or wavelet based techniques are applied to estimate the matrices). The frequency-dependent Granger causality (GC; Geweke, 1982, Dhamala et al., 2008) is expressed as

$$GC_{ij}(f) = ln\left(\frac{S_{jj}(f)}{S_{jj}(f) - (\Sigma_{ii} - \frac{\Sigma^2_{ji}}{\Sigma_{jj}})\left|H_{ji}(f)\right|^2}\right) \tag{2.24}$$

A time-series $x_i(f)$ is defined to Granger-cause time-series $x_j(f)$ for a specific frequency f,

if $GC_{ij}(f)$ is significantly greater than 0.
Another methods that was proposed by Kaminski and Blinowska (Kamiński and Blinowska, 1991) is directed transfer function (DTF)

$$DTF_{ij}(f) = \gamma_{ij}^2(f) = \frac{|H_{ij}(f)|}{\sum_{k=1}^{N} |H_{ik}(f)|} \tag{2.25}$$

DTF is, in contrast to Granger causality, a normalized connectivity estimator ranging from 0 to 1. It can be interpreted as the ratio of the information flow from channel j to i, divided by the total inflow to channel i. A downside of DTF is its inability in the distinction of direct and indirect connections between signals. In order to compensate for this weakness of DTF, Korzeniewska (Korzeniewska et al., 2003) defined two new measures. The full frequency directed transfer function (ffDTF) represents a different normalization of DTF and is expressed as

$$ffDTF_{ij}(f) = \eta_{ij}^2(f) = \frac{|H_{ij}(f)|^2}{\sum_f \sum_{k=1}^{N} |H_{ik}(f)|^2} \tag{2.26}$$

By summation over the whole frequency range, the dependence of the denominator on frequency is eliminated. However, just as DTF, ffDTF is still not able to detect differences between direct and indirect connections. Therefore, Korzeniewska introduced the direct directed transfer function (dDTF; Korzeniewska et al., 2003), which connects information from partial coherence and the ffDTF

$$dDTF_{ij}(f) = PCoh_{ij}(f) \times ffDTF_{ij}(f) \tag{2.27}$$

Due to the combination of PCoh, which is able to distinguish between direct and indirect connections and ffDTF, the strength of only direct connections between two channels will be exposed. However, partial coherence is prone to an effect called marrying parents of a joint child (Winterhalder et al., 2005). This refers to the analysis of two (parents) time-series with a causal relationship to a third (child) time-series. In this case partial coherence, and therefore dTDF as well, will detect a non-existing causal link between the parents time-series. dDTF values are in the interval [0; 1], where higher values indicate higher interaction between the channels.
Partial directed coherence (PDC; Baccalá and Sameshima, 2001) has been introduced to reconstruct causal relationships in multivariate systems. It is based on Granger causality and uses the Fourier transformed coefficient matrices of equation 2.12

$$PDC_{ij}(f) = \pi_{ij}(f) = \frac{a_{ij}(f)}{\sqrt{\sum_{k=1}^{N} a_{ki}(f)a_{kj}(f)}} \tag{2.28}$$

The normalization in the equations of the DTF and the PDC is a significant difference between both analysis techniques. PDC quantifies the connectivity between time-series j and i with respect to all connections of j to other components of the analysed network, satisfying the equation

$$\sum_{i=1}^{N} \left|\pi_{ij}(f)\right|^2 = 1 \tag{2.29}$$

Moreover, PDC, compared to DTF, has the great benefit that the inversion of the coefficient matrix A is not necessary for its calculation. This not only leads to a computational advantage, but also the fact that PDC is able to distinguish between direct and indirect connections (Astolfi et al., 2006). Both estimators, and their derivatives, along with the incentive to choose one metric over the other, are examined in more detail in Blinowska et al. (Blinowska, 2011).

More recently, Astolfi (Astolfi et al., 2006) proposed a new variation of PDC called the squared partial directed coherence (sPDC)

$$sPDC_{ij}(f) = \frac{|a_{ij}(f)|^2}{\sum_{k=1}^{N} |a_{kj}(f)|^2} \tag{2.30}$$

The modification of squaring the AR coefficients leads to an increase in the sensitivity of the PDC (Astolfi et al., 2006).

Chapter 3

Simulation Model

As described in the previous chapter, different functional and effective connectivity estimators are based on different underlying mathematical concepts or address various aspects of connectivity. This complicates not only the choice of the connectivity method that is best suited for a particular type of data analysis, but also makes it difficult to evaluate the quality of different connectivity results, as a ground truth solution is generally unavailable for real electromagnetic recordings. For these reasons, it is essential to analyse simulated data with a predefined ground truth and known properties to be able to identify and compare strengths and weaknesses of particular methods.
The goal of this work is to compare the performance of various connectivity estimators based on a simulation framework that meets the following criteria:

- High degree of realism: simulated neurophysiological data generated by a known architecture provides the possibility to assess the effect of various parameters. However, in order to enable the transfer of knowledge gained by simulation studies to real world applications, simulative techniques must not be over-simplified.

- Standardisation: various simulation studies investigating the performance of connectivity estimators have been proposed in the last decades, with some of them implying highly differentiated approaches. The degree of technical complexity and innovation varies considerably between the studies, leading to an essential aggravation or even impossibility to compare results and findings. For this reason, this work makes use of well established standards.

- Statistical evaluation: in order to point out significant differences between results and thus measure the quantitative effect of certain parameters on connectivity estimators it is essential to carry out statistical tests.

- Expandability: the modular structure of the simulation architecture easily enables enhancing or exchanging parts of the simulation to use (e.g.) more complex modelling

techniques and implement other inverse source reconstruction methods or connectivity estimators.

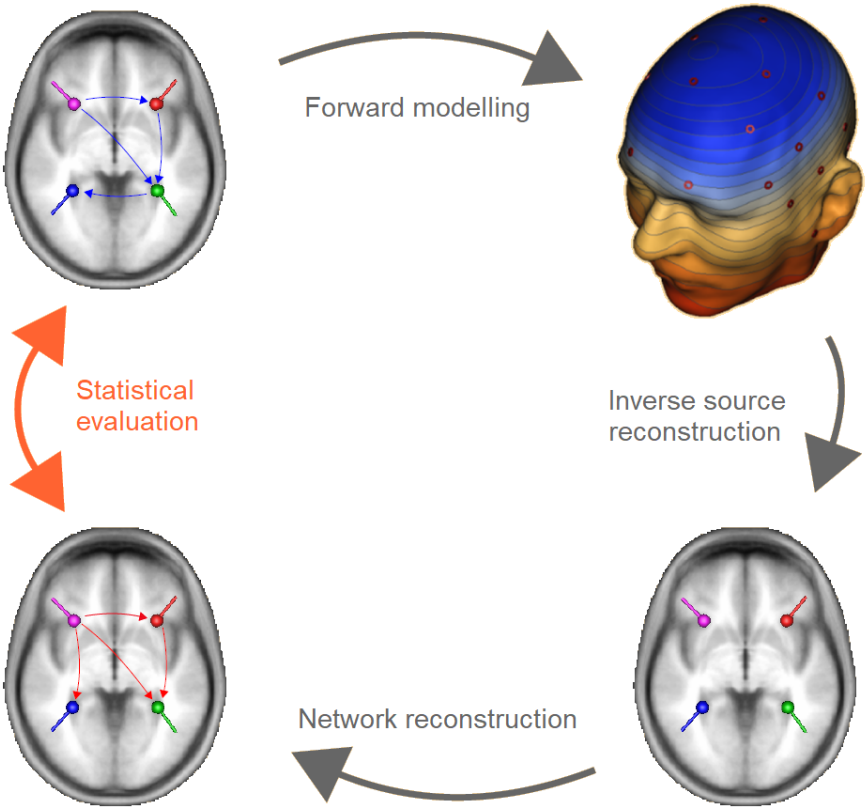

Figure 6: Schematic layout of the simulation pipeline, that is divided into four modules, covering the domains of signal generation, inverse source reconstruction, connectivity analysis and statistical evaluation. In the first step (top-left), all characteristics of the simulated network (blue network links) and the properties of the data set need to be defined, prior to the computation of the simulated recording via forward modelling (top-right). Subsequently, inverse source analysis methods are applied to estimate the temporal activity of active brain regions (bottom-right). The resulting source-waveforms are then used to reconstruct the network (bottom-left; red network links). Finally, the simulated and the reconstructed network are statistically compared to obtain a measure for the accuracy and reliability of each connectivity method.

The working principle and the entire composition of the simulation is shown in figure 6. Prior to the start of the simulation pipeline, various parameters must be defined to determine the characteristics of the network and the properties of the electromagnetic data, as well as modelling and analysis techniques. On that basis, the simulation starts with the generation of the underlying cortical network and calculates the expected EEG or MEG data. The additional step of forward modelling with subsequent inverse source reconstruction

allows incorporating and considering parameters and effects that might affect the outcome of connectivity analysis. The estimated waveforms of active cortical sources are used to reconstruct the cortical network by applying multiple functional and effective connectivity methods. As the last step, a statistical evaluation needs to be performed to check for stability and convergence of the solutions and to test for significant differences when comparing the reconstructed network against the ground truth.
This section introduces a comprehensive simulation architecture that was designed and implemented to evaluate and assess connectivity methods. The framework is divided into four modules that cover the domains of signal generation, inverse source reconstruction, connectivity analysis and statistical evaluation. The extent and complexity of the individual simulation stages are described in detail in the following sections.

3.1 Signal Generation

The initial part of the simulation pipeline covers the spatio-temporal characterization of the cortical network to be modelled, the addition of neural and sensor noise, as well as the forward modelling, to obtain simulated electromagnetic data. This component was completely developed using MATLAB 7.4.0.287 (The MathWorks, Inc., Natick, Massachusetts, United States) and the MATLAB-based open-source toolbox Fieldtrip (Oostenveld, Fries, Maris, and Schoffelen, 2011).

3.1.1 Definition of Cortical Networks and Neural Noise

The simulation architecture provides two types of models to generate activity for a predefined number of distinct cortical sources: a multivariate-autoregressive (MVAR) approach and a model that uses band-pass filtered Gaussian noise time-courses as the basis for cortical activity.
MVAR models, as introduced in equation 2.11 for the bivariate case, offer the advantage of defining the time-delayed linear influences from one source to another directly by setting the respective off-diagonal entries of the coefficient matrix $A(f)$ to non-zero values. For the simplified example of only two sources (equation 2.11), a unidirectional influence of time-series $x_i(t)$ on $x_j(t)$ can be achieved by setting the coefficients $a_2(f,n)$, with $n \in \{1,...,P\}$, to zero for all time-lags n, while $a_3(f,n)$, with $n \in \{1,...,P\}$ are generally non-zero values. This principle can easily be extended to networks consisting of a larger number of active cortical areas and the required number of time-lags. Because of this high flexibility and individual adaptability, MVAR models are widely used in the generation of simulated electromagnetic recordings (Astolfi et al., 2007, Florin et al., 2010, Wu et al., 2011, Silfverhuth et al., 2012).

The second option to generate coherent source waveforms is to use a joint signal for interrelated sources. In this work, a Gaussian white noise signal serves as such a common input signal, as illustrated in figure 7.

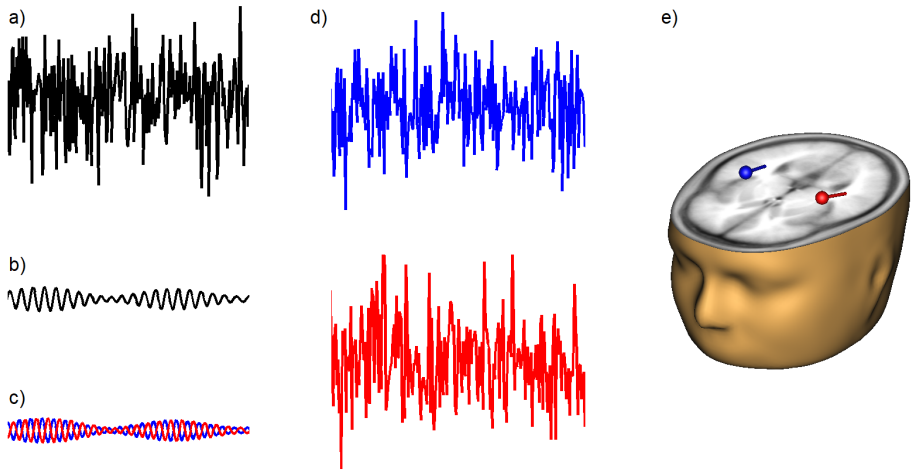

Figure 7: Simulation of coherent activity for two sources located in the left and right auditory cortex using a band-pass filtered Gaussian noise signal. A band-pass filter (with a width from 24 Hz to 28 Hz) is applied on a Gaussian white noise signal (a) to obtain a source waveform centred around the frequency of interest (b). A causal dependency between signals (c) is created by introducing a phase shift. Individual white noise is added to each individual waveform (d). Positions of active cortical regions are determined by placing dipoles in the respective brain areas (e).

By applying a band-pass filter on the base signal with a width covering the frequency range of interest (figure 7 shows a band-pass filtered signal with a frequency range of interest from 24 Hz to 28 Hz), only spectral components remain that are of particular focus for subsequent connectivity analysis. Furthermore, the band-pass filtered signal may be shifted by a specific phase to simulate uni-directional information flow from one source to another. In the final step of generation of correlated source waveforms, white noise is then added to the individual waveforms.

Both approaches take neither the absolute position of the respective source in the human brain nor the relative position of sources to each other into account and are therefore completely independent from the position and orientation of the modelled cortical areas. This allows, on the one hand, an unrestricted choice for the simulation of activated brain regions and enables the simple adaptation of modelled activity for different simulations and iterations. On the other hand, studies (Vander, Sherman, and Luciano, 2001, Wen and Chklovskii, 2005) showed that the relative position of sources to each other and thus, the distance or wiring length does affect the communication between distinct areas. In particular, the time lag of information flow between regions is influenced by this parameter. In the present simulation study, this effect on cortical networks is not considered.

Besides the active regions of the correlated cortical network, further noise sources,

distributed in the entire brain space, are used to simulate non-correlated background activity. Locations and orientations of up to 29 regional sources are randomly chosen, as shown in figure 8. The list of labels and positions for each source is given in table A7.

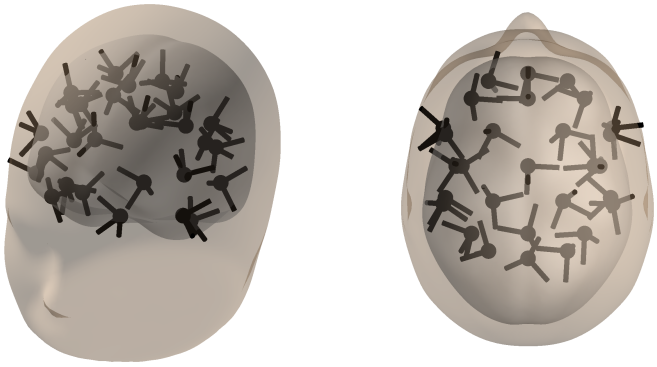

Figure 8: Position of noise sources (29 regional sources) used to simulate independent background noise. Regional source were placed randomly with a minimum distance between sources of at least 20 mm and orthogonal orientations. For the simulation of EEG recordings, regional sources consisted of dipoles with three orthogonal orientations. In this image, the surfaces of scalp and brain layers are shown in transparent colour.

Waveforms of these noise sources are defined using three types of noise: Gaussian white noise, pink noise (noise with a frequency spectrum where the power spectral density is inversely proportional to the frequency) and real EEG noise. Realistic noise waveforms were retrieved from an auditory EEG experiment.

3.1.2 Simulation of EEG and MEG Recordings

Forward modelling requires information about the specific head model used in the simulation process, as well as the EEG or MEG sensor configuration and the position and orientation of active brain regions to simulate electromagnetic recordings.
Due to the modular design of the simulation architecture, different types of head models are provided for forward modelling and further models can be integrated without difficulty. The head models implemented include: single-shell sphere (MEG only, Sarvas, 1987), spherical 3-shell model (Geselowitz, 1967), age-appropriate template models (Richards and Xie, 2015) and individual finite-element models (Yan et al., 1991, Wolters et al., 2006). The impact of head model selection and accuracy of tissue compartment geometry on EEG forward modelling has been considered in several studies (Hallez et al., 2007).
In each simulation run, active cortical regions are represented by dipoles. The centre locations of distinct brain regions are required to be at least 40 mm away from each other to reduce errors in the correct separation of cortical activity during inverse source reconstruction. Moreover, dipole locations are restricted to have a maximum source depth, which is the Euclidian distance between the dipole centre and the cortex surface, of 40 mm.

For all simulation scenarios, the number of modelled cortical regions, excluding additional noise sources, ranged between 4 and 10 areas.
EEG and MEG scalp topographies are then computed by summing up the contributions from all sources using equation 2.2, with electrode positions defined in the 10-5 electrode placement system (Oostenveld and Praamstra, 2001).
After the scalp topographies for the modelled brain activity of interest and the background noise have been estimated, the noise signals need to be scaled to the desired signal-to-noise ratio before combining both topographies to obtain a simulated electromagnetic recording. SNR is defined as the ratio of signal power P_S to the noise power P_N. The SNR for a single sensor is then computed as

$$SNR = \frac{P_S}{P_N} \tag{3.1}$$

For multi-trial evoked response recordings, SNR is typically calculated in the time-domain, resulting in an estimation of signal quality for the entire frequency spectrum. However, due to the decrease in power with increasing frequency in the spectrum of measured electromagnetic brain signals, this approach may not reflect the precise proportion of signal and noise for the selected frequency range of interest. For this reason, the SNR is calculated in the frequency-domain using the power spectral density of the brain $PSD_S(f)$ and noise topographies $PSD_N(f)$

$$SNR(f) = \frac{PSD_S(f)}{PSD_N(f)} \tag{3.2}$$

Depending on the frequency range of interest, the respective spectral components of the noise signal are scaled to obtain the required SNR (figure 9). Simulations considering a broad yet realistic range of SNR ranging from 0.1 up to 15 are carried out to reveal the influence of SNR on connectivity estimators (see chapter 4.2).
To provide an undistorted view on the effect of SNR, it should be noted that it is vital to avoid large differences in the signal-to-noise ratios between single sensors as this may lead to asymmetries in connectivity estimators like Granger causality. This distortion of causal dependencies driven by SNR differences has been defined by Haufe et al. as “weak asymmetries” (Haufe, Nikulin, and Nolte, 2012).

3.2 Inverse Source Reconstruction

Inverse source reconstruction is vital for connectivity analysis, as the interpretation of connectivity measures from EEG or MEG sensor level data is non-trivial and results do not necessarily reflect insights in the information flow between interacting cortical regions. This is mainly due to the effect of volume conduction, which precludes a direct connection

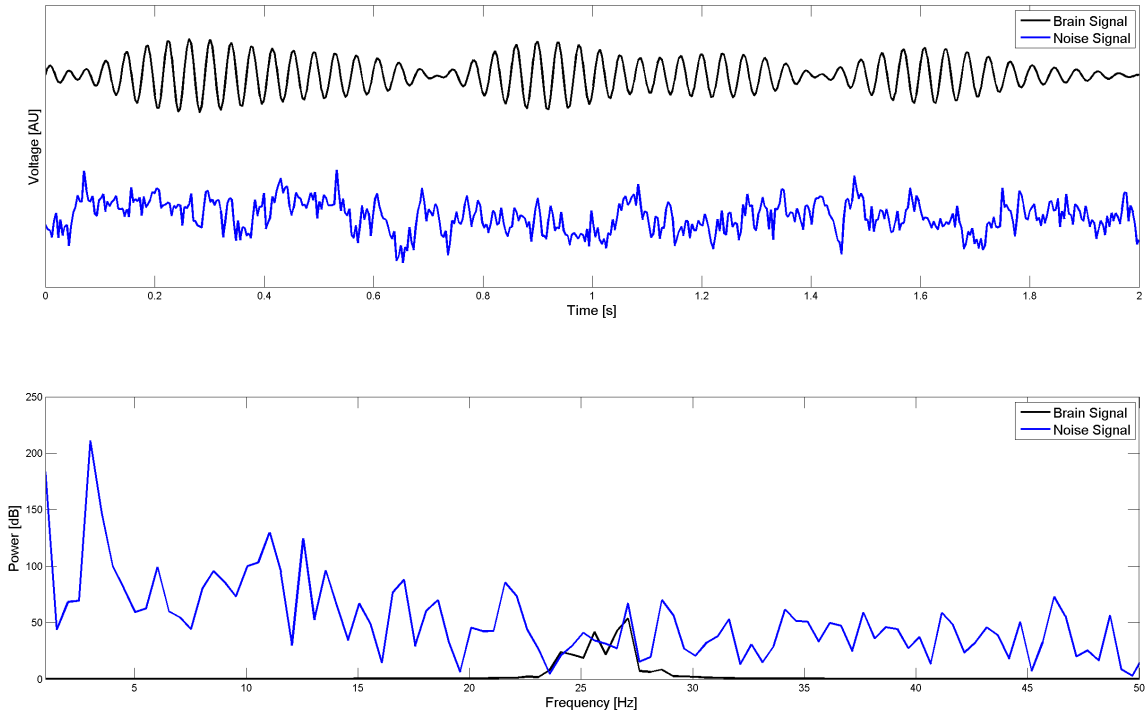

Figure 9: Waveforms (top) and power spectral density (bottom) of brain and noise signal. Power spectra of brain signal show a distinct peak for the frequency range of interest (24 Hz to 28 Hz).

and relationship between the sensor time-series and the source waveforms of activated brain areas (Nunez and Srinivasan, 2006; Haufe et al., 2013). Depth and orientation of sources have a great influence on how a source is projected to the sensors. Furthermore, the application of connectivity estimators on sensor data can lead to the detection of spurious connections (Schoffelen and Gross, 2009, Vinck et al., 2015; Bastos and Schoffelen, 2016). To resolve these difficulties, inverse source reconstruction methods will be implemented to reconstruct the temporal dynamics of cortical areas from EEG and MEG sensor data. However, this approach does not guarantee an error-free identification of the network in the source space, as the inverse solution is strongly influenced by the selected reconstruction method and the volume conductor model. Besides, volume conduction effects can also never be entirely resolved in source space and may lead to spurious connections between sources (Palva and Palva, 2012). This issue is particularly relevant in the evaluation of real neurophysiological data. Therefore, it is of great importance to analyse how certain parameters of inverse source reconstruction affect the results of connectivity estimators.
The simulation framework makes use of brain source montages (Scherg, Ille, Bornfleth, and Berg, 2002; Scherg et al., 2004) to transform simulated EEG and MEG recordings back into the source space. Source montages estimate the time-course of active brain regions modelled by either dipoles or regional sources. Therefore, a spatial filter is applied to separate the source activities that overlap at the scalp surface, given that the modelled current dipoles

(and regional sources) account for all active cortical areas (figure 10). Spatial filters of a source montage modelling multiple active brain regions are computed by generating a linear inverse operator of the leadfield matrix L (Mosher, Lewis, and Leahy, 1992; Scherg, 1990). For each source, the spatial filter is designed in a way that it tries to fully recover the source activity at the respective brain area, whereas activation from different regions in the brain is completely suppressed (Scherg et al., 2002). The data matrix D for the recorded signals at scalp surface is described as a linear overlap of N active sources at the respective position r and source waveform S_n.

$$D = \sum^{N} L(r,n)S_n + noise \tag{3.3}$$

The temporal activity pattern of each source can be reconstructed by inverting the leadfield matrix $L(r,n)$:

$$S_n = L^{-1}(r,n)D - L^{-1}(r,n) * noise \tag{3.4}$$

Each row of the spatial filter L^{-1} is a linear operator reconstructing one source waveform.

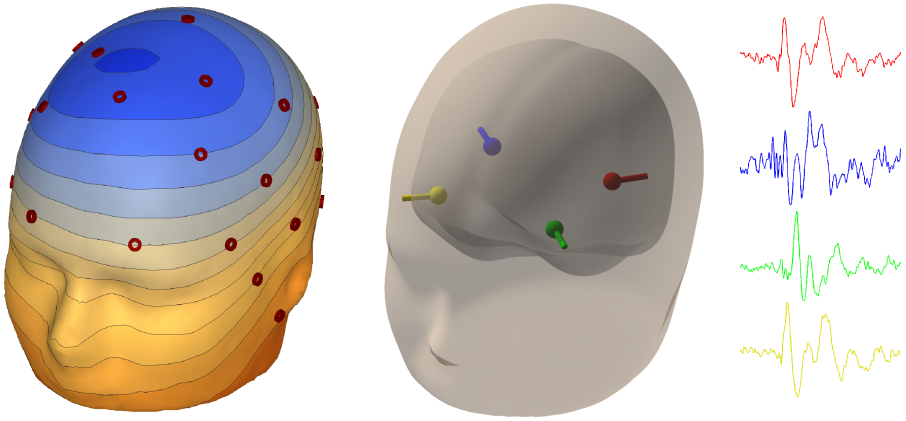

Figure 10: Transformation of an EEG recording to source space using a source montage. The topographic map (left) shows the voltage surface distribution for a single time-point. A brain source montage with 4 current dipoles (middle) is used to separate the spatially and temporally overlapping surface signals. The resulting source-waveforms (right) represent the time-varying activity pattern for each of the modelled brain regions.

The application of source montages enables to minimize effects on connectivity estimators that may occur during forward modelling and inverse source reconstruction. This is essential for single simulation runs that focus on a parameter that is not associated with source analysis. On the other hand, this approach offers the option to incorporate parameters that are relevant for inverse source reconstruction and to simulate errors in the estimated localization and orientation of active cortical regions.

Like in the forward modelling process, the volume conductor model used for source

Table 3.1

Taxonomy of connectivity methods implemented in the simulation architecture.

	Model-free	Model-based
Functional Connectivity	Amplitude correlation	
	Power correlation	
	Coherence	Coherence (MVAR)
	Phase-Locking Value	Phase-Locking Value (MVAR)
	Pairwise-Phase Consistency	
Effective Connectivity	Imaginary Part of Coherency	Imaginary Part of Coherency (MVAR)
		Granger Causality
		Granger Causality (MVAR)
		Directed Transfer Function
		Directed Transfer Function (MVAR)
		Partial Directed Coherence
		Partial Directed Coherence (MVAR)
		squared Partial Directed Coherence
	Phase-Slope Index	Phase-Slope Index (MVAR)

reconstruction can be selected from several types of head models. It should be noted that the simulation architecture supports selecting different head models for forward modelling and inverse source reconstruction to simulate modelling errors produced by the differences between the volume conductor models. Further deviations, including skull thickness and electrical conductivities of the head tissues, can be included in simulation runs. This serves the purpose of creating realistic simulations as in practice, the volume conductor model can only be an approximation of the true head volume conductor.
Inverse source reconstruction of simulated neurophysiological data using source montages was performed in BESA Research 6.1 (BESA GmbH, Germany).

3.3 Connectivity Analysis

Estimation of connectivity measures is performed on the source waveforms of active cortical regions. The systematic analysis includes functional as well as effective connectivity estimators. Both types of estimators can be further subdivided into model-free methods and measures that build upon a certain model. Model-based methods make assumptions regarding the interaction between signals. This includes autoregressive (AR) modelling as well as the statistical concept of Granger causality. Table 3.1 provides an overview on the categorization of connectivity analysis methods used in the simulation architecture.
All methods based on AR modelling use a a stepwise least squares estimation to compute coefficients of the MVAR model. The model order is chosen as the optimizer of Schwarz's Bayesian Criterion (Schwarz, 1978).

Reconstructed source waveforms of active brain regions were split up into trials of 2 s for connectivity estimation. It should be noted that the performance of connectivity estimates are biased by epoch length. The severity of the effect depends on the properties of the underlying data set and varies for different methods as shown in previous studies (Vinck, Oostenveld, van Wingerden, Battaglia, and Pennartz, 2011, Chu et al., 2012, Bonita et al., 2014, Fraschini et al., 2016).
The results of a connectivity estimation are visualized as a square matrix of graphs with number of sources columns and rows, as shown in figure 11. Each graphs displays the connectivity spectrum (y-axis) for each frequency (x-axis) between the two respective sources.

3.4 Performance Measures and Statistical Evaluation

After reconstructing the simulated brain network using different connectivity methods, it is important to assess whether and to what extent the simulated connections between cortical areas have been correctly recovered. Moreover, particular attention should be given to spurious connectivity, indicating wrongly reconstructed links between areas that are have not been defined in the simulated network. Figure 11 shows the connectivity spectra of Granger causality for a cortical network of 4 sources. Spectra calculated before forward modelling are indicated in blue, whereas spectra estimated after inverse source reconstruction are indicated in red.

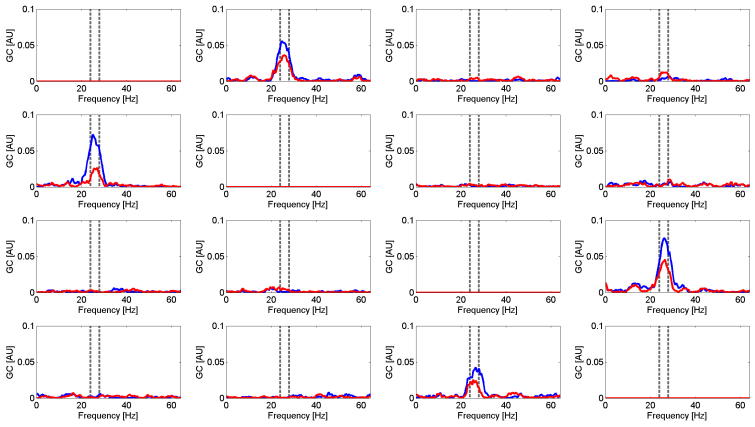

Figure 11: Comparison of connectivity spectra for Granger causality of simulated brain network (blue) and reconstructed network (red). The network comprised 4 active brain regions with a frequency interval of interest of 24 Hz to 28 Hz, indicated by the grey dashed lines.

Connectivity matrices (also known as correlation matrices) of the simulated and the reconstructed network measuring the performance of each single connectivity method

can incorporate methodological errors that may ultimately lead to considerable deviations in the connectivity estimation. Comparisons among methods are therefore difficult and must be interpreted only with great caution. To prevent and limit method-based errors, it is necessary to introduce a ground truth matrix. This binary matrix points out connected and unconnected nodes as defined in the configuration, at the start of each simulation experiment. Before applying statistical measures, connectivity spectra of the simulated network are multiplied with the ground truth matrix to set all spectra for unconnected pairs of network nodes to zero.

To measure the performance of each connectivity estimator, two approaches were implemented with both of them emphasizing different aspects of reconstructed networks. One important feature to depict cortical networks by analysing multi-channel recordings is to identify links between network nodes. For this reason, a performance measure was introduced to evaluate the reconstruction rate in terms of a binary classifier.

It should be noted that inverse source reconstruction and connectivity analysis are considering exactly the same number of active cortical areas that were used to generate the respective electromagnetic recording. This provides an equivalent representation of all nodes between simulated and reconstructed networks and allows a comparison of each pair of nodes.

A measure of correctly or incorrectly identified network links offers only a binary classification and therefore does not consider the coupling strength between two sources. It also means that incorrectly identified links are graded in the same way, independently of the strength of the network connection. For this reason, a second measure is calculated that also takes the connectivity matrices of the simulated and reconstructed network into account. The two performance measures are introduced in the following sections.

3.4.1 Binary Classification Testing

The first performance measure focusses on the correctly or incorrectly identified network links between two nodes of the reconstructed network and compares them to the ground truth of the simulated network across a range of thresholds. This method provides a binary classification and is similar to the performance measurement as introduced by Drakesmith (Drakesmith, 2012). The true positive rate (TPR) and false positive rate (FPR) were calculated from the comparison of both networks thresholded at 100 equally spaced values from the minimum to the maximum values in the connectivity matrix. TPR measures how many true positive results arise among all positive results, whereas FPR specifies the ratio between false positive results and all negative results. For each threshold level, the receiver operating characteristic (ROC) curve was created from the values provided by both metrics. Finally, to summarize the ROC curve into a single number, the area under the ROC curve (AUC) was calculated integrating the ROC curve using the trapezoidal

rule. The resulting value quantifies the ability of the test to distinguish between network reconstructions. Multiple iterations of each simulated scenario need to be carried out to obtain reliable results for AUC values and to be able to estimate their variance. Therefore, one of the first simulations must aim at determining the required number of iterations for subsequent experiments. Results of AUC values for each connectivity estimator are visualized using boxplots. An example of AUC results for Granger causality are shown in figure 12.

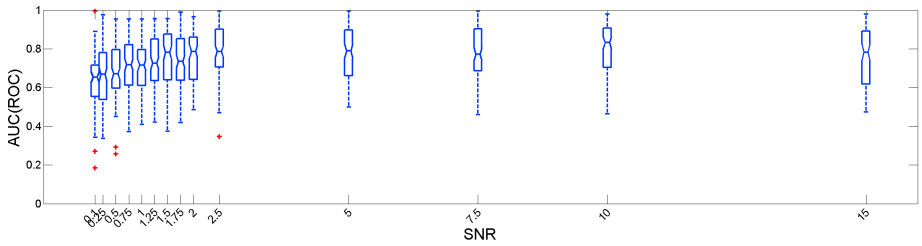

Figure 12: Result of AUC for Granger causality over varying SNR levels. The central mark in each box indicates the median and the bottom and top edges of the box indicate the 25th and 75th percentiles, respectively. The whiskers extend to the most extreme data points not considered outliers. Outliers are plotted individually using the '+' symbol.

3.4.2 Frobenius Norm

The performance indicator based on binary classification outlined in the previous section constitutes an important input to estimate the quality of a reconstructed network. A disadvantage of this binary categorization is the fact that incorrectly identified links are graded in the same way, not taking the coupling strength between two sources into account. As a consequence, links between sources with very low connections strength are valued in the same way as links with a high correlation, even though they are not of equal importance for the entire network.

For this reason, a second measure is calculated that also takes the connectivity matrices of the simulated and reconstructed network into account. This measure is based on the Frobenius norm (also known as Schur norm) outlined by Astolfi et al. (Astolfi et al., 2007). It is a matrix norm derived from the Euclidean norm. The Frobenius norm of a $m \times n$ matrix A is defined as the square root of the sum of the absolute squares of its elements

$$\|A\|_F = \sqrt{\sum_{i=1}^{m} \sum_{j=1}^{n} |a_{ij}|^2} \tag{3.5}$$

To measure a connectivity estimators performance of correctly reconstructing cortical networks, the Frobenius norm is calculated between the simulated connectivity matrix A^{pre} (defined at the start of the respective experiment) and the connectivity matrix A^{post} for the reconstructed network, estimated after forward modelling and inverse source reconstruction.

The distance measure providing a quality indicator of network reconstructions can then be expressed as

$$\|A^{pre}(\bar{f}) - A^{post}(\bar{f})\|_F = \sqrt{\sum_{i=1}^{m}\sum_{j=1}^{n} |a_{ij}^{pre}(\bar{f}) - a_{ij}^{post}(\bar{f})|^2} \tag{3.6}$$

with $a_{ij}(\bar{f})$ specifying the mean connection strength from source i to source j in the frequency band $\bar{f}$.

3.4.3 Analysis of Variance

Both performance measures, AUC and Frobenius norm, enable the classification of the efficiency and precision of connectivity estimators. In combination with visualizing results using boxplots, a comparability among different connectivity methods for varying parameters (e.g. SNR, data-length, etc.) can be achieved. However, it does not become sufficiently clear whether there are significant differences between distinct methods or parameter values, since this graph does not serve as qualitative evidence on their statistical difference. In order to be able to compare the quality of results and to draw conclusions on systematic effects or random fluctuations, it is necessary to apply further statistical methods analyses.

Analysis of variance (ANOVA) for a single variable (one-way ANOVA) and multiple, categorical independent variables (two-way ANOVA) were implemented based on results from AUC and Frobenius norm to gain such mathematical proof. One-way ANOVAs were used to determine whether there are any statistically significant differences between the means of two or more samples. Subsequently, post-hoc tests are carried out to identify the significance of detected differences. To examine the influence of two or more different independent variables (e.g. effect of SNR levels and connectivity methods), two-way ANOVAs need to be applied to reveal not only the main effect of each independent variable but also if there is any interaction between them.

Chapter 4

Simulations

In this chapter, the performance of functional and effective connectivity estimators under several conditions is evaluated. Various simulation runs are performed to assess the effect of specific parameters that are of vital importance during the simulation, preprocessing and analysis of realistic EEG recordings. A statistical analysis, as introduced in section 3.4, is applied to the results obtained in each of the experiments to point out significant differences and characteristics of the connectivity estimators.

Nine simulation experiments are presented in this chapter. Section 4.1 evaluates the required number of iterations for each simulation run to obtain robust and stable results. In section 4.2 the influence of the signal-to-noise ratio (SNR) is shown. The simulation run outlined in section 4.3 takes multiple data lengths into account and tests the effectiveness of connectivity estimators over varying data intervals. Section 4.4 considers source connections with different phase shifts. The sections 4.5 and 4.7 deal with the positions of cortical sources and investigate the differences between random source positions versus fixed source positions for each iteration (section 4.5) and demonstrate the influence of source localization errors on connectivity estimators (section 4.7). The main focus of the experiment presented in section 4.6 is put on the regularization constant (RC) used during inverse source reconstruction. Section 4.8 considers networks with varying numbers of active cortical sources and connections between them. The last simulation covered by this chapter (section 4.9) evaluates the effect of varying numbers of sensors that are taken into account during inverse source reconstruction.

Each of the following chapters, describing single simulation experiments, are divided into three parts: the *"Simulation Setup"* section describes the selected parameters of the respective simulation, for example the number of network sources or the head model used for forward modelling or inverse source reconstruction. It should be noted that some key parameters are not kept constant, but vary due to deviating conditions and requirements between experiments. For example, regularisation may be changed to improve source analysis for different networks. The common set of connectivity estimators, that are

assessed for each of the eight experiments, are coherence, DTF, PDC and Granger causality. Besides, the simulations analysing the effect of SNR (section 4.2), data length (section 4.3) and phase shifts (4.4) also evaluate the performance of imaginary part of coherency. The findings of connectivity estimation comparing the simulated and the reconstructed network are presented in the *"Results"* section. Moreover, this part of each simulation chapter also shows the outcome of Frobenius norm and AUC visualized using boxplots. Conclusions and implications with regard to the respective focus of the particular simulation run are outlined in the *"Discussion"* section.

4.1 Simulation I - Convergence and Stability

The first simulation scenario is used for verification and calibration of the entire simulation pipeline, as well as to determine the required number of iterations per simulation run to produce reliable and reproducible results. Furthermore, this is also essential for defining settings and preferences for future simulations.

Simulation Setup

The simulated cortical network consisted of four dipoles as shown in figure 13. Sources one and two were connected in a frequency range of 24 Hz to 28 Hz using a common band-pass filtered Gaussian noise signal, whereas the sources three and four remained unconnected. The coordinates and orientations of each source are listed in table A2. To simulate cortical background noise, 20 noise sources, carrying white noise signal, were distributed in the brain space.

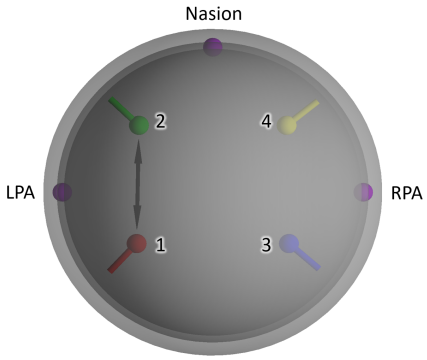

Figure 13: Top view of head model and network used in simulation I - Convergence and Stability. The network consists of four nodes with a bidirectional connection between sources one (red) and two (green). A concentric three-shell (brain, skull and scalp compartment) head model was used for forward modelling and inverse source reconstruction. Fiducials (nasion, left and right pre-auricular points) are indicated as purple spheres.

Forward modelling and inverse source reconstruction was performed based on a three-shell head model (see figure 13) defining the brain, skull and scalp compartments with conductivity values of 33 mS/m, 0.40 mS/m and 33 mS/m, respectively. EEG potentials at 31 scalp electrodes were simulated with 13 SNR values ranging from 0.1 to 15. The labels and coordinates of the EEG sensors are indicated in table A9. Each simulated data set has a total length of 100 s at a trial length of 2 s and a sampling rate of 256 Hz.
Inverse source reconstruction was realised using a source montage with identical dipole positions and orientations as used for forward modelling to avoid errors due to mislocalization of active cortical regions. A regularization factor of 5% was applied.
For the number of iterations, 11 levels (10 iterations to 200 iterations) were chosen to

determine the required number of iterations for future simulations. In each iteration, a data set with the characteristics mentioned above was generated and analysed. An overview on the settings for this simulation is shown in table 4.1.

Table 4.1

Overview of key parameters and settings for simulation I - Convergence and Stability. The parameter examined in this simulation is indicated in bold type.

Parameter	
Data length	100 s
Signal-to-noise ratio	0.1 - 15
Number of network nodes	4
Number of noise nodes	20
Number of electrodes	31
Number of iterations	**10 - 200**
Head model	Concentric three-shell
Regularization	5%
Localization error	0 mm
Connectivity methods	Coherence, DTF, PDC and GC

Results

In this section, the results of Frobenius norm and AUC values for multiple number of iterations levels are shown using boxplots. It is assumed that the quality of network reconstruction depends on the quality of the simulated EEG signal. Therefore, results with different SNR levels are shown in the following boxplots. The assumption that there is a correlation between the SNR of a simulated recording and the quality of a network reconstruction needs to be verified in a subsequent simulation run.

Figure 14 shows Frobenius norm over multiple number of iterations levels (10 to 200 iterations per run) for several signal-to-noise ratios (Figure 14a: 0.1, figure 14b: 0.5, figure 14c: 1, figure 14d: 10). Connectivity methods are colour-coded: coherence (red), DTF (orange), PDC (green) and Granger causality (blue).
Frobenius norm results demonstrate that the performance of network reconstructions depends on the number of iterations per simulation run, the SNR of the data set, but also on the respective connectivity measures that are applied. As already mentioned above, the effect of SNR will be looked at in more detail in a subsequent simulation run. However, it must be noted that network reconstructions greatly improve for higher SNR values, particularly for coherence and to some extent also for DTF and PDC. Granger causality, on the other hand, provides robust and reproducible results even for lower SNR values.

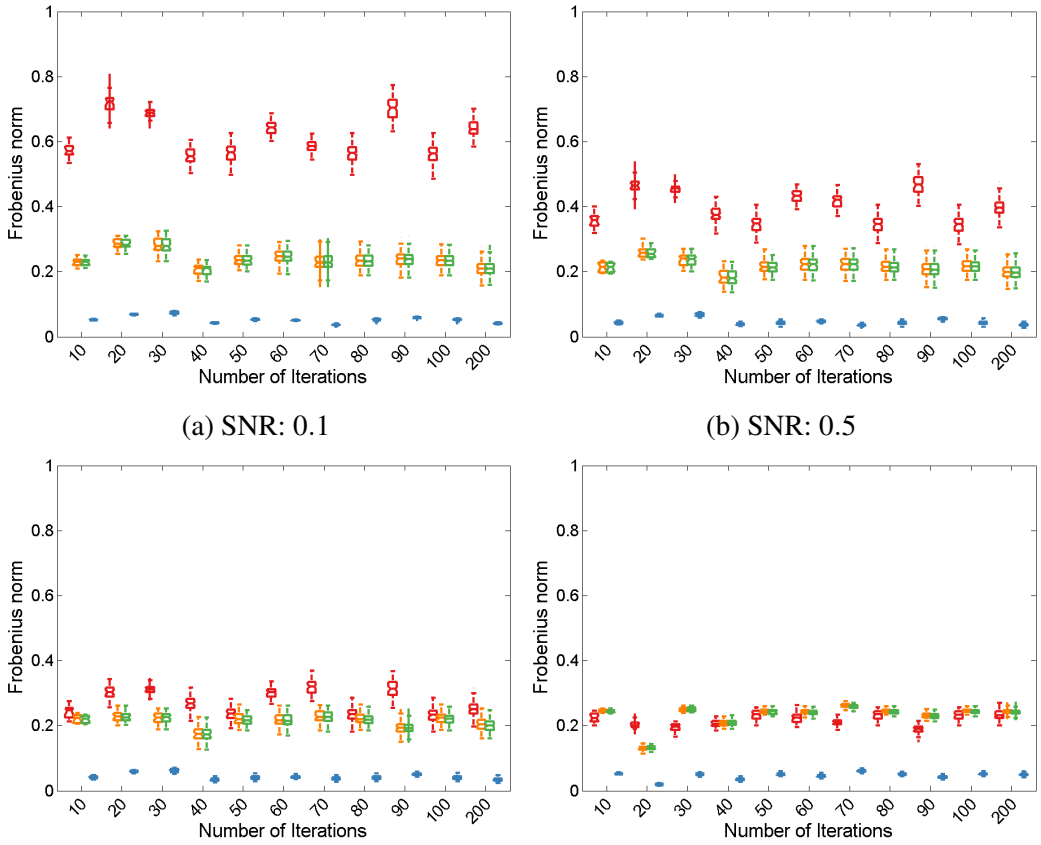

(a) SNR: 0.1

(b) SNR: 0.5

(c) SNR: 1

(d) SNR: 10

Figure 14: Frobenius norm over number of iterations for coherence (red), DTF (orange), PDC (green) and Granger causality (blue). Each sub-plot depicts the results for a specific SNR: a) 0.1, b) 0.5, c) 1, d) 10. For illustration purposes, boxplots of connectivity estimators are slightly offset for the respective number of iterations.

When focusing on the required number of iterations, the skewness pattern of each single boxplot indicates whether a major part of all observations are concentrated on one end of the scale, or whether results are evenly distributed, indicating a sufficient number of iterations. This is of particular importance for lower SNR values, as illustrated by results of coherence in figure 15a (SNR: 0.1). For a small number of iterations (10 to 70 iterations), the median does not symmetrically split the interquartile range (IQR). A similar pattern can also be found for DTF for 10 to 40 number of iterations, although the effects are not as profound as they are for coherence since the value range of DTF is more narrow. Results of PDC are almost identical to results of DTF. For Granger causality, such a differentiation between varying number of iterations is not possible, as results strongly converge, even for only 10 iterations and show an extremely limited range. The spread of results, represented by the vertical distance between the smallest value (lower whisker) and the largest value (upper whisker), including outliers, is independent of the number of iterations. However, results show a growing convergence as the range of observations decreases with higher SNRs.

An equivalent visualization for area under ROC curve (AUC) visualizing results of

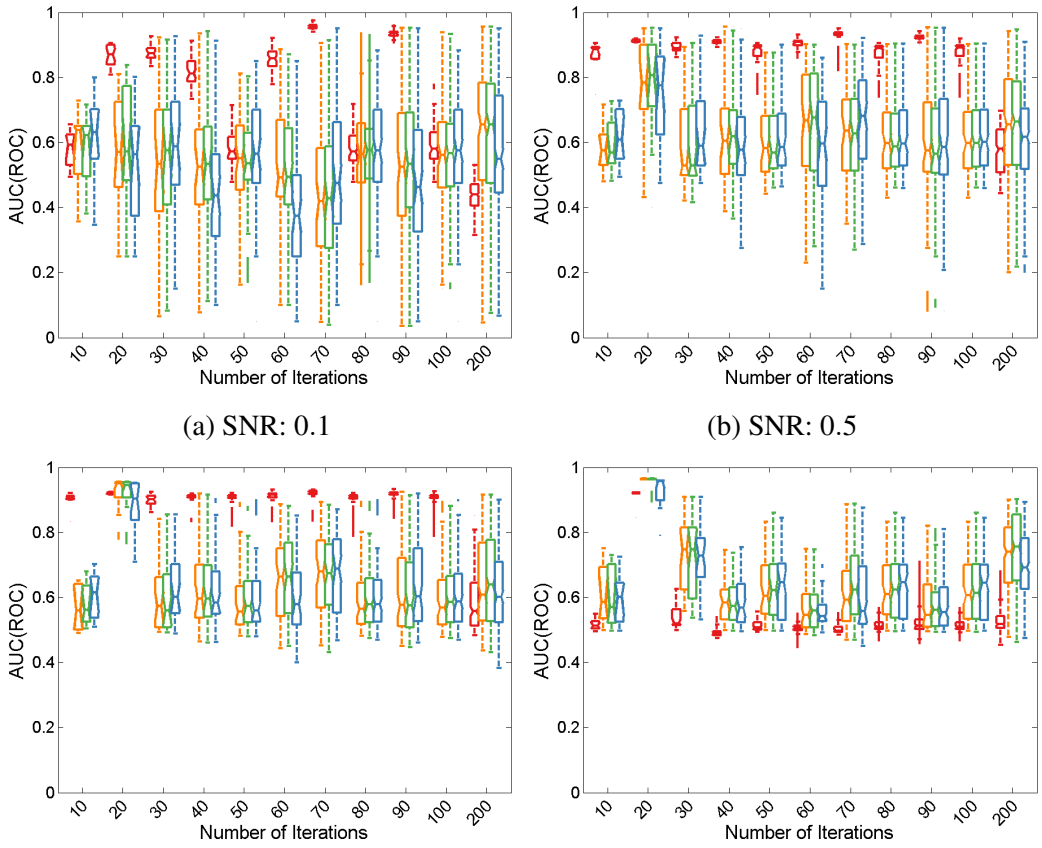

(a) SNR: 0.1

(b) SNR: 0.5

(c) SNR: 1

(d) SNR: 10

Figure 15: Area under ROC curve over number of iterations for coherence (red), DTF (orange), PDC (green) and Granger causality (blue). Each sub-plot depicts the results for a specific SNR: a) 0.1, b) 0.5, c) 1, d) 10.

coherence, DTF, PDC and Granger causality for several SNRs over number of iterations is presented in figure 15. However, AUC boxplots cannot be assessed and interpreted as intuitively as Frobenius norm boxplots. Since AUC is based on the ROC curve that is formed by plotting the sensitivity (true positive rate) and specificity (true negative rate) of the classifier against each other as a function of a threshold criterion, the AUC and both statistical performance measures of a binary classification test are subject to the same degree of uncertainty.

Despite the difficult interpretability of AUC boxplots, parallels can be drawn between the results emerging from Frobenius norm and AUC. In line with evidence from Frobenius norm, the median does not evenly divide the IQR for smaller number of iterations (from 10 up to 60 iterations). This effect becomes particularly apparent for lower SNRs (0.1 and 0.5). Moreover, the distance between the opposite ends of the whiskers, indicating the data range, is stable across varying number of iterations for a constant SNR. In contrast an increase in SNR will lead to a decrease in data range.

In addition to the visualization of results using boxplots, it is essential to take a look at

the connectivity spectra of simulated and reconstructed networks for each connectivity estimator to be able to critically assess and validate the results of AUC and Frobenius norm. Figure 16 shows connectivity spectra for the information flow from source 1 to source 2 for coherence, DTF, PDC and Granger causality.

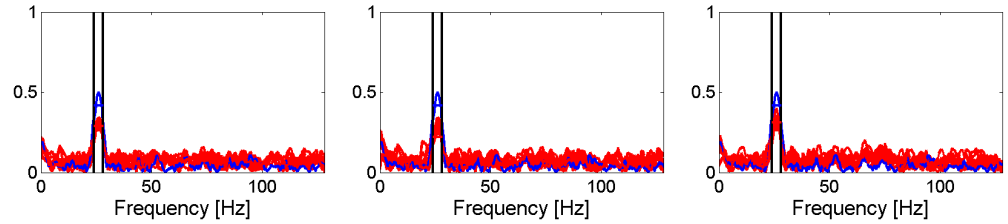

(a) Connectivity spectra of coherence for 10 (left), 50 (middle) and 100 (right) iterations.

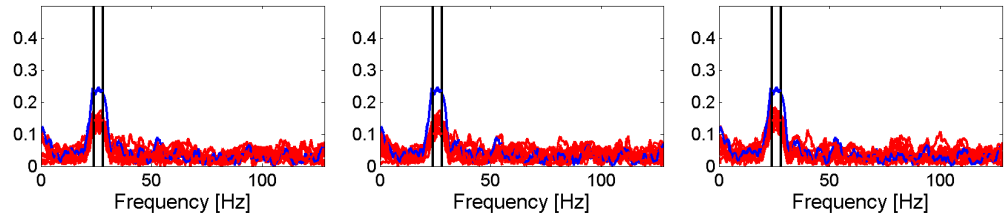

(b) Connectivity spectra of DTF for 10 (left), 50 (middle) and 100 (right) iterations.

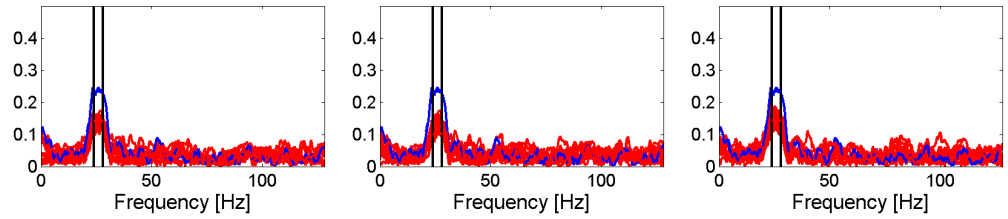

(c) Connectivity spectra of PDC for 10 (left), 50 (middle) and 100 (right) iterations.

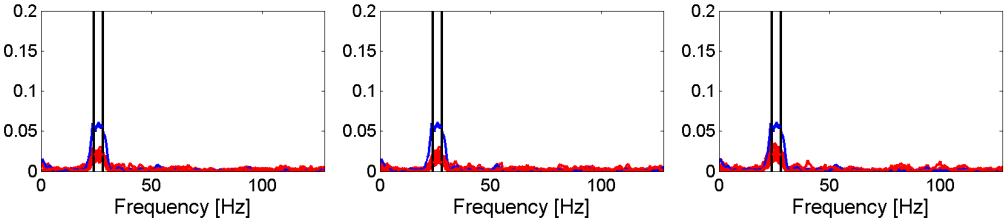

(d) Connectivity spectra of Granger causality for 10 (left), 50 (middle) and 100 (right) iterations.

Figure 16: Connectivity spectra of simulated (blue) and reconstructed (red) networks for coherence, DTF, PDC and Granger causality indicating the information flow between source one and source two. Spectra were retrieved from data sets of 100 s length and an SNR of 0.5.

The graphs show high connectivity in the frequency range of interest (24 Hz to 28 Hz) only and are stable among different number of iterations. Connectivity values of reconstructed networks (red) almost reach the same level as for the simulated networks (blue) indicating a high quality of network reconstructions. Furthermore, the level of connectivity values outside the frequency range of interest are rather low and enable an effortless identification

of correlated sources within certain frequency bands even for a visual inspection of the connectivity spectra by the researcher.

Discussion

The goal of this simulation was not necessarily to point out similarities and differences of connectivity measures or to evaluate which estimator performs best for different number of iterations, rather than to identify a tangible number of iterations that enables reliable and converging results for all connectivity estimators used in the simulations. Since subsequent simulation scenarios will cover a wide range of SNR values, data lengths and other values affecting the performance of each method, it is vital to choose a high number of iterations to obtain trustworthy results also for complex cases with low SNRs and short data sets.
Results of Frobenius norm, as well as AUC, show that coherence requires a larger number of iterations than DTF and Granger causality to attain exact and reliable results. To avoid the assignment of varying numbers of iterations for different connectivity estimators in succeeding simulation experiments, which might adversely affect the statistical analysis and interpretation of results, a highest common denominator must be determined. For all configurations that were examined in this simulation run, a number of iterations of 100 proved to be more than sufficient to obtain reproducible and consistent results. Moreover, it provides enough margin for subsequent simulations to retrieve accurate results when analysing shorter data sets.

4.2 Simulation II - Signal-to-Noise Ratio

In this experiment, it is examined whether and to what extent the performance of connectivity estimators is affected by the characteristics and quality of electrophysiological recordings. The key parameter to generate and evaluate data with predefined properties in this simulation scenario is the signal-to-noise ratio (SNR).

Simulation Setup

This simulation used a similar brain network consisting of four dipoles as introduced in section 4.1. However, the information flow between sources was slightly modified. Connections from source one to two and from source three to four were modelled in the frequency range of 24 Hz to 28 Hz with a phase-delay of 9.6 ms between connected areas. The dipole positions and network connections are illustrated in figure 17. The detailed settings for this experiment are listed in table 4.2.

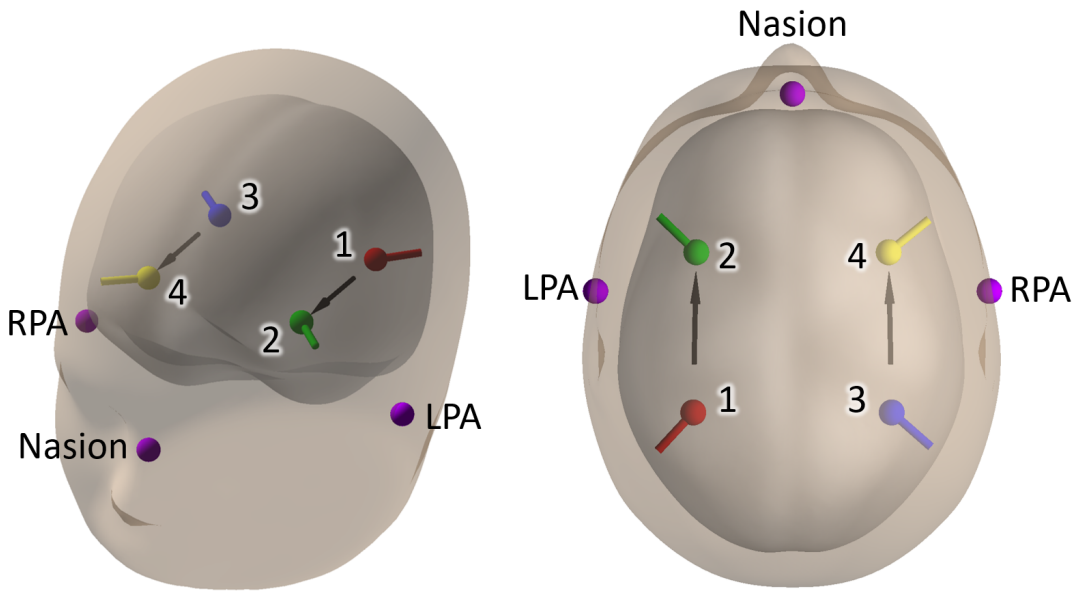

Figure 17: Head model, dipole locations and network connections used in simulation II - Signal-to-Noise Ratio. Information flow from source one (red) to two (green) and from source three (blue) to four (yellow) was simulated. A realistic standardised FEM head model (BESA Research 6.1) was used to perform forward modelling as well as inverse source reconstruction. Fiducials (nasion, left and right pre-auricular points) are indicated as purple spheres.

Cortical background noise was simulated by distributing 20 noise dipoles in the brain space. All noise sources carried white noise signals that were randomly generated for each of the 100 iterations. In order to estimate the effect of SNR on network reconstructions, the simulation was performed for 14 different SNR levels ranging from 0.1 up to 15. The

scaling of the noise topographies was carried out in the frequency domain after forward modelling activities from noise and network dipoles for 31 scalp channels, with sensor labels and positions outlined in table A9 in the appendix. Each data set consisted of a 100 s recording at a sampling rate of 256 samples per second.
Reconstruction of cortical activity was carried out based on a source montage with four dipoles located at locations and orientations equivalent to the simulated sources and a regularization factor of 2%.

Table 4.2

Overview of key parameters and settings for simulation II - Signal-to-Noise Ratio. The parameter examined in this simulation is indicated in bold type.

Parameter	
Data length	100 s
Signal-to-noise ratio	**0.1 - 15**
Number of network nodes	4
Number of noise nodes	20
Number of electrodes	31
Number of iterations	100
Head model	Realistic standardised FEM head model
Regularization	2%
Localization error	0 mm
Connectivity methods	Coherence, imaginary part of coherency, DTF, PDC and GC

Results

Boxplots of Frobenius norm (figure 18) and area under ROC curve values (figure 19) show a non-linear increase of accuracy over all connectivity methods with an increase of SNR. Above a certain threshold no further significant improvements in accuracy can be achieved. Results indicate that coherence methods are more strongly impaired by lower SNR levels (0.1 to 2) than other methods. As expected, and as a validation of the pipeline, simulations including directional information flow can be reproduced best by methods based on Granger causality.
Figure 18 indicates that Granger causality shows lowest Frobenius norm over the entire SNR range, even for poor signal-to-noise ratios (0.1 and 0.25), where all other methods generate significantly higher Frobenius norm results. As a result of the fact that Granger causality is least prone to noise, it shows less improvement for higher SNR values as other methods in absolute terms, but still provides slightly better network reconstructions for higher SNR. Frobenius norm for all methods converges towards a low limiting Frobenius norm value of

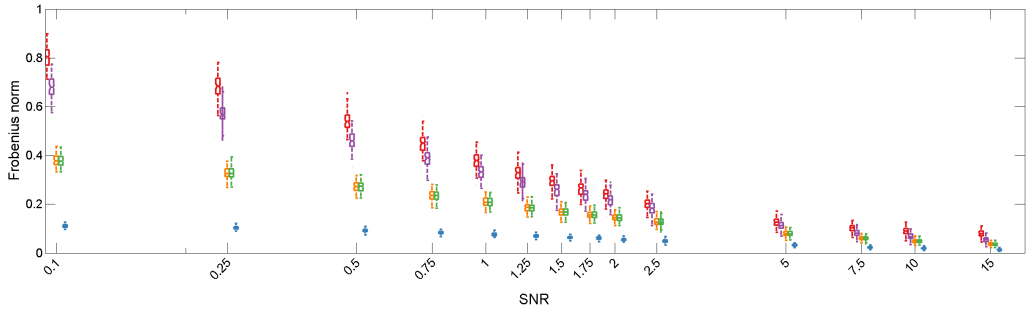

Figure 18: Semi-logarithmic plot of Frobenius norm over SNR for coherence (red), imaginary part of coherency (purple), DTF (orange), PDC (green) and Granger causality (blue) for 100 s data sets. For illustration purposes, boxplots of connectivity estimators are slightly offset for the respective SNR level.

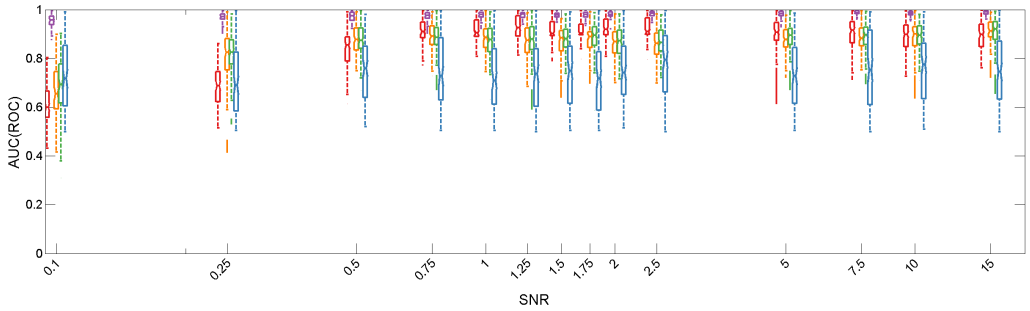

Figure 19: Semi-logarithmic plot of area under ROC curve over SNR for coherence (red), imaginary part of coherency (purple), DTF (orange), PDC (green) and Granger causality (blue) for 100 s data sets.

approximately 0.07 ± 0.02. Variance of results, indicated by the vertical distance between the lower and upper whisker also decreases for all methods for higher SNR values.

AUC results indicate higher accuracy of imaginary part of coherency compared to other methods over all SNR values, followed by coherence, DTF and PDC. However, due to the simple binary classification of the comparison between simulated and reconstructed network over multiple connectivity thresholds, the ROC is unable to distinguish between a correctly reconstructed connection between cortical areas in the frequency range of interest or a connection obtained by chance due to a generally high noise level over the entire frequency range. Connectivity graphs illustrate and highlight the quality of a network reconstruction and should be taken into account to draw conclusions when evaluating AUC, as well as Frobenius norm boxplots.

Figure 20 shows information flow from source one to source two and from source three to source four over the entire frequency range for the connectivity estimators coherence, imaginary part of coherency, DTF, PDC and Granger causality. The noise level for coherence is relatively large compared to noise level of Granger causality over the entire frequency range. For this reason, peaks identifying correlated sources for specific frequencies vanish, which makes a visual detection of connected or unconnected cortical areas rather

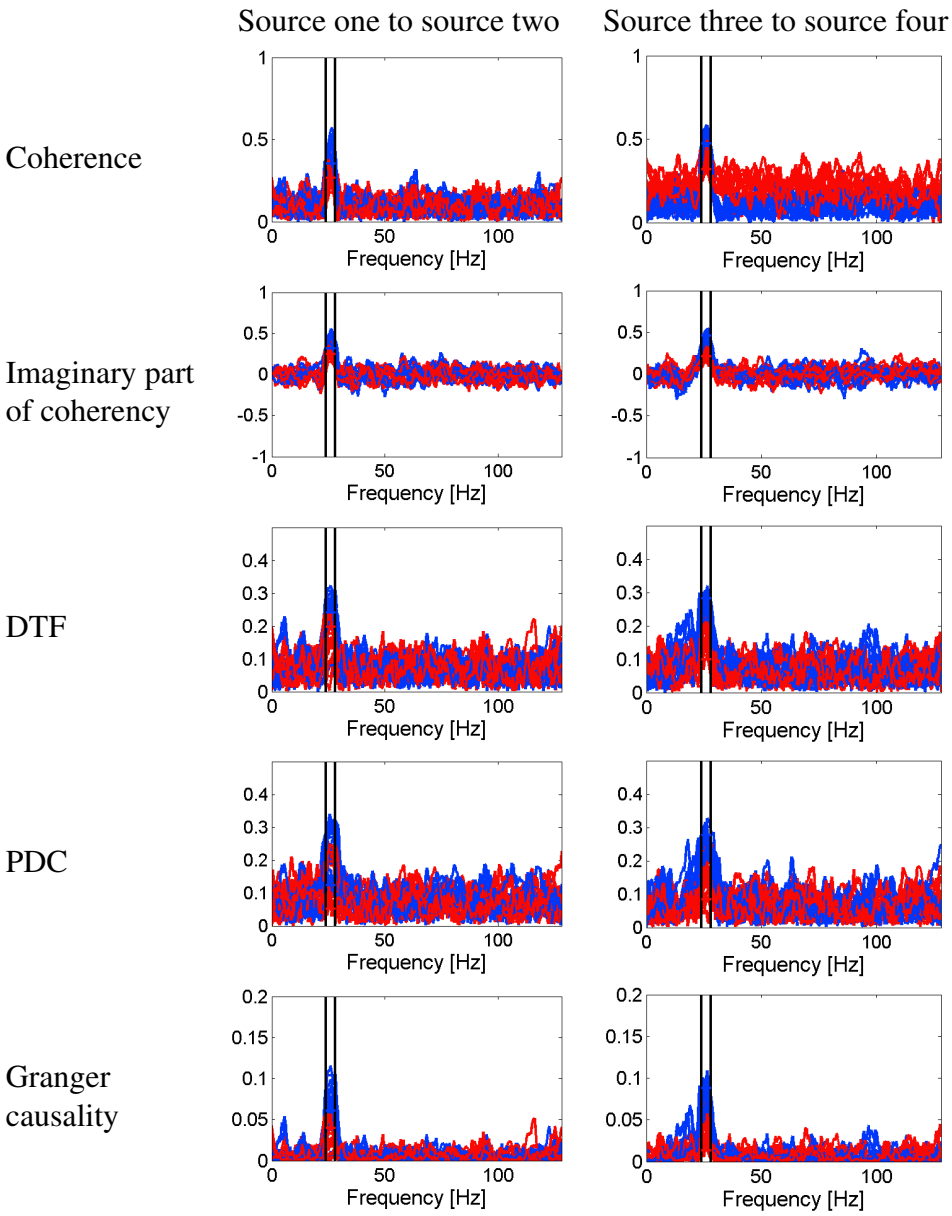

Figure 20: Connectivity spectra of simulated (blue) and reconstructed (red) networks for different connectivity estimators indicating the information flow from source one to source two (left column) and from source three to source four (right column). Spectra were retrieved from data sets of 25 s length and an SNR of 1.0.

complicated and error-prone. Spectra of DTF and PDC show higher noise level compared to Granger causality but provide a more sufficient degree of stability and accuracy than coherence. Results of imaginary part of coherency are substantially better than DTF or PDC, showing lower noise level over the entire frequency range and more prominent peaks for in the frequency band of interest. Imaginary part of coherency and Granger causality achieve comparable results. Differences between those two estimators are rather small and difficult to observe.

The output value range of Granger causality depends on the analysed data set and

computational settings. In this case, Granger causality provides relatively low connectivity values, but is still able to suppress noise outside the frequency range of interest. This robustness towards low SNR enables easier and more accurate determination of correlated sources compared to other methods.

Discussion

The results demonstrated in this simulation suggest that increasing SNR levels led to better network reconstructions for all tested connectivity estimators. To assess the advantages and disadvantages of each method, it is reasonable to divide the entire range of analysed SNR values into two intervals: low SNR values ranging from 0.1 to 2 and high SNR values ranging from 2.5 to 15. For higher SNR values, all estimators perform considerably better and are able to provide sufficient and reliable network reconstructions. Results of Frobenius norm show that the difference in network reconstruction between methods at high SNR values are very slight. Moreover, a further increase of SNR starting from a level of 2.5 led only to minor improvements in accuracy of network reconstructions.
On the other hand, this is in strong contrast to the results obtained for the low SNR range. Granger causality provides stable reconstructions out of data with poor SNR, whereas all other methods, in particular coherence and imaginary part of coherency, produce partially very different results. Furthermore, connectivity spectra of these estimators contain a high degree of noise over the entire frequency spectrum which makes it difficult to detect peaks of true information flow. However, these connectivity methods can effectively benefit from an increase in SNR and tend to converge towards a limiting value. For such an increase in SNR the difference between Granger causality and other estimators becomes less significant and noticeable.
This simulation clearly shows that the quality of data sets influence the choice of connectivity estimators. Consistent and robust network reconstructions for data with low SNR can be provided by imaginary part of coherency, Granger causality, DTF and PDC, whereas connectivity spectra obtained from coherence must be interpreted and evaluated with care.

4.3 Simulation III - Data Length

The previous simulation considered the effect of SNR on connectivity estimation for a fixed data length. The experiment presented in this chapter will add another aspect and examine the influence of data length with varying signal to noise ratio on connectivity estimators. The most important point of this analysis is the question whether it is possible to compensate for poor data with relatively low SNR by using longer data sets. Derived from this, provided that this statement can be confirmed, the question arises of how long data epochs with a given low SNR are required to retrieve similar results as compared to shorter data set with higher SNR.

Simulation Setup

The configuration of this experiment is identical to the simulation setup used for generating data of the SNR study in simulation II (chapter 4.2). Table 4.3 shows the chosen configuration for the current study. In this simulation, the framework was enhanced to also incorporate varying data length to generate recordings consisting of 2 s up to 200 s at a constant trial length of 2 s. The network consisted of 4 dipoles (see table A2) with 2 connections simulating information flow from source one to two and from source three to four. Like the simulation carried out in chapter 4.2, this simulation was performed for 14 SNR levels ranging from 0.1 up to 15 for each data length. 20 sources carrying white noise signals were distributed in brain space to simulate cortical background noise.
Inverse source reconstruction was performed using an equivalent source montage consisting of 4 dipoles and a constant regularization factor of 2%.

Table 4.3

Overview of key parameters and settings for simulation III - Data Length. The parameter examined in this simulation is indicated in bold type.

Parameter	
Data length	**2 s - 200 s**
Signal-to-noise ratio	0.1 - 15
Number of network nodes	4
Number of noise nodes	20
Number of electrodes	31
Number of iterations	100
Head model	Realistic standardised FEM head model
Regularization	2%
Localization error	0 mm
Connectivity methods	Coherence, imaginary part of coherency, DTF, PDC and GC

Results

The results of this simulation with varying data length found clear support for the assumption that longer data sets generally improve the accuracy and stability of network reconstructions. This applies to all connectivity estimators used throughout this experiment. Figure 21 shows Frobenius norm boxplots of coherence, imaginary part of coherency, DTF, PDC and Granger causality over logarithmic data lengths ranging from 2 s to 200 s at SNR values of 0.1, 1 and 10.

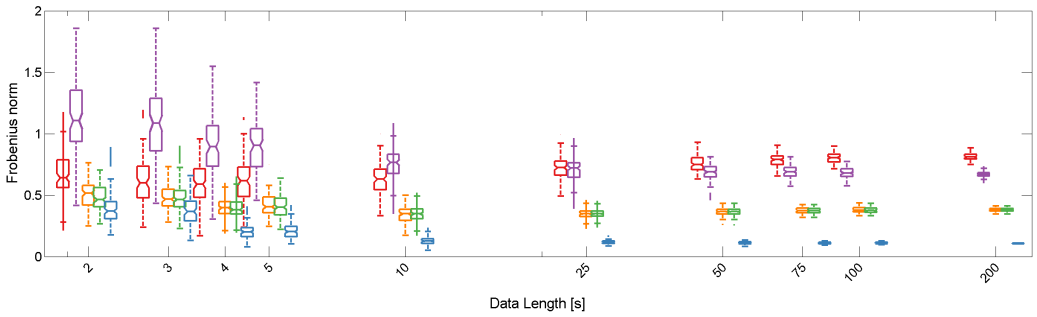

(a) SNR: 0.1

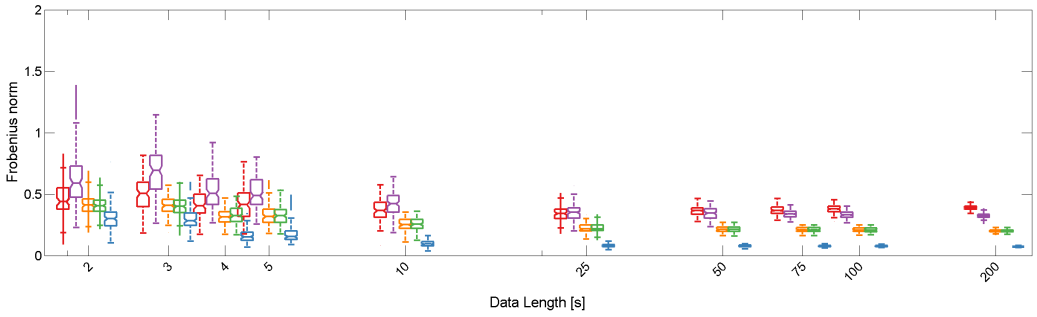

(b) SNR: 1.0

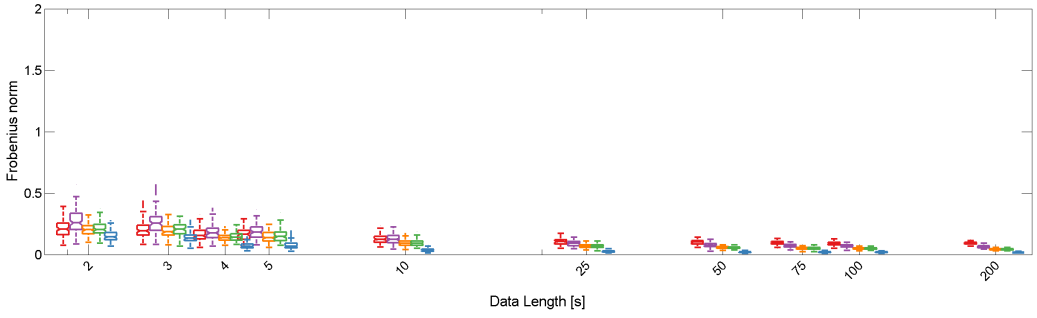

(c) SNR: 10

Figure 21: Frobenius norm over logarithmic data length for coherence (red), imaginary part of coherency (purple), DTF (orange), PDC (green) and Granger causality (blue) at different SNR levels (top: 0.1, middle: 1.0, bottom: 10).

This figure clearly shows that interquartile ranges (IQR) are reduced with longer epochs and higher SNR values for all methods. Particularly for long data sets of 100 s and 200 s, no differentiation can be made between various SNR levels as far as IQR is concerned. Consequently, it can be concluded that all connectivity algorithms provide more stable

results with an increase of data length.
Comparing the accuracy of a single connectivity method for several data lengths and SNR levels or between multiple connectivity estimators, it becomes obvious that there are considerable differences in how precise and consistent methods perform. For longer data sets, accuracy converges towards a certain limit, depending on SNR and connectivity method.
For coherence, longer data epochs cannot compensate for poor data quality (SNR: 0.1). The variation of reconstruction accuracy does decrease with longer data length, but an improvement in the average accuracy level is only feasible to a certain limit. Further optimization in network reconstruction is only possible with data sets of higher quality, implying a higher SNR. Results of DTF, PDC and Granger causality also tend to converge to a specific limit for increasing data length, however, this limit is significantly lower than that of coherence or imaginary part of coherency. This difference becomes less pronounced for data with higher SNR (SNR 10).
Results of Frobenius norm provide another case demonstrating that Granger causality outperforms coherence, imaginary part of coherency, DTF and PDC, since it is less strongly impaired by shorter data sets than other methods. Moreover, for methods like coherence and imaginary part of coherency long data epochs cannot compensate poor data quality.
Calculations of area under ROC curve (AUC) for this simulation are shown in figure 22. Equivalent to the illustration of Frobenius norm (figure 21), the boxplots present AUC over logarithmic data length for three SNR levels with a colour-coded classification of the corresponding connectivity estimators.
In line with previous simulations, AUC provides consistent, yet not entirely compatible results compared to Frobenius norm. With the exception of results for Granger causality, AUC indicates a decrease in variance and an increase in accuracy of connectivity reconstructions using longer data sets or data with higher SNR for all methods. Furthermore, figure 22 demonstrates that the accuracy of network reconstructions converges towards a certain limit and hence connectivity estimators will not continue to provide more accurate results by adding more data to the analysis.
AUC results for Granger causality suggest that this method is unable to correctly detect connections between distinct brain areas, since there is only negligible or no improvement in variance and accuracy for increasing SNR as well as for increasing data length. That is inconsistent with the results from Frobenius norm that showed a best overall performance for Granger causality. To resolve this contradiction, it is essential not only to concentrate exclusively on statistical results provided by Frobenius norm and AUC, but also to take a look at the corresponding connectivity spectra for each method. Figure 23 depicts the connectivity spectra of simulated (blue) and reconstructed (red) networks for coherence, imaginary part of coherency, DTF, PDC and Granger causality at three different data lengths

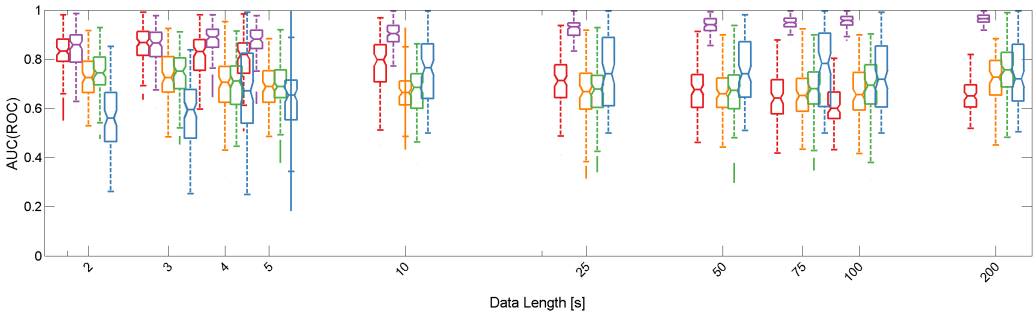

(a) SNR: 0.1

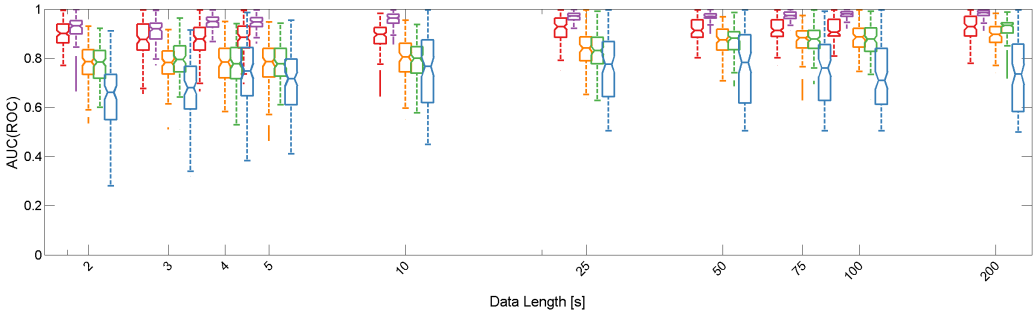

(b) SNR: 1.0

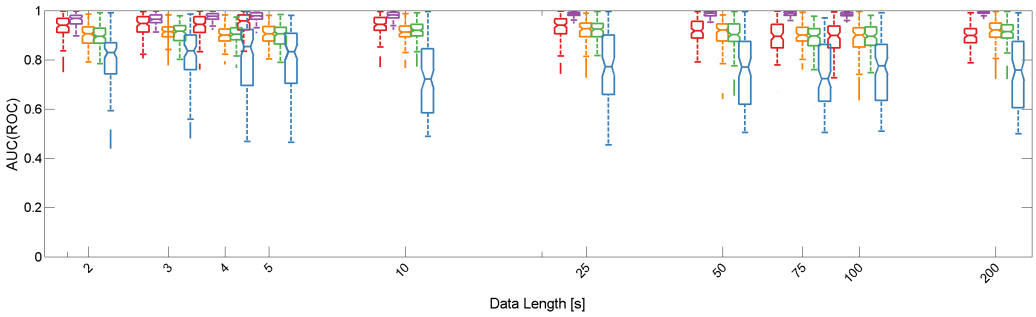

(c) SNR: 10

Figure 22: Area under ROC curve over logarithmic data length for coherence (red), imaginary part of coherency (purple), DTF (orange), PDC (green) and Granger causality (blue) at different SNR levels (top: 0.1, middle: 1.0, bottom: 10).

(left column: 10 s, middle column: 50 s, right column: 100 s) and a constant SNR of 1. Each individual graph shows the information flow from source three to source four over the entire frequency band, whereas the simulated link between the sources is apparent in the frequency range of 24 Hz to 28 Hz.

Since connectivity spectra are the basis for the statistical analysis of network reconstructions, they are directly related to the results of Frobenius norm and AUC and may support with their explanation and clarification.

Spectra of all methods show a significant decrease in variation of noise with higher data length for simulated as well as for reconstructed networks. For coherence, the average noise level does not completely decline when having more data available, instead it converges at a particular level depending on the SNR. This also explains the convergence of Frobenius

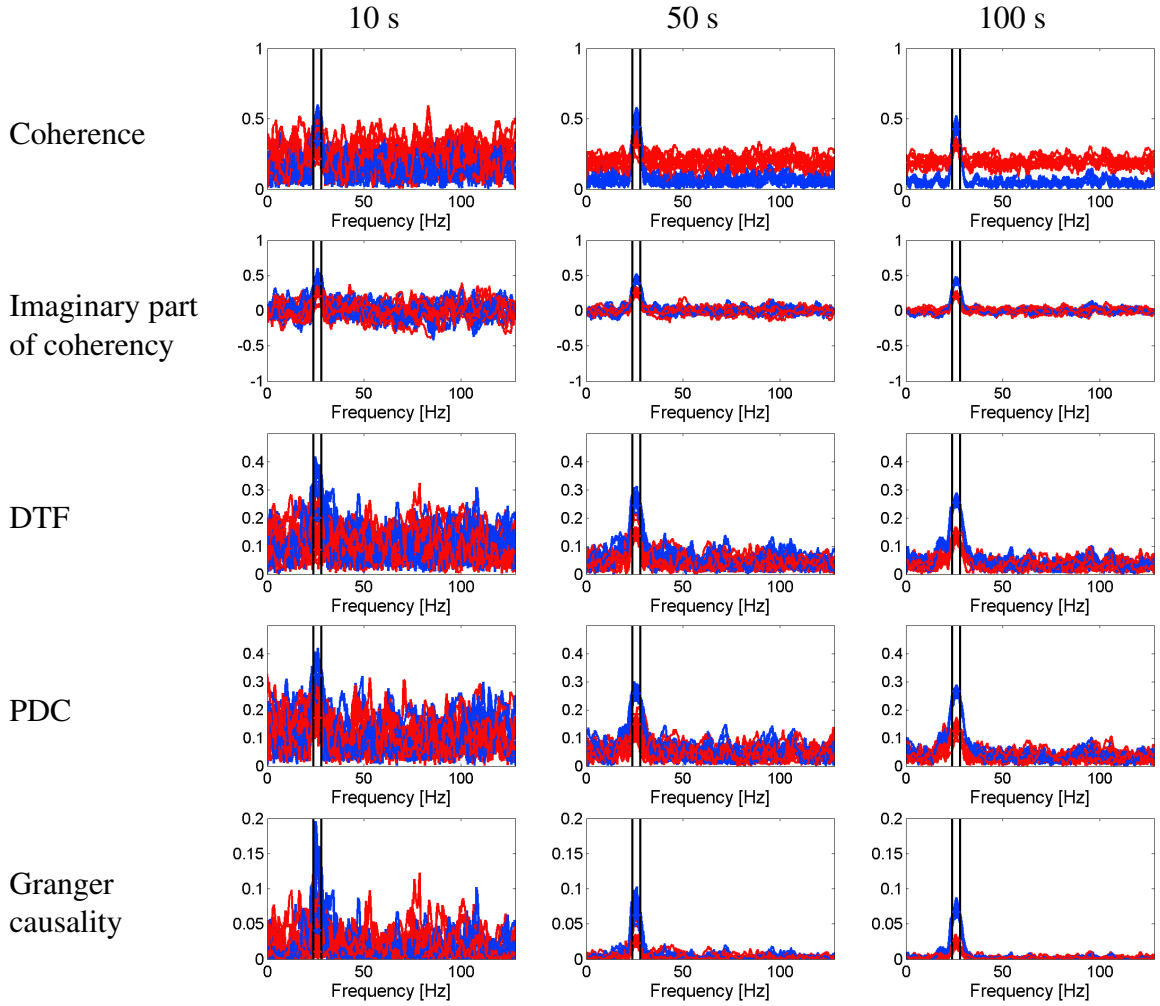

Figure 23: Connectivity spectra of coherence, imaginary part of coherency, DTF, PDC and Granger causality indicating information flow from source three to source four of simulated (blue) and reconstructed (red) networks at different data lengths (left: 10 s, middle: 50 s, right: 100 s) and constant SNR of 1.

norm and AUC at higher data lengths. To have the limit value reduced further, it is necessary to use data with higher SNR. Imaginary part of coherency, DTF, PDC and Granger causality are not affected by poor SNR values to that extent. Those estimators provide noisy connectivity spectra for short data sets (10 s), but both, the variance of the retrieved spectra and the average noise level are constantly reduced with longer data. The minimisation and suppression of noise in the connectivity spectra enables an effortless and accurate detection of peaks even via visual assessment. Whereas for coherence, the average noise level is too high for the peaks to protrude from the remaining spectrum.

The relatively poor performance of Granger causality shown in the results of AUC (figure 22) cannot be attributed to major deviations in the connectivity spectra between the simulated and reconstructed network. This imprecision of AUC resides more in the methodological limitations of the method based on the selection of the threshold that is chosen for the calculation of TPR and FPR and also due to the inaccuracy of the ROC curve for a large

ratio of negatives to positives (Clark and Webster-Clark, 2008). To compensate for this effect, Clark and Webster-Clark proposed the logarithmic receiver-operator characteristic curve as a method of scaling the ROC curve.

Discussion

Results of this experiment confirm and extend the findings revealed in the SNR simulation (section 4.2). The analysis found evidence that accuracy and stability of network reconstructions increase to a certain extent with longer data sets for all estimators. In particular the variance of connectivity spectra could be minimized constantly. However, it could also be clarified that long data epochs cannot compensate poor data quality.
Methods like coherence and imaginary part of coherency could only provide an improvement in the average accuracy level to a certain limit depending on the SNR. A further increase in accuracy was only possible with higher quality data sets. On the other hand, connectivity spectra of DTF, PDC and Granger causality, were able to benefit from longer data which lead to a minimisation and elimination of noise over the entire frequency range. This not only has the advantage of easier identification of information flow between distinct brain areas, but also avoids inadequate or incorrect evaluation.
Regarding the limitations of connectivity estimators to provide consistent and robust network reconstructions for data sets with low SNR, high importance must be attached to accurate and thorough data acquisition to obtain high quality data. A further argument in favour of data quality over quantity is the fact that it is generally not possible to refine connectivity results by simply providing longer data.

4.4 Simulation IV - Phase Difference

Previous simulations were based on networks with a fixed, predefined phase delay between correlated brain areas. For simulations SNR (section 4.2) and data length (section 4.3), a phase delay of 9.6 ms between sources with a simulated transmission of information was determined. This corresponds to a shift of 25% of the average cycle length (T) at an frequency range of interest from 24 Hz to 28 Hz.
In this simulation, it is examined whether there is a dependency between the performance of particular connectivity estimators and the duration of phase delays. Furthermore, the effect of lower or higher phase delays on results of network reconstructions will be evaluated.

Simulation Setup

The simulation included source activity emerging from four dipoles, that were placed in source space as shown in figure 17. To generate source waveforms, white noise signals were bandpass filtered, with filter boundaries ranging from 24 Hz to 28 Hz. For simulations including phase differences, one bandpass filtered signal of a pair of correlated source waveforms was shifted by a fraction ($0/8$, $1/8$, $2/8$, ... $7/8$) of the cycle length T of the average frequency of interest. For an average frequency of interest of 26 Hz, the duration of T is calculated according to

$$T = \frac{1000}{f_{avg}} = \frac{1}{26\,Hz} = 38.462\,ms \tag{4.1}$$

Consequently, the time-lag Δt between connected brain areas with a phase-shift of $1/8$ of the cycle length is

$$\Delta t_{1/8} = \frac{T}{8} \approx 4.81\,ms \tag{4.2}$$

A concentric three-sphere volume conduction model was used to model the measurable EEG potential at 31 electrode positions. The complete list of sensor labels including positions is shown in table A9. Each data set consisted of 100 iterations with 50 trials at a length of 2 s and a sampling rate of 256 samples per second. To add noise to the simulation, 20 dipoles that carried white noise signal were randomly distributed in source space. EEG potentials were likewise calculated by projecting these time-courses on the scalp based on the same head model and were scaled to obtain the desired SNR levels (0.1, 0.25, 0.5, 0.75, 1, 2, 2.5, 5, 7.5, 10 and 15).
As in previous simulations, reconstructing the time-dependent activity in cortical space was done using a discrete source reconstruction method: a source montage consisting of four network nodes was applied to retrieve the source waveforms for each active brain area. The position and orientation of each node was identical to the ones as used for forward

calculations. Finally, connectivity estimators were calculated to evaluate information flow between network nodes. The quality of each connectivity evaluation was rated using Frobenius norm and AUC. A list of parameters for the current experiment is given in table 4.4.

Table 4.4

Overview of key parameters and settings for simulation IV - Phase Difference. The parameter examined in this simulation is indicated in bold type.

Parameter	
Data length	100 s
Phase difference	**0/8 - 7/8**
Signal-to-noise ratio	0.1 - 15
Number of network nodes	4
Number of noise nodes	20
Number of electrodes	31
Number of iterations	100
Head model	Concentric three-sphere
Regularization	5%
Localization error	0 mm
Connectivity methods	Coherence, imaginary part of coherency, DTF, PDC and GC

Results

Frobenius norm results for the connectivity estimators coherence, imaginary part of coherency, DTF, PDC and Granger causality are illustrated in figure 24. Each subfigure shows the results of connectivity reconstructions for a specific phase difference between connected nodes, ranging from no phase shift (figure 24a) to a phase shift of $7/8$ of the cycle length (figure 24h).

Comparisons between results with phase differences shifted by a half wavelength of the frequency of interest ($0/8$ and $4/8$, $1/8$ and $5/8$, $2/8$ and $6/8$, $3/8$ and $7/8$) reveal that Frobenius norm values are on the same level for each pair within each method. Coherence and imaginary part of coherency constitute an exception to this pattern. For coherence, results for phase differences $1/8$ compared to $5/8$ and $3/8$ compared to $7/8$ differ from each other. Moreover, minor deviations can be determined for phase differences $0/8$ compared to $4/8$.

Coinciding with findings of previous simulations, DTF, PDC and Granger causality show consistent behaviour over all phase lags with only small changes in variance and only few outliers for lower SNR. In general, it can be stated that results of Frobenius norm, depicting the accuracy of network reconstructions, are stable over the entire range of SNR levels and

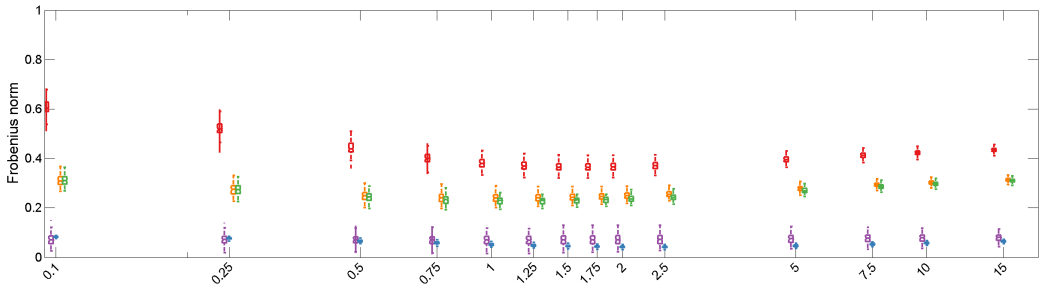

(a) Phase difference: $0/8$

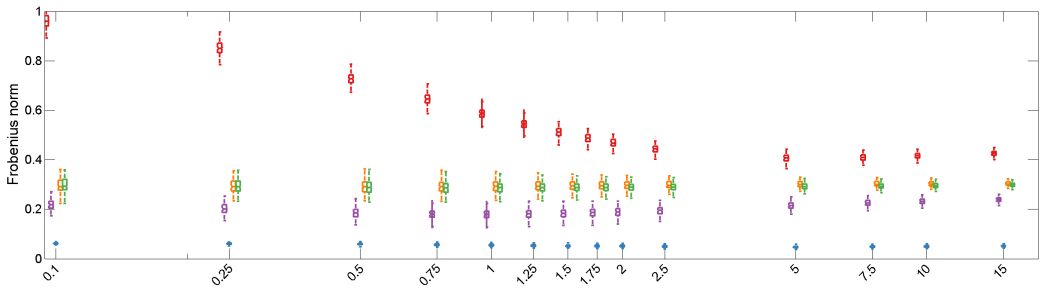

(b) Phase difference: $1/8$

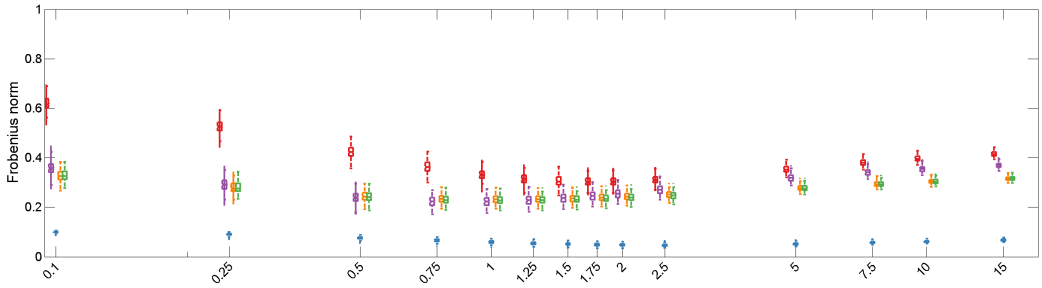

(c) Phase difference: $2/8$

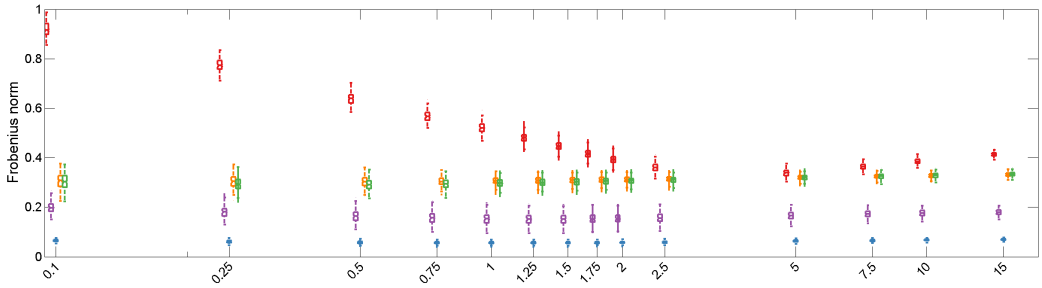

(d) Phase difference: $3/8$

Figure 24: Semi-logarithmic plot of Frobenius norm over SNR for coherence (red), imaginary part of coherency (purple), DTF (orange), PDC (green) and Granger causality (blue) at phase differences ranging from $0/8$ to $3/8$.

all phase differences.

Compared to Granger Causality, results of imaginary part of coherency are more variable, depending on the respective phase difference. For phase shifts of $0/8$, $3/8$, $4/8$ and $7/8$, imaginary part of coherency provides accurate and reliable results that are almost on the same level as results from Granger Causality. However, for phase shift of $1/8$, $2/8$, $5/8$ and $6/8$, results of imaginary part of coherency are less consistent.

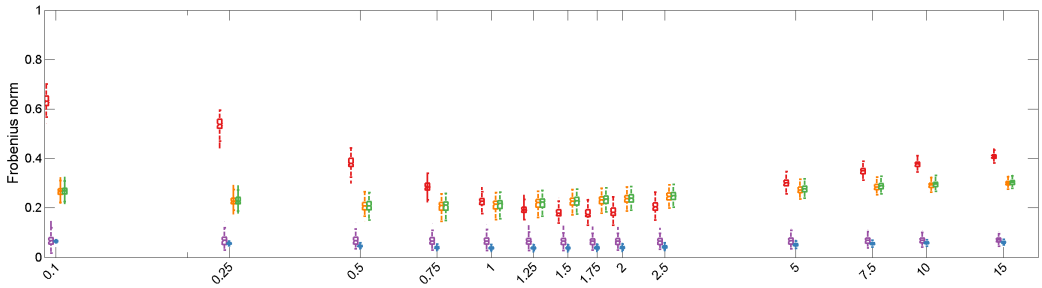

(e) Phase difference: $4/8$

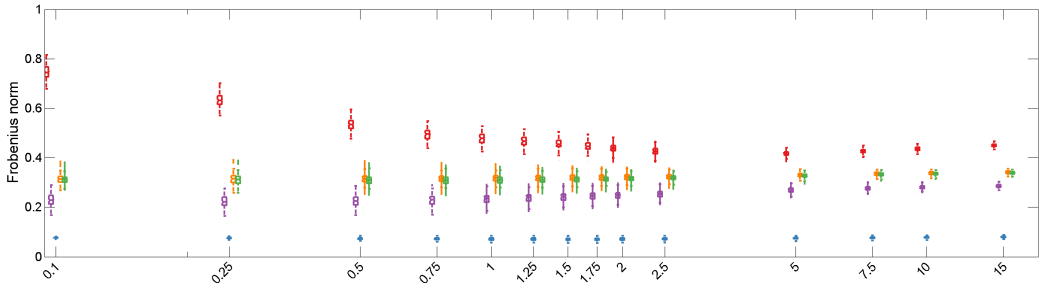

(f) Phase difference: $5/8$

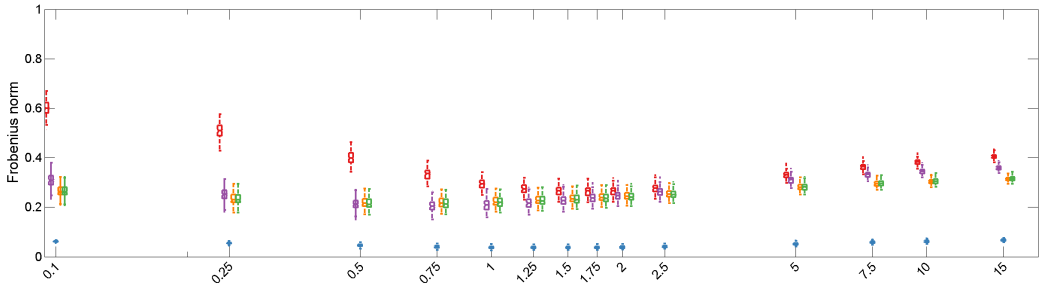

(g) Phase difference: $6/8$

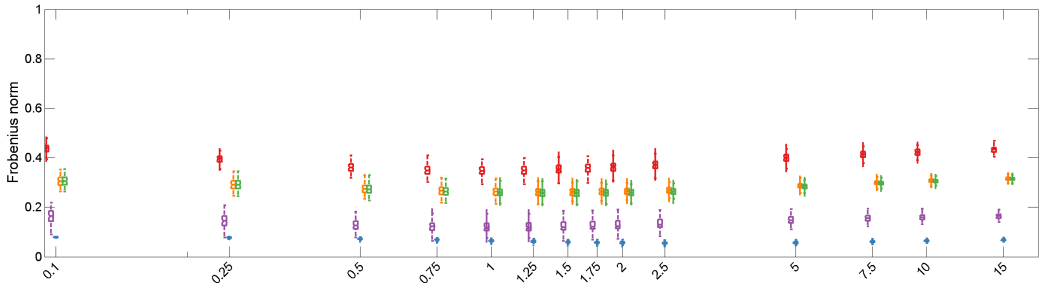

(h) Phase difference: $7/8$

Figure 24: Semi-logarithmic plot of Frobenius norm over SNR for coherence (red), imaginary part of coherency (purple), DTF (orange), PDC (green) and Granger causality (blue) at phase differences ranging from $4/8$ to $7/8$ (cont.).

As shown in the simulation focussing on SNR (section 4.2), coherence is more impaired by SNR than other connectivity estimators. There is a non-linear increase of accuracy for coherence for low SNR levels (0.1 to 2). However, with better data quality, no further significant improvements in accuracy can be achieved above an SNR of 2.
Corresponding results of AUC over SNR for multiple phase differences are shown in figure 25.

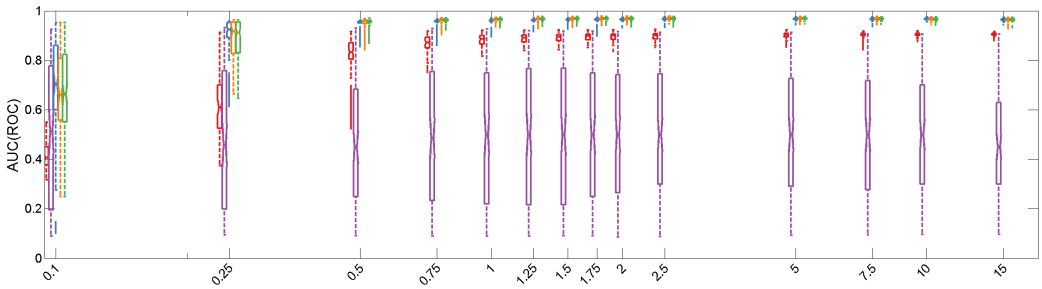

(a) Phase difference: $0/8$

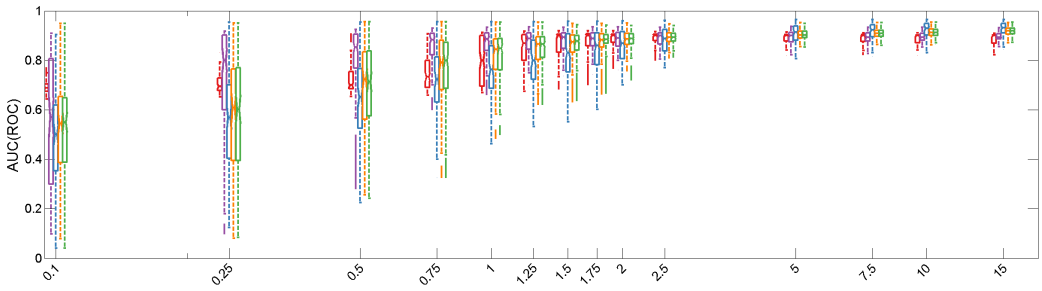

(b) Phase difference: $1/8$

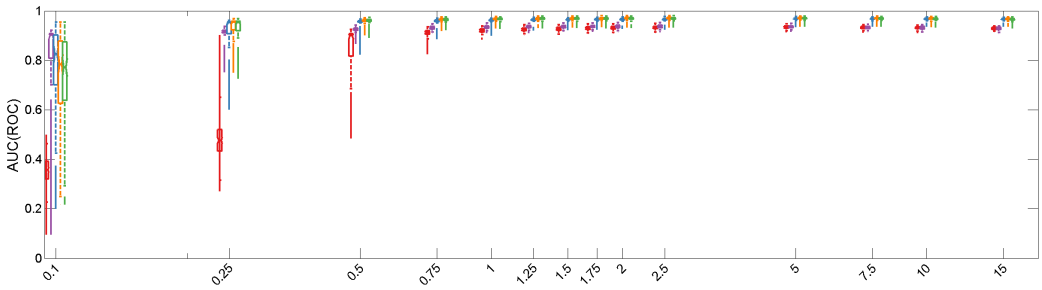

(c) Phase difference: $2/8$

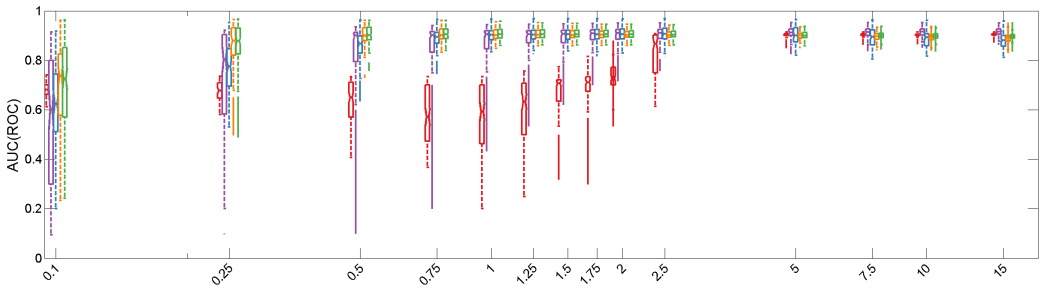

(d) Phase difference: $3/8$

Figure 25: Semi-logarithmic plot of area under ROC curve over SNR for coherence (red), imaginary part of coherency (purple), DTF (orange), PDC (green) and Granger causality (blue) at phase differences ranging from $0/8$ to $3/8$.

Compared to the results of Frobenius norm, AUC boxplots show a significantly higher proportion of variance and inaccuracy. Especially at low SNR levels of 0.1 to 2, it is not possible to give reliable statements on the relative performance of connectivity estimators. From an SNR of 2, results are converging at a high AUC level and show no significant differences between methods over the remaining SNR spectrum. Particularly striking are the AUC boxplots of coherence for the phase differences $5/8$ (figure 25f) and $7/8$ (figure

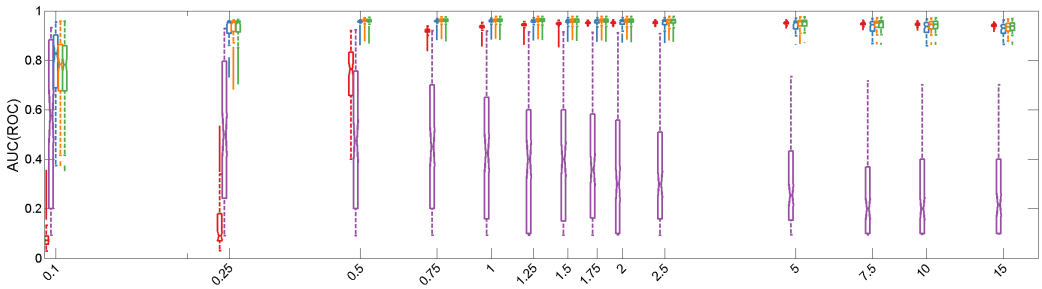

(e) Phase difference: $4/8$

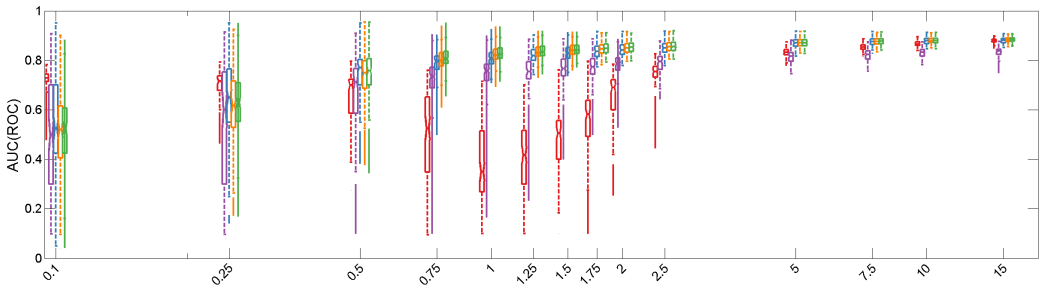

(f) Phase difference: $5/8$

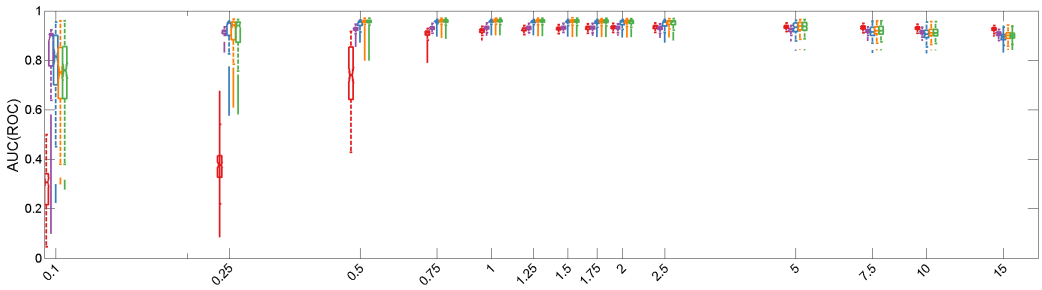

(g) Phase difference: $6/8$

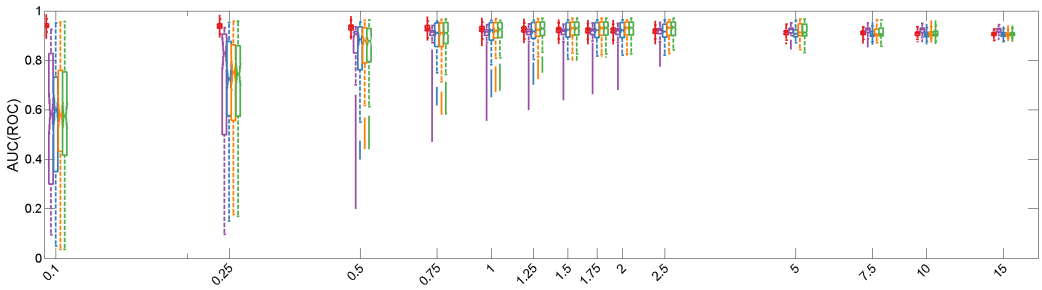

(h) Phase difference: $7/8$

Figure 25: Semi-logarithmic plot of area under ROC curve over SNR for coherence (red), imaginary part of coherency (purple), DTF (orange), PDC (green) and Granger causality (blue) at phase differences ranging from $4/8$ to $7/8$ (cont.).

25h). They expose considerably different results for an SNR range of 0.5 to 2.5 that are not apparent in the results of DTF, PDC and Granger causality and also not reproducible in the remaining phase differences. For imaginary part of coherency, results of AUC reveal a particular vulnerability in case of no phase shift (figure 25a) and for a phase shift of half wavelength (π-phase) of the frequency of interest (figure 25e). This behaviour for non-delayed connections or π-phase interactions between sources is a defining characteristic

of imaginary part of coherency (Nolte et al., 2004, Stam and Reijneveld, 2007).

Discussion

The objective of this experiment was to determine whether differing phase-lags in the information flow between connected brain areas influence the quality and reliability of network reconstructions.
Results obtained from this simulation demonstrate that all connectivity estimators, except for coherence and imaginary part of coherency, are insensitive to the duration of phase differences. Data generated for this experiment included a variation of SNR levels. This enabled the analysis of network reconstructions over a broad SNR range and confirmed results according to the simulation examining the effect of SNR (section 4.2). For low SNR values ranging from 0.1 to 2, significant differences between connectivity estimators could be observed, whereas for higher SNR values ranging from 2.5 to 15, all methods provide consistent and reliable network reconstructions for all phase differences.
Results of Frobenius norm and AUC of coherence show a stronger impact of phase differences as outlined in the previous section. However, these deviations are limited to lower SNR values and do not occur for SNR values of 2.5 and higher.
Imaginary part of coherency provides substantially more reliable and accurate results than coherence. However, this estimator was proposed to eliminate volume conduction effects for estimation of connectivity in sensor space (Nolte et al., 2004). Therefore, it is only sensitive to correlations between sources with a non-zero or or non-π-phase time-lag (Stam and Reijneveld, 2007). In this simulation, results of AUC confirmed that imaginary part of coherency is unable to detect correlated sources for phase shifts of $0/8$ and $4/8$.

4.5 Simulation V - Randomized versus Fixed Source Positions

This simulation will focus on the variability of network reconstructions caused by variations in dipole positions. In each single iteration of all previous simulations, a dipole model with fixed positions for activated brain areas was used. This ensured that potential effects of source positions, which could contribute to the outcome of the network analysis, were minimized allowing an unbiased estimation of the respective parameter to be tested. However, in neuroscientific research, the number and locations of active brain areas is strongly dependent on the particular question being addressed and the experiments carried out to answer them.
Therefore, the simulation described in this section will examine the effect of varying source positions on the accuracy and variability of network reconstructions. This also aims to respond to the question on whether it is possible to transfer results and insights obtained from fixed dipole models to completely different source compositions.

Simulation Setup

As with the previous simulations, this experiment will also make use of a source model including four dipoles. However, the positions and orientations of the dipoles will be recomputed and assigned randomly for each single iteration. To avoid and prevent errors in inverse source reconstruction, the following essential conditions need to be fulfilled for every permutation: this simulation will focus on superficial sources, therefore the maximum depth of dipoles, defined by the distance between the cortical surface and the dipole location, will be restricted to 40 mm. Furthermore, a minimum depth of 5 mm is required. For reliable separation of cortical activity during inverse source reconstruction, distinct brain areas need to have a distance of at least 40 mm from each other. Otherwise, source montages might not be able to distinguish activity from neighbouring brain areas and incorrectly estimate the respective source waveforms. Figure 26 shows four different dipole configurations that were calculated during the experiment and fulfil the above-listed criteria.
The number of dipoles used in this simulation was kept constant. Varying the number of active brain regions is part of a subsequent simulation. In addition to the four dipoles modelling brain activity, 20 noise sources carrying white noise signals where distributed in brain space to simulate background activity for multiple SNR levels ranging from 0.1 to 15. Simulated EEG recordings with an electrode layout consisting of 31 sensors (table A9) were generated for multiple data lengths from 2 s up to 200 s. To reconstruct the source waveforms from EEG data sets, inverse source reconstruction based on source montages was applied. It is worth noting that source montages had to be adopted for each iteration

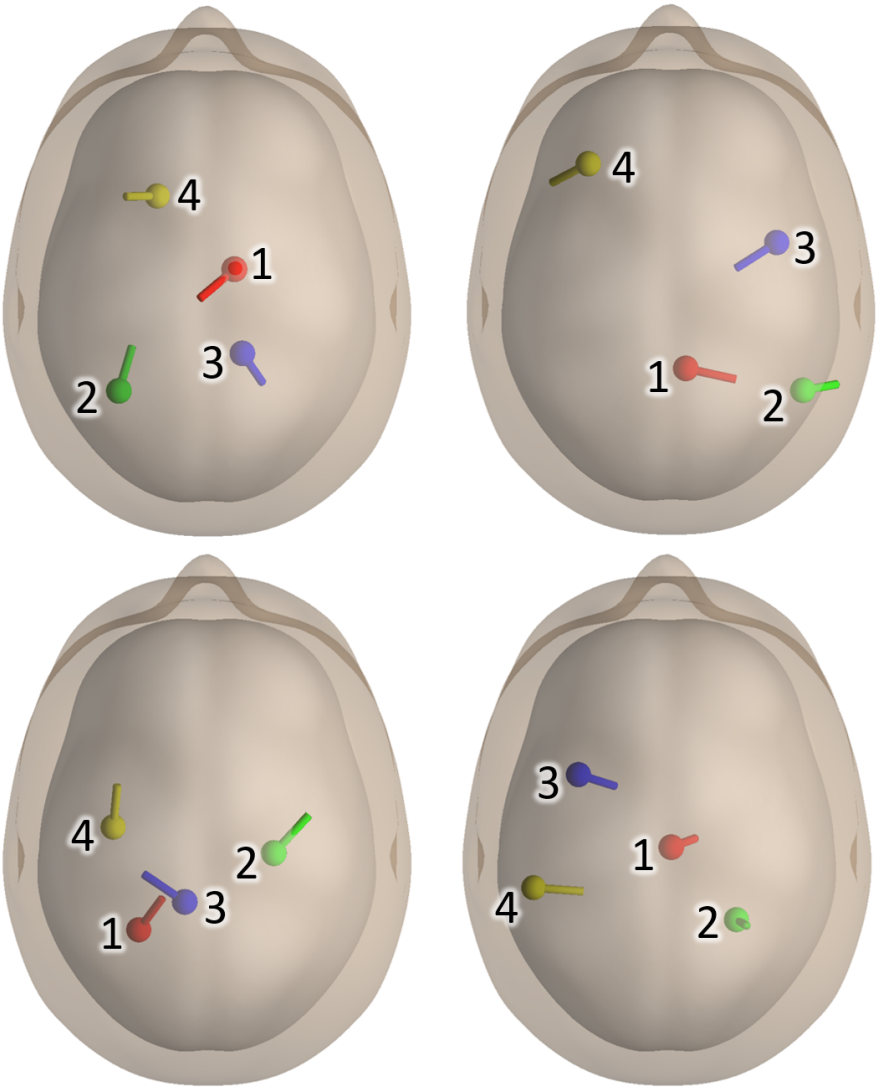

Figure 26: Four randomly selected network configurations from all the dipole models generated during the simulation. Positions and orientations of each dipole were randomly assigned for each iteration. Forward modelling and inverse source reconstruction were carried out based on a realistic standardised FEM head model (BESA Research 6.1).

depending on the randomized dipole configuration to avoid errors for the position and orientation of each source. The analysis of source localization errors is also part of a successive experiment. For each source montage, a regularization factor of 1% was defined. After estimation of temporal cortical activity, connectivity methods were applied to reconstruct simulated dependencies between distinct brain areas. As in the simulations described before, statistical tests were performed to enable quantitative decisions about the effect of randomized source positions on connectivity estimators. Results are presented in the following section using Frobenius norm and AUC comparing the outcome of this simulation to a previous experiment that was based on a similar four dipole model with fixed positions and orientations. Settings for this experiment are outlined in detail in table

4.5.

Table 4.5

Overview of key parameters and settings for simulation V - Randomized versus Fixed Source Positions. The parameter examined in this simulation is indicated in bold type.

Parameter	
Data length	2 s - 200 s
Signal-to-noise ratio	0.1 - 15
Number of network nodes	4
Position of network nodes	**Fixed vs. randomized**
Number of noise nodes	20
Number of electrodes	31
Number of iterations	100
Head model	Realistic standardised FEM head model
Regularization	1%
Localization error	0 mm
Connectivity methods	Coherence, DTF, PDC and GC

Results

This section compares connectivity analysis results of networks with randomized positions to networks with fixed positions. Figure 27 depicts the two different models.

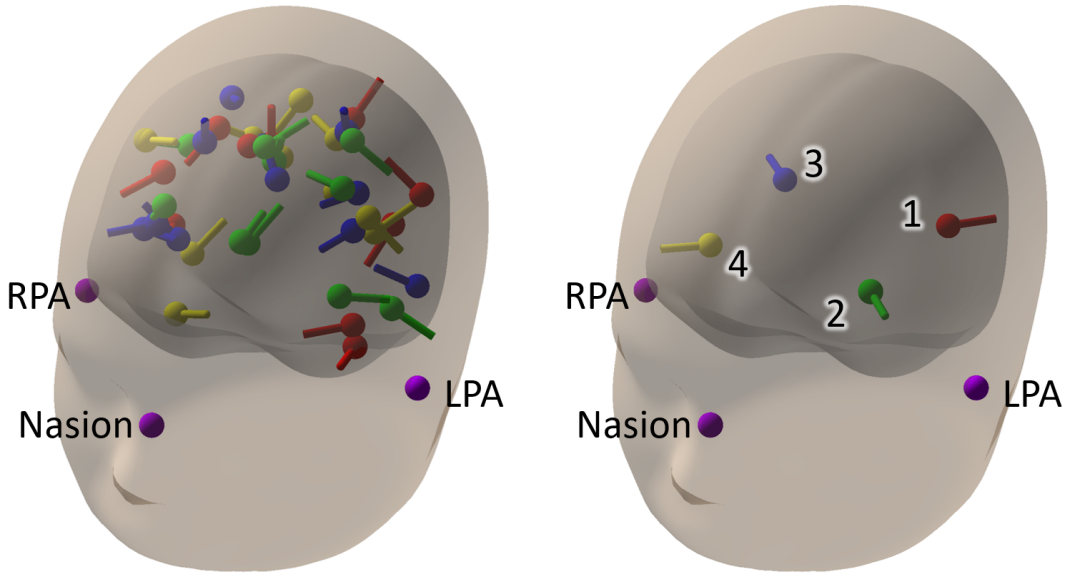

Figure 27: Network configurations for randomized (left) and fixed dipole positions (right). The visualization of randomized position and orientations shows superimposed source locations for a total of 10 out of 100 iterations.

In order to point out the differences between randomized and fixed source position,

connectivity spectra of multiple methods are visualized in figure 28. This figure illustrates the simulated (blue spectra) and reconstructed (red spectra) information flow from source one to source two over the entire frequency spectrum. Graphs shown on the left column are multiple superimposed reconstructions based on the randomized dipole model, whereas graphs on the right column are based on a fixed dipole model.

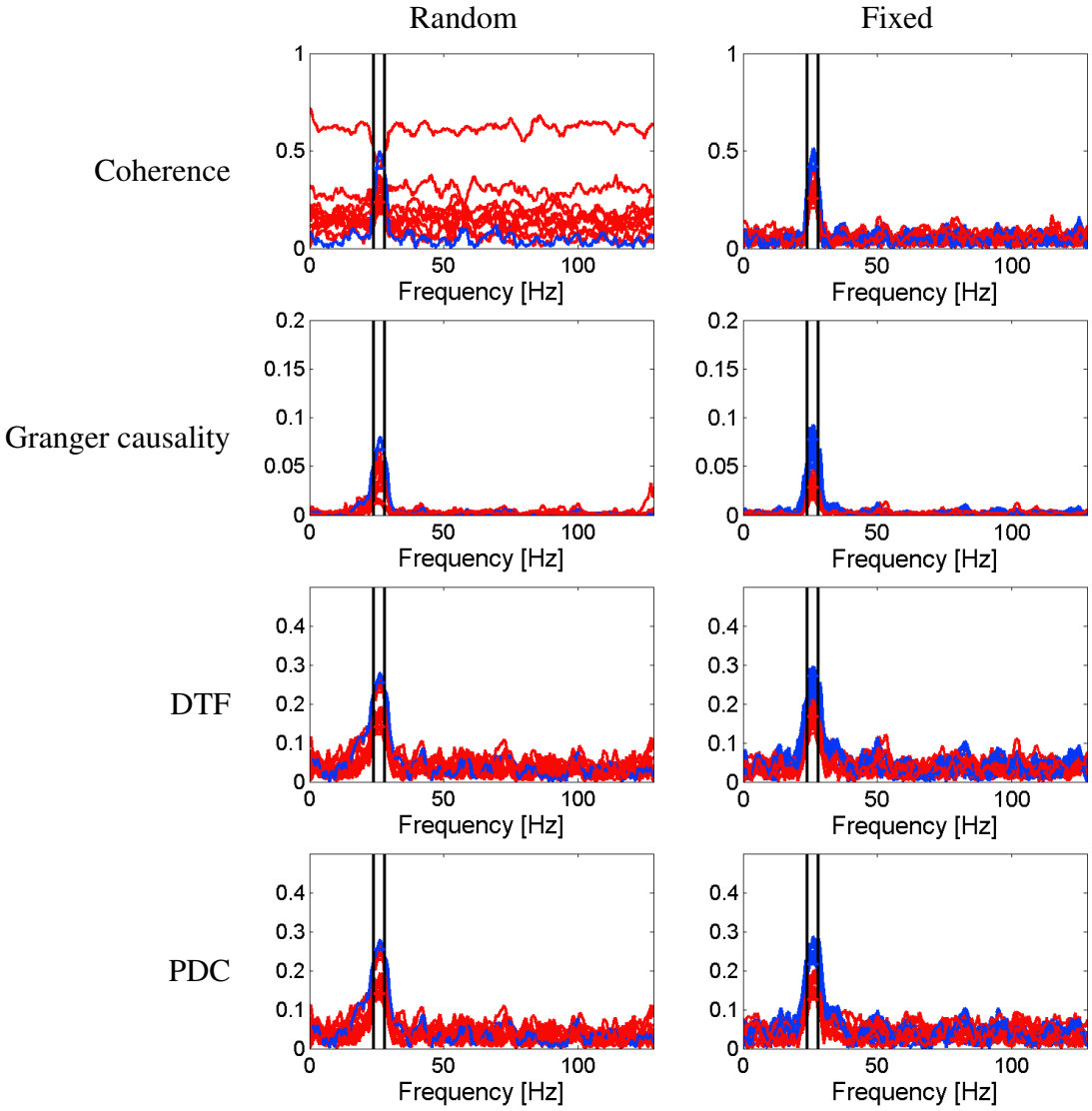

Figure 28: Simulated (blue) and reconstructed (red) connectivity spectra of coherence, DTF, PDC and Granger causality describing the information flow from source one to source two. Network reconstructions used randomized dipole positions (left column) and fixed source positions (right column). Spectra were calculated from data sets of 100 s length and an SNR of 1.

From the figure it is clear that the connectivity spectra of the simulated cortical networks, indicated in blue, are identical independent of the dipole model for all estimators. This result was to be expected, due to the fact that none of the connectivity methods take the positions of active brain areas or the relative distance between correlated regions into account.

Comparing the spectra of each method for both source models, only the network reconstructions using coherence show a significant difference. There is less variation for fixed source positions. Randomized source positions show large variation not only for frequencies outside of the frequency range of interest, but also for the 24 Hz to 28 Hz interval, that contains the modelled information flow from source one to source two. In contrast spectra of Granger causality, DTF and PDC show no significant differences when comparing the two dipole models (random vs. fixed). Moreover, results of these methods based on the randomized model indicate a good overall suppression of noise which enables an easy identification of peaks in the connectivity spectra.
The significant difference between the randomized and fixed dipole model that only occurs for coherence is even more pronounced when applying statistical measures on connectivity reconstructions to calculate Frobenius norm and AUC. Results for several connectivity estimators are displayed in figure 29 showing Frobenius norm and figure 30 illustrating AUC.
Frobenius norm and AUC show no significant differences for DTF, PDC and Granger causality between both dipole models, except for a larger number of outliers in the case of randomized source positions. The variance observed in the connectivity spectra of coherence for random dipole locations lead to larger interquartile ranges in Frobenius and AUC boxplots. This effect is most prominent for an SNR range of 0.1 to 2 and will attenuate for higher SNR values.

Discussion

The goal of this experiment was to demonstrate the effect of random dipole locations and orientations on connectivity estimators. Results showed that the quality of network reconstructions for randomized dipole positions is equivalent to results obtained for fixed positions from previous simulations.
Results from coherence represent an exception to this rule. It could be shown that connectivity spectra, as well as statistical measures based on coherence contain a significantly higher variance for randomized source locations. Apart from this, the quality of network reconstructions will improve with larger SNR values for all connectivity estimators. This is consistent with what has been found in preceding simulations which were based on dipole models with fixed positions and orientations.
It must be pointed out that the source montages (Scherg et al., 2002) used for inverse source reconstruction were a decisive factor for a correct and comprehensive reconstruction of cortical networks. This approach allowed to correctly separate activity from distinct cortical areas even in cases where neighbouring dipoles were located relatively close to each other. One of the requirements predefined by the simulation setup was to provide a minimum distance of at least 40 mm between active cortical areas. Therefore, reconstructions of the

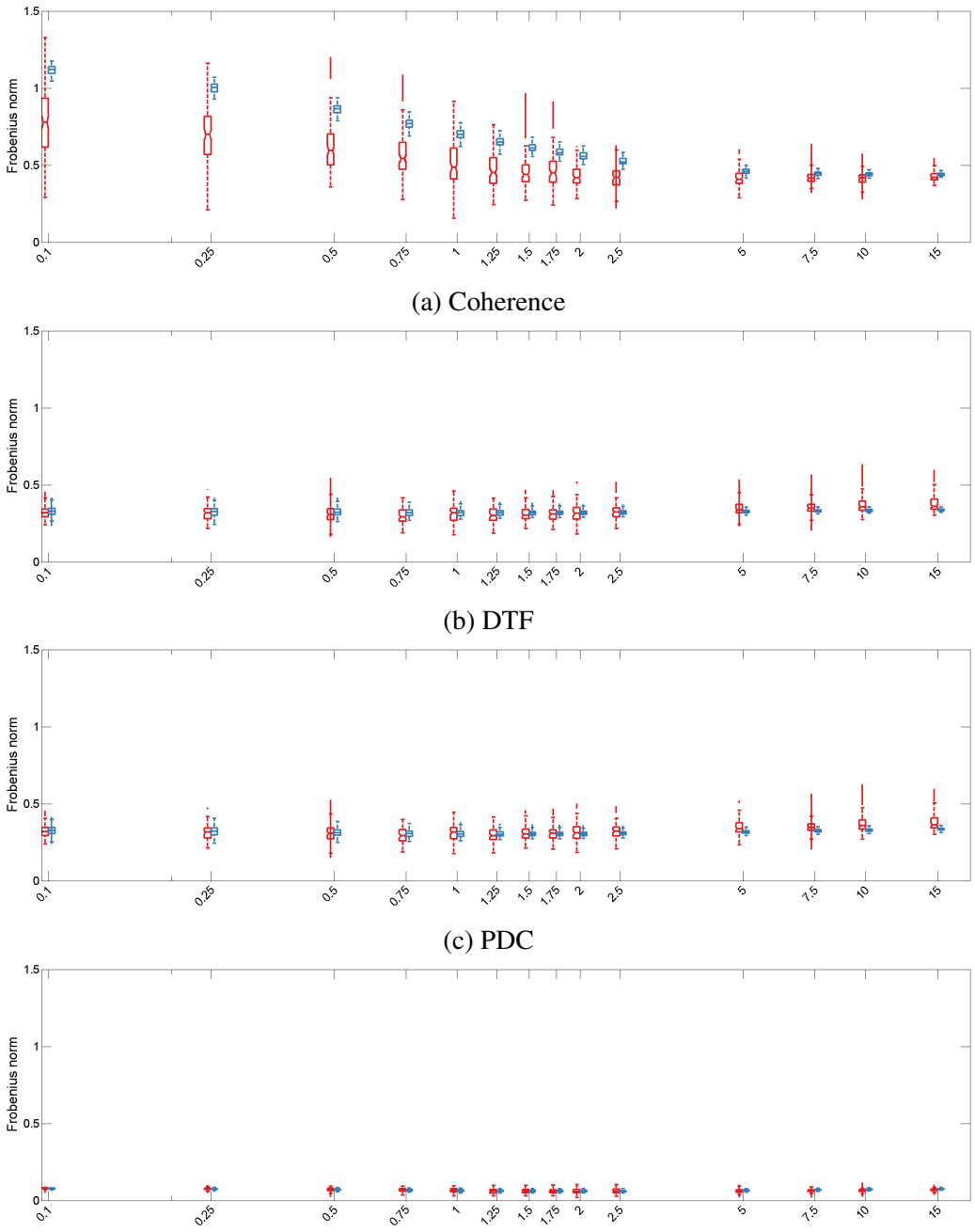

(a) Coherence

(b) DTF

(c) PDC

(d) Granger causality

Figure 29: Semi-logarithmic plot of Frobenius norm over SNR comparing results of random source positions (red) versus fixed souce positions (blue) for coherence, DTF, PDC and Granger causality.

source waveforms provided sufficient accuracy to achieve reliable and consistent results during connectivity analysis.

The main conclusion that can be drawn is that dependencies of specific factors on the quality of network reconstructions obtained from dipole models with a fixed dipole model can be applied to other dipole positions and locations. This finding is however based upon the premise that an appropriate inverse source reconstruction method is applied to allow a

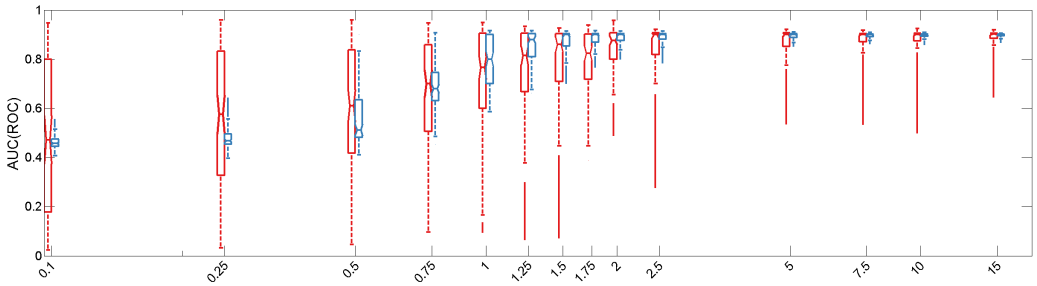

(a) Coherence

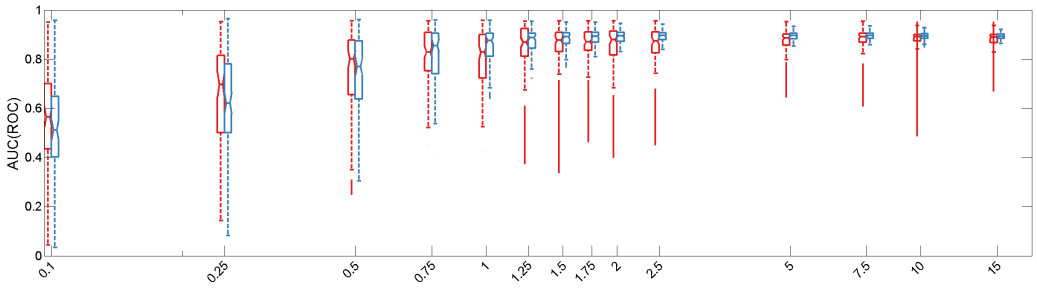

(b) DTF

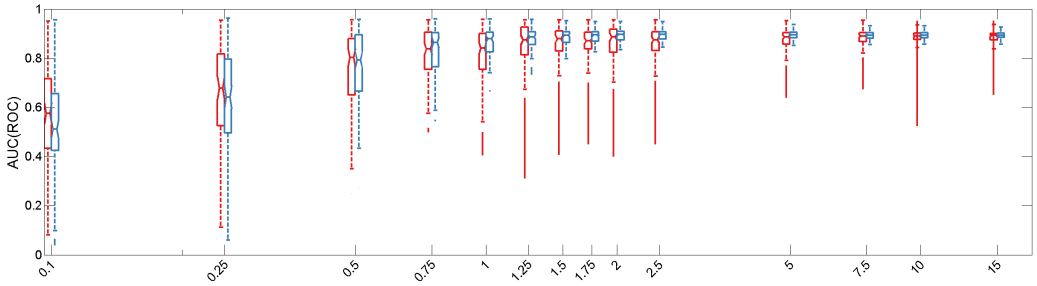

(c) PDC

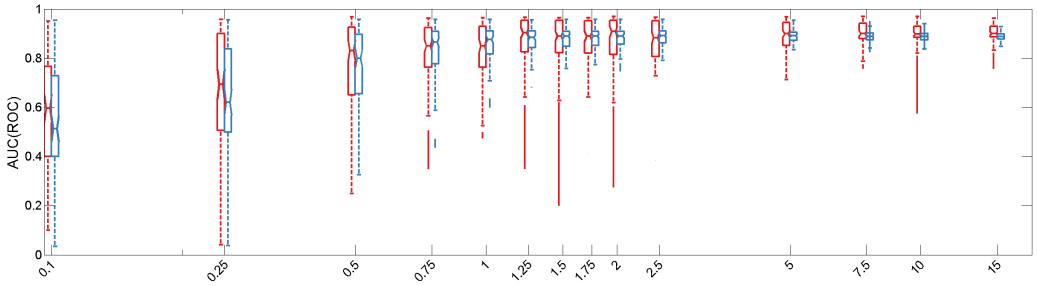

(d) Granger causality

Figure 30: Semi-logarithmic plot of area under ROC curve over SNR comparing results of random source positions (red) versus fixed souce positions (blue) for coherence, DTF, PDC and Granger causality.

correct and unmixed estimation of source waveforms for active brain regions.

4.6 Simulation VI - Regularization

Regularization is applied to solve inverse problems (e.g. inverse source reconstruction) to solve ill-posed problems or to prevent overfitting. Within the simulation framework, it is used in brain source montages (Scherg et al., 2002; Scherg et al., 2004) to estimate cortical activity from simulated electrophysiological data. Equation 2.5 describes the calculation of the inverse leadfield matrix using Tikhonov regularization involving the noise regularization parameter λ. This approach enables the separation of cortical activity and the suppression of cortical background noise. However, the level of regularization to achieve best results in inverse source reconstruction for the underlying data set may not be directly evident. On the one hand, low regularization provides a good separation of cortical activity from distinct cortical regions, but leads to poor noise level for source waveforms. On the other hand, high regularization enables the suppression of background noise but may not fully separate activity originating from different brain areas.
With regard to connectivity estimators, these parameters are likely to have a significant influence on the quality and reliability of network reconstructions. Therefore, this simulation will investigate the effect of regularization on connectivity methods.

Simulation Setup

To analyse the influence of regularization constant (RC) a cortical network based on four dipoles that were placed in the source space as shown in figure 31 was simulated. Information flow from source 1 to 2 and from source 3 to 4 was modelled by introducing joint band-pass filtered white noise signals for coupled sources. The filtered signals of sources 2 and 4 were shifted by a fraction of 25% of the average cycle length (T) at a frequency range of interest from 24 Hz to 28 Hz. This resulted in a phase delay of 9.6 ms between sources with a simulated uni-directional transmission of information. Moreover, independent white noise signals were added to the time-courses of each node.
A concentric 3-sphere volume conduction model (figure 31) was used to model the measurable EEG potential at 31 electrode positions (table A9). Cortical background noise was simulated by randomly distributing 20 dipoles only carrying white noise signal in source space. EEG potentials were likewise calculated by projecting these time-courses on the scalp based on the same head model and were scaled to obtain the desired SNR levels from 0.1 to 15. During inverse source reconstruction based on source montages, different levels of regularization constants were applied. 14 factors ranging from 0% to 20% (0%, 0.1%, 0.15%, 0.2%, 0.3%, 0.5%, 0.7%, 1%, 1.5%, 2%, 5%, 10%, 15% and 20%) were used in the calculation of the truncated singular value decomposition (TSVD, see equation 2.5). To obtain stable and reproducible results, 100 iterations were carried out per regularization level. For each iteration, a fixed data length of 100 s was simulated. Table 4.6 gives an

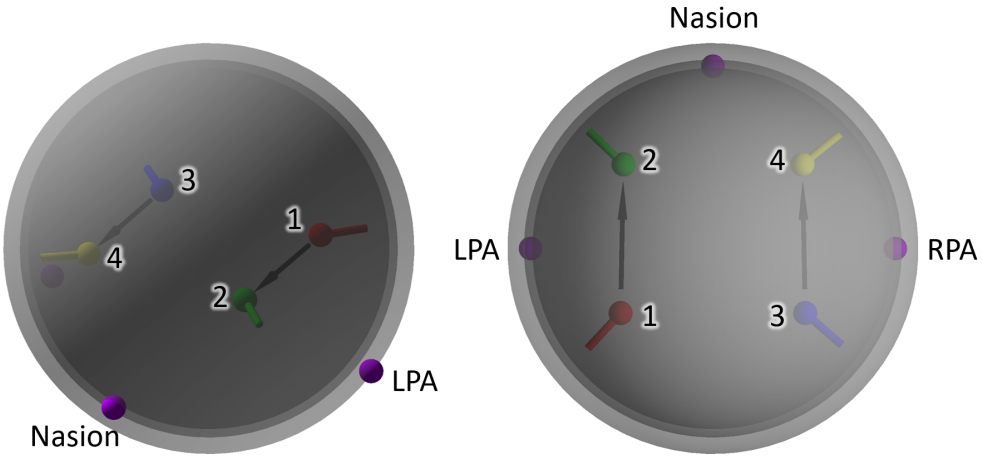

Figure 31: Illustration of 3-shell (brain, skull and scalp compartment) head model and cortical network consisting of four dipoles (table A2). This configuration was used in the current experiment during forward modelling to simulate EEG data and for inverse source reconstruction. Information flow was modelled from source one (red) to source two (green) and from source three (blue) to source four (yellow). Fiducials are indicated as purple spheres.

overview on the configuration for this simulation.

Estimation of the reconstructed cortical network was done using multiple connectivity estimators. A subsequent statistical analysis resting on Frobenius norm and AUC revealed their performance and dependency regarding regularization.

Table 4.6

Overview of key parameters and settings for simulation VI - Regularization. The parameter examined in this simulation is indicated in bold type.

Parameter	
Data length	100 s
Signal-to-noise ratio	0.1 - 15
Number of network nodes	4
Number of noise nodes	20
Number of electrodes	31
Number of iterations	100
Head model	Concentric three-sphere
Regularization	**0% - 20%**
Localization error	0 mm
Connectivity methods	Coherence, DTF, PDC and GC

Results

As emphasized in the last section, the choice of the best regularization value for a specific data set results in a trade-off between noise suppression and sufficient separation of brain activity from different cortical regions. To gain a first insight into the dependency between connectivity estimations and regularization levels, figure 32 shows connectivity spectra for several methods and regularization factors from 0% to 10%. Each graph visualizes superimposed the calculated information flow from source one to source two for 10 out of 100 iterations.

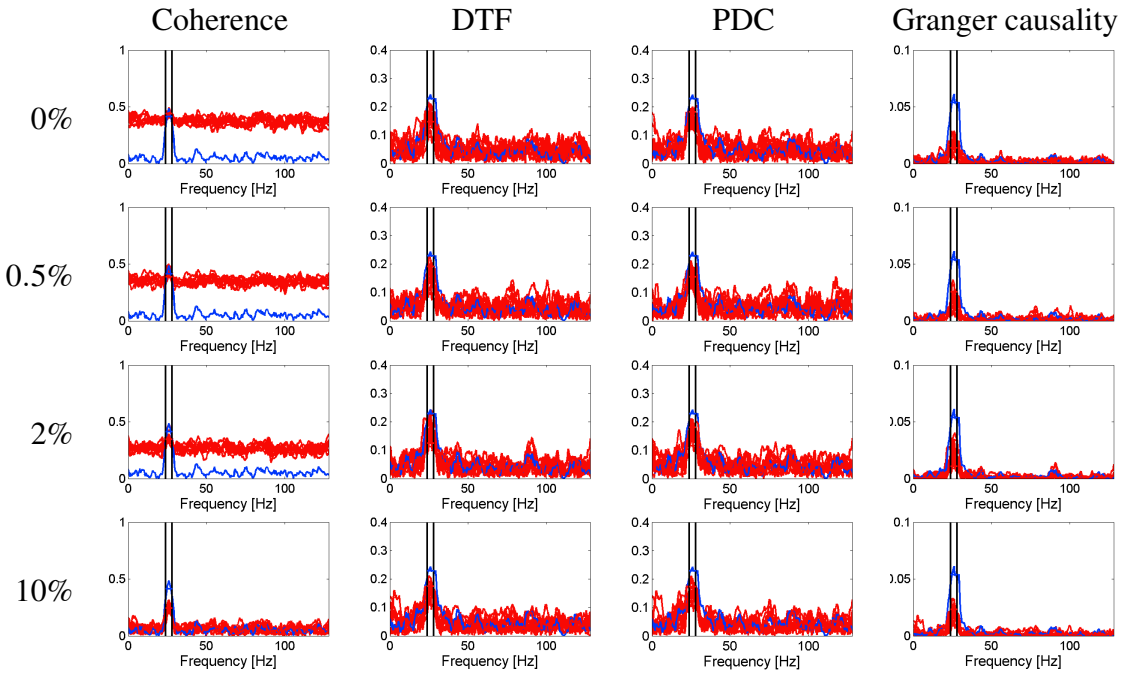

Figure 32: Superimposed connectivity spectra of 10 out of 100 iterations showing simulated (blue) and reconstructed (red) information flow from source one to source two for coherence, DTF, PDC and Granger causality. Each row represents a different level of regularization ranging from 0% to 10%. Connectivity estimation of visualized data was performed on data sets with a length of 100 s and SNR of 1.

From the connectivity spectra of coherence, it becomes clear that an increase in regularization will decrease correlation outside the frequency range of interest. Thus, simulated correlation in the range of 24 Hz to 28 Hz can be detected more easily with high RC values, since connectivity peaks stand out over noise spectrum more prominently. The variation of superimposed spectra remains unchanged even for high regularization.
No significant differences can be observed in the connectivity spectra of DTF, PDC and Granger causality. In contrast to coherence, these three methods provide good noise suppression beyond the frequency range of interest, regardless of the chosen regularization factor. The finding that methods like DTF, PDC and Granger causality are more resistant to noise that coherence has already been depicted in preceding simulations. For Granger

causality, coupled sources are therefore easy to identify due to correlated frequencies having approximately 8 times the value of non-correlated frequencies (outside frequency band of interest). Interestingly, Granger causality also shows that the average connectivity between 24 Hz to 28 Hz is slightly higher for larger RC values. The effect is particularly noticeable when comparing the spectra for 2% and 10% regularization and might be due to the source waveforms being less correctly separated when using high regularization values during inverse source reconstruction.

To test this hypothesis, results of statistical analysis need to be evaluated. Figure 33 shows Frobenius norm boxplots of coherence (red), DTF (orange), PDC (green) and Granger causality (blue) over regularization values from 0.1 to 20% plotted on a logarithmic scale for three SNR values of 0.1 (top), 1 (middle) and 10 (bottom).

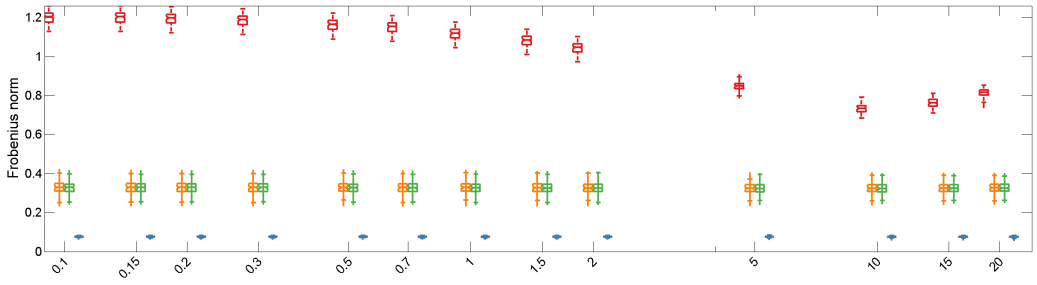

(a) SNR: 0.1

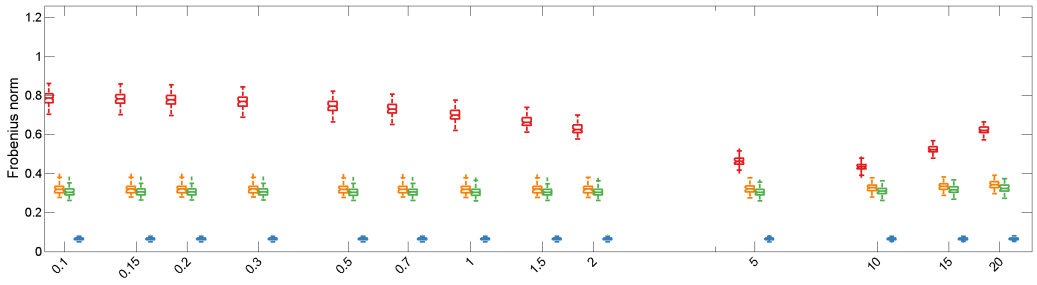

(b) SNR: 1

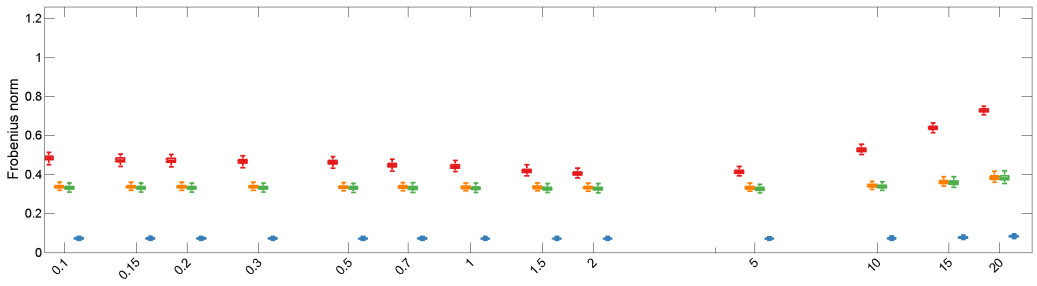

(c) SNR: 10

Figure 33: Semi-logarithmic plot of Frobenius norm over regularization constant [%] for coherence (red), DTF (orange), PDC (green) and Granger causality (blue).

Results indicate that connectivity methods are affected differently to changes of regularization. Particularly for a low SNR value of 0.1, the graphs display a distinct

difference in the quality of network reconstructions when comparing DTF, PDC and Granger causality to the results of coherence. Granger causality provides the best results over all regularization factors in terms of accuracy and stability, followed by DTF and PDC. Coherence shows an improvement in reconstruction for increasing regularization up to a certain limit. Further increase leads to a decline in network reconstruction. This value of optimal reconstruction is dependent on SNR, with higher SNR values requiring lower regularization. For data sets with an SNR of 0.1, a regularization factor of approximately 10% provided best results, whereas for data sets with a higher SNR of 10, significantly less regularization of about 2% to 5% was required to achieve an optimal outcome. A slight decrease in accuracy of network reconstruction could also be observed for DTF, PDC and Granger causality, but only for data sets with high SNR (10) in combination with very high regularization factors ($\geq 15\%$).

Statistical results of area under ROC curve (AUC) for this experiment are illustrated in figure 34. Corresponding to Frobenius norm (figure 33), graphs show a semi-logarithmic plot of AUC over regularization for three SNR levels with a colour-coded classification for the corresponding connectivity estimators.

The dependency between regularization and SNR and their effect on connectivity methods is more difficult to identify for AUC compared to the straightforward and efficient results of Frobenius norm. Since AUC is based on a binary classification test to summarize a connectivity methods ability to correctly identify links between distinct areas, it is less sensitive to relative changes of correlation than Frobenius norm.

Nevertheless, AUC boxplots also indicate a deterioration of network reconstructions for coherence with high regularization. Below this threshold, no significant improvement in the accuracy and reliability of connectivity estimations can be determined. For data sets with higher SNR, all methods provide more precise and stable results.

AUC boxplots of coherence reveal inaccuracies for higher regularization values ($\geq 10\%$) depending on SNR. This inaccuracy of AUC calculations is due to the methodological limitations of the method rather than a strongly declining performance of network reconstruction. The reason for this is the predominant share of negatives to positives and the choice of the threshold for the computation of TPR and FPR. A modification of the AUC calculation proposed by Clark and Webster-Clark (Clark and Webster-Clark, 2008) that uses a semi-logarithmic scaling of the receiver-operator characteristic curve could be implemented to eliminate these inaccuracies.

Discussion

This simulation was designed to reveal the effect of regularization on connectivity methods. Moreover, a side issue that should be outlined was the dependency between regularization and SNR and their interaction during network reconstructions.

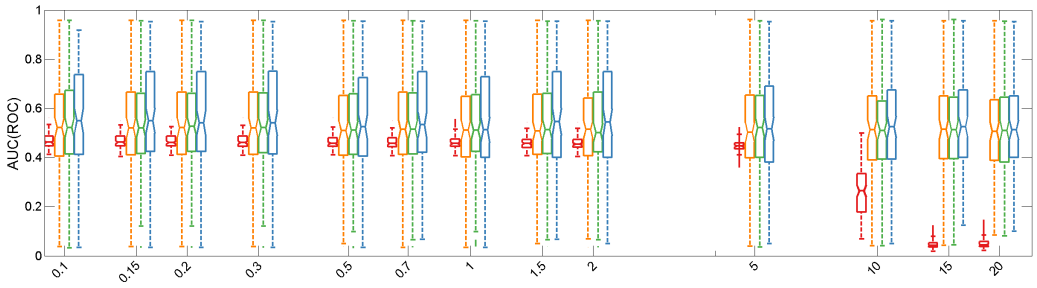

(a) SNR: 0.1

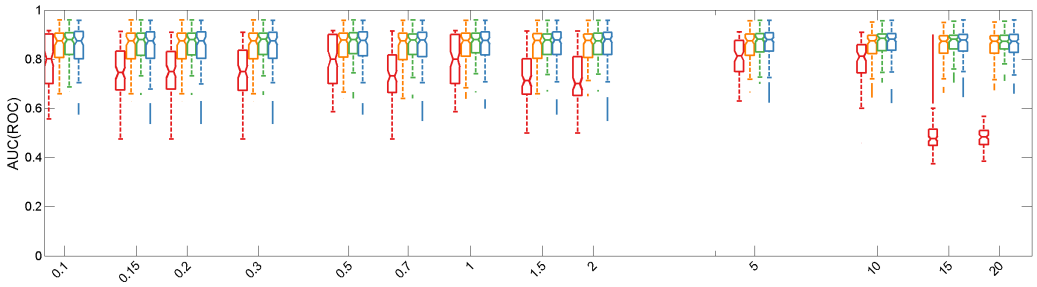

(b) SNR: 1

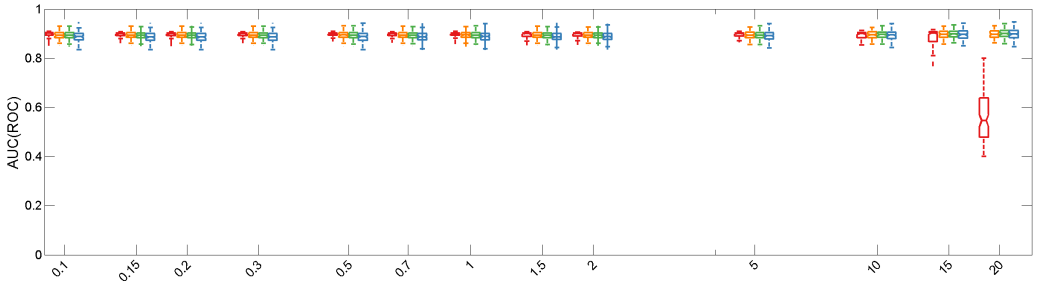

(c) SNR: 10

Figure 34: Semi-logarithmic plot of AUC over regularization constant [%] for coherence (red), DTF (orange), PDC (green) and Granger causality (blue).

In order to demonstrate this, data sets with different SNR values from 0.1 to 15 were analysed using source montages that incorporated regularization factors ranging from 0% up to 20%. On the basis of this model, it could be shown that the degree of regularization chosen during inverse source reconstruction is crucial for network reconstructions and depends on data quality. It emerged that connectivity methods are affected differently by changes in regularization. A particularly significant impact was shown for coherence, whereas DTF, PDC and Granger causality showed almost no influence of regularization on network reconstructions. Coherence provided an enhancement in accuracy for increasing regularization up to a specific threshold depending on SNR. Further increase led to a decline in network reconstruction. Other methods did not show any alteration when increasing regularization. Only in cases with very high SNR (10) and excessive regularization ($\geq 15\%$) DTF, PDC and Granger causality also indicated a slight decrease in accuracy.

4.7 Simulation VII - Source Localization Error

In the analysis and evaluation of EEG and MEG recordings, much importance and value is generally attached to inverse source localization and a most accurate prediction of the position of active brain regions. However, it is not known to which extent source localization errors influence the quality of network analysis. Therefore, this simulation was aimed to analyse effects of poor and insufficient source reconstruction.
Preceding experiments used identical dipole positions for forward modelling and during inverse source reconstruction applying the respective source montage. This procedure was necessary since the main focus was put on parameters like data length, signal-to-noise ratio or phase difference. For this reason, errors in source localization had to be minimized to obtain an unbiased view on the dependency of connectivity estimators on the particular parameter to be analysed in the respective simulation.
This section is concerned exclusively with the influence of systematic errors in the localization of active cortical areas to answer the question to which extent correctness and accuracy of network reconstructions are affected by deviations in source positions. Moreover, simulated electrophysiological data sets will be analysed using different regularisation constants during inverse source localization. This serves to investigate whether errors in the estimation of dipole positions can be compensated by lower or higher levels or regularization.

Simulation Setup

The simulation is based on a four dipole model, with positions kept fixed during forward modelling (see table 4.7 for a detailed list of parameters). Generated data sets for each of the 100 iterations consisted of a data length of 100 seconds and a sampling rate of 256 samples per second. As described in previous simulations, EEG potentials of 20 randomly positioned noise sources carrying white noise signals were calculated by projecting the time-courses onto the scalp using a concentric 3-sphere volume conduction model. The resulting noise topographies were scaled and added to the network topographies to obtain SNR levels ranging from 0.1 to 15 in the frequency range of interest (24 Hz to 28 Hz).
To add systematic, predefined errors during source reconstruction, source montages (Scherg et al., 2002) no longer maintained identical positions as used for forward modelling. Coordinates of each source were altered by a randomly generated error term to create a systematic deviation between the simulated dipole model and the source montage with a maximum variance of 25 mm per node. Figure 35 illustrates different error levels ranging from 3 mm to 25 mm. It should be noted that the deviations from the original coordinates correspond exactly to the indicated error term. Therefore, the positions of dipoles that were used for inverse source localization do not fall within the outlined error sphere but precisely

on the sphere's edge.

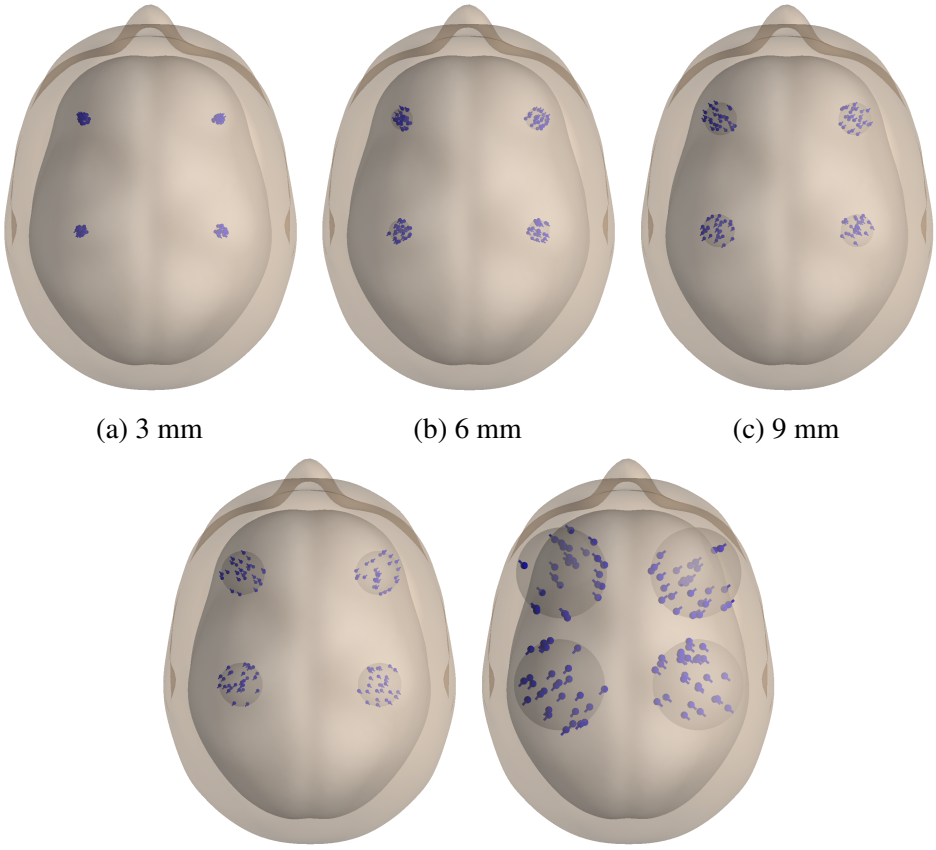

(a) 3 mm (b) 6 mm (c) 9 mm

(d) 12 mm (e) 25 mm

Figure 35: Representation of source models with four dipoles used for generating source montages with error terms ranging from 3 mm to 25 mm. For each simulation, the respective deviation was added to the positions of each source as described in table A2. Each graph shows superimposed source positions for 30 of the 100 iterations carried out in this simulation. The sphere for the respective localization error of each dipole is displayed slightly transparent.

Furthermore, inverse source reconstruction was performed applying source montages including localization errors and different regularization factors ranging from 0% to 20%. Another critical parameter of inverse source analysis that needs to be considered is the orientation of active brain areas. Ideally, a perfect estimation of cortical activity matches the orientation of the simulated dipole activity. A deviation between the orientation of the simulated and the reconstructed dipole will lead to a modification of the source waveform and therefore influence subsequent network reconstructions. As shown in figure 35, the orientations of dipoles used for source reconstruction remained unchanged to focus solely on the effect of errors in dipole positions.

Multiple connectivity estimators were applied on the estimated temporal cortical activity to reconstruct dependencies between distinct brain areas. On this basis, statistical tests were carried out to measure the effect of source localization errors on network reconstructions.

Table 4.7

Overview of key parameters and settings for simulation VII - Source Localization Error. The parameter examined in this simulation is indicated in bold type.

Parameter	
Data length	100 s
Signal-to-noise ratio	0.1 - 15
Number of network nodes	4
Number of noise nodes	20
Number of electrodes	31
Number of iterations	100
Head model	Concentric three-sphere
Regularization	0% - 20%
Localization error	**3 mm, 6 mm, 9 mm, 12 mm, 25 mm**
Connectivity methods	Coherence, DTF, PDC and GC

Results

Results presented in this section depict the performance of connectivity estimators with regard to particular source localization errors. As a first indicator, connectivity spectra indicating the information flow from source one to source two are illustrated in figure 36. From the connectivity spectra, it becomes apparent that reconstructions using Granger causality and DTF are not significantly influenced by an increase of source localization error. Peaks of high correlation, particularly in the frequency range of interest (24 Hz to 28 Hz), are quite prominent. Coherence, on the other hand, shows a noticeable increase in variance over the entire frequency range with higher error values. As already demonstrated in earlier simulations, peaks of large coherence are hard to detect due to high noise level beyond the frequency range of interest. Nevertheless, using data sets with higher SNR, noise can be diminished allowing easier identification of correlation with more prominent peaks.
Results of the statistical analysis of connectivity spectra for data sets with a SNR of 1 and a data length of 100 s are shown in figure 37, illustrating Frobenius norm, and in figure 38 displaying AUC.
Both figures confirm the assumption that was established when analysing and evaluating connectivity spectra (figure 36). Thus, only results of coherence provide significantly higher variance for larger source localization deviations, whereas results of DTF, PDC and Granger causality show no effect at all. Most importantly, statistical evaluation of all connectivity estimators found no evidence that the average accuracy level of network reconstructions was significantly reduced for any source localization errors. Furthermore, with regards to the result of different connectivity methods, it can be stated that Granger causality provides the most accurate and reliable network reconstructions.

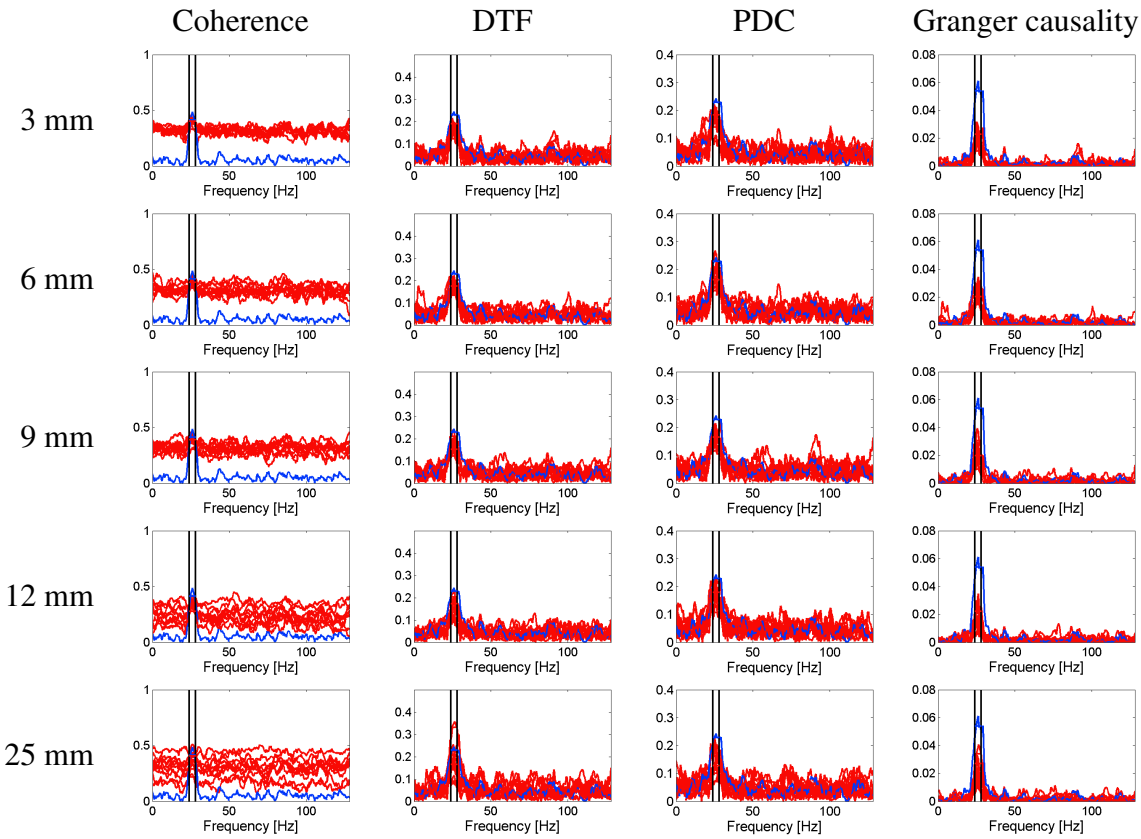

Figure 36: Connectivity spectra showing simulated (blue) and reconstructed (red) information flow from source one to source two for coherence, DTF, PDC and Granger causality. Each row represents a different level for the source localization error (3 mm to 25 mm) based on a regularization constant of 1%. Data sets with a length of 100 s and SNR of 1 were evaluated for this visualization.

Building on the results from the current simulation, it was also examined if localization errors made during inverse source reconstruction may be compensated by adjusting the regularization constant. Network reconstructions using coherence will be applied to demonstrate this effect, since it is most prone to source localization effects compared to other methods. Figure 39 illustrates the outcome of this evaluation.

It shows Frobenius norm for different, colour-coded source localization errors over regularization constant in logarithmic scale. As shown in the simulation focussed on regularization before (chapter 4.6), it could also be demonstrated in this example that network reconstructions can be significantly improved with increasing regularization. This applies to the stability of connectivity estimations, indicated by more narrow interquartile ranges, as well as to the overall accuracy, due to lower median values. However, this is only valid to a certain degree of regularization. In this example, the optimal regularization value for a data set with SNR 0.1 (figure 39a) is at approximately 15%. For data sets with better SNR, less regularization is required to obtain optimal results for network reconstructions. For a SNR of 1, best estimations were provided by a regularization factor of 10% and for data

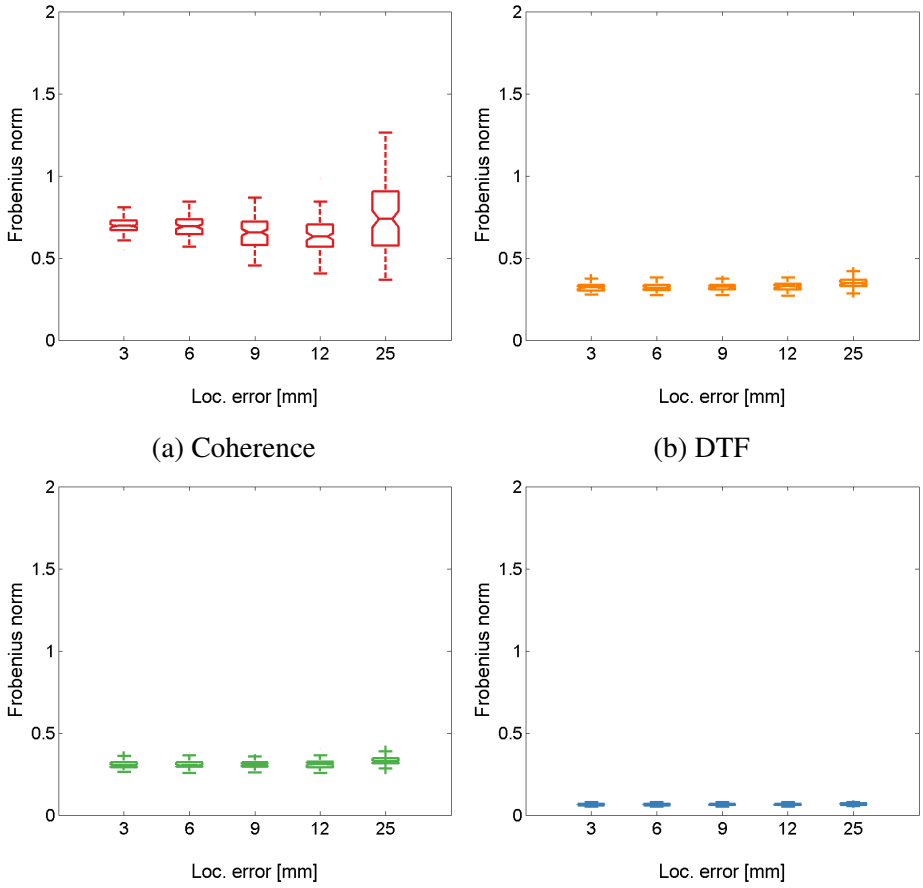

(a) Coherence (b) DTF

(c) PDC (d) Granger causality

Figure 37: Frobenius norm over localization errors for coherence (red), DTF (orange), PDC (green) and Granger causality (blue) of data sets with a length of 100 s and SNR of 1. Results used for this visualization were based on a source montage with a regularization constant of 1%.

sets with a SNR of 10 a regularization of 2% to 5% provided strongest results. Increasing this value even further will lead to a deterioration of results. The optimal regularization value depends primarily on the SNR of the respective data set. This corresponds to the findings from the previous simulation that demonstrated the dependence between regularization and SNR and the influence of both parameters on network reconstructions.

Discussion

This simulation considered the effect of source localization errors on the performance of connectivity methods. It could be demonstrated that there is no significant decline in accuracy and precision of network reconstructions with an increase of localization error for all estimators. However, larger localization errors lead to an increase of variance and less reliability. Coherence was particularly affected by erroneous localization of active brain regions, whereas methods like DTF, PDC and Granger causality showed no significantly

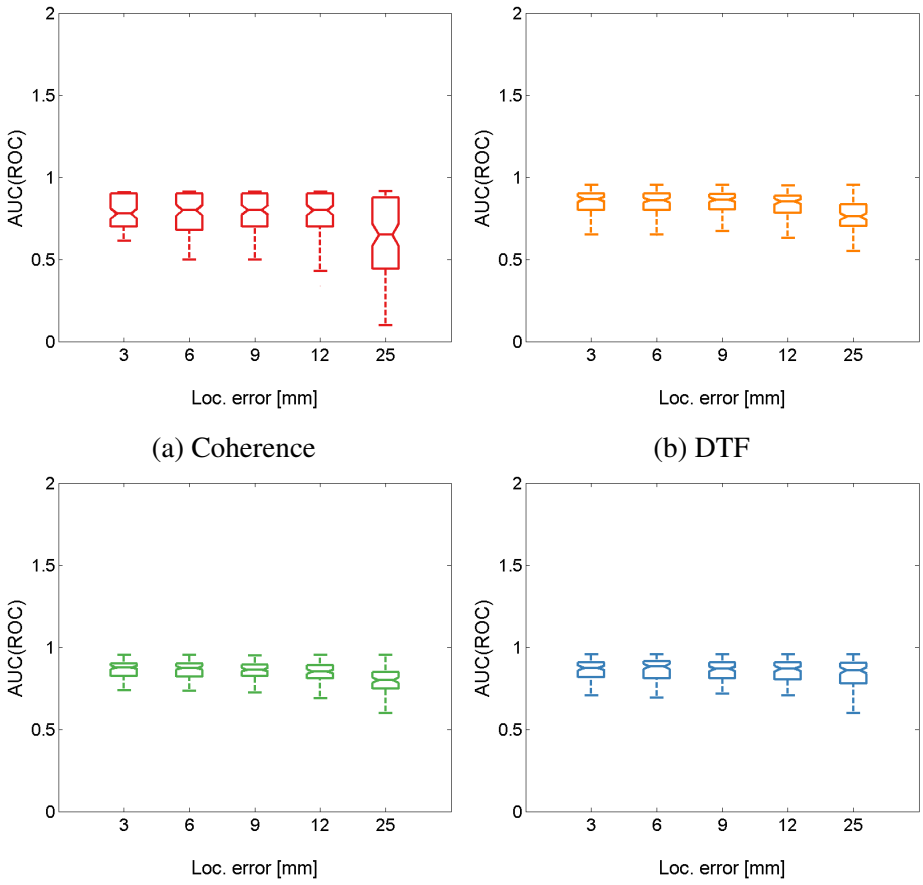

(a) Coherence (b) DTF

(c) PDC (d) Granger causality

Figure 38: AUC over localization errors for coherence (red), DTF (orange), PDC (green) and Granger causality (blue) of data sets with a length of 100 s and SNR of 1. Results used for this visualization were based on a source montage with a regularization constant of 1%.

difference for larger errors, with Granger causality outperforming all other methods.

Furthermore, it was examined whether an increase in regularization might lead to an improvement in the accuracy of network estimations. By focusing on coherence, it became apparent that the regularization factor to obtain an optimal network reconstruction depends on the SNR of the underlying data set. This dependency was shown before in a previous simulation analysing the effect of RC, and could also be transferred to this experiment including localization errors.

It is worth noting that a dipole used to model the activity of a particular active brain region is defined by its position, that may be deviating from the actual location, but also by its orientation. The present simulation dealt with errors for the position of a dipole, however, its orientation was not altered. Both parameters are essential for the estimation of the temporal activity pattern of cortical areas. Hence, it would be instructive to carry out another simulation that focuses on the effect of orientation errors on network reconstructions.

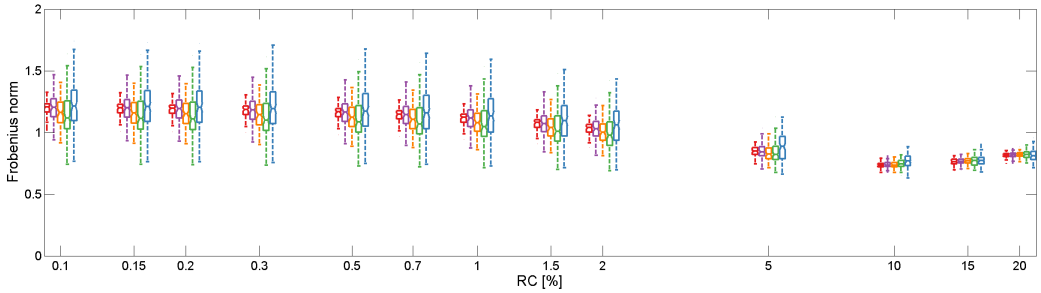

(a) SNR: 0.1

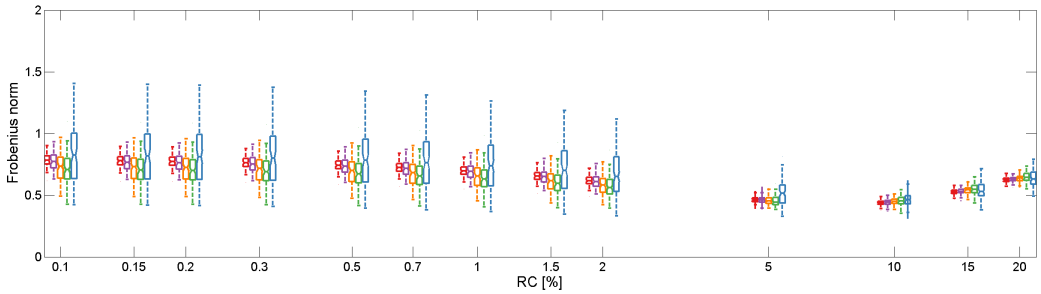

(b) SNR: 1

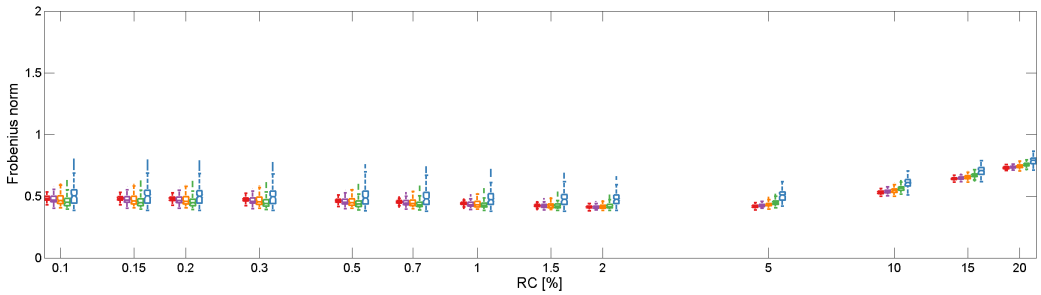

(c) SNR: 10

Figure 39: Semi-logarithmic plot of Frobenius norm over regularization constant [%] for coherence. Source localization errors are colour-coded: 3 mm (red), 6 mm (purple), 9 mm (orange), 12 mm (green), 25 mm (blue). The analysed data set implied a SNR of 0.1 (top), 1 (middle) and 10 (bottom).

4.8 Simulation VIII - Network Size

In this final experiment, the main focus is on the size of complex neural networks, defined by the number of active sources involved in the exchange and transfer of information. Previous simulations were based on a network model consisting of a fixed number of four dipoles. However, the amount of active cortical areas in a neural network may easily exceed this number. This does not only make inverse source reconstruction more difficult, but also complicates the estimation of correlated areas. Therefore, this simulation is designed to determine the effect of network size by analysing networks with different number of active brain regions.
Another important characteristic of networks is the number of connections between network nodes. A differentiation is made between direct and indirect connections between active sources (see figure 5). Some connectivity estimators take the simultaneous information flow between more than two nodes into account, while other methods may only calculate the correlation between two distinct sources at a time. The simulated number of direct and indirect connections amongst nodes defines the complexity of a network. The difficulty of accurate network reconstructions consists of the partial influence of indirect connections and their differentiation from direct information flow between network nodes. For this simulation, it must be ensured that the complexity of networks is kept at a comparable level to allow drawing conclusions regarding the number of active nodes.

Simulation Setup

In order to evaluate the influence of network size on the quality of network reconstruction, networks with sizes from 4 nodes to 10 nodes were simulated and analysed. A detailed description of source positions is part of the appendix of this thesis: 4 nodes: table A2, 6 nodes: table A3, 8 nodes: table A4, 10 nodes: table A5. Figure 40 illustrates the dipole positions and information flow for the different networks. The relative number of connections, defined by the ratio of existing connections divided by the the number of possible connections within a network was kept constant at about 16% to obtain an equal complexity for all networks. Table 4.8 gives an overview on the connection matrices for each network size as well as the number of simulated connections, number of possible connections and the respective ratio. The phase delay for links between network nodes is expressed as a fraction of the average cycle length (T). All connections were simulated to occur within a frequency band of 24 Hz to 28 Hz, resulting in an average cycle length of 26 Hz.
Based on these network configurations, EEG data sets of 100 s at a sampling rate of 256 samples per second and 64 electrodes were created. The complete list of sensors labels and

Table 4.8

Connection matrices for all cortical networks used in this simulation experiment. The matrix coefficients indicate the phase shift between connected nodes as a fraction of the average cycle length (T) at a frequency range of interest from 24 *Hz to* 28 *Hz.*

Nodes	Connection matrix	NC	NPC	Ratio
4	$\begin{bmatrix} 0 & T/4 & 0 & 0 \\ 0 & 0 & 0 & 0 \\ 0 & 0 & 0 & T/4 \\ 0 & 0 & 0 & 0 \end{bmatrix}$	2	12	16.7%
6	$\begin{bmatrix} 0 & T/4 & T/5 & 0 & T/6 & 0 \\ 0 & 0 & 0 & 0 & 0 & 0 \\ 0 & 0 & 0 & T/4 & 0 & T/6 \\ 0 & 0 & 0 & 0 & 0 & 0 \\ 0 & 0 & 0 & 0 & 0 & 0 \\ 0 & 0 & 0 & 0 & 0 & 0 \end{bmatrix}$	5	30	16.7%
8	$\begin{bmatrix} 0 & T/4 & 0 & 0 & T/5 & 0 & T/4 & 0 \\ 0 & 0 & 0 & 0 & 0 & 0 & 0 & 0 \\ 0 & 0 & 0 & T/4 & 0 & T/5 & T/4 & 0 \\ 0 & 0 & 0 & 0 & 0 & 0 & 0 & 0 \\ 0 & 0 & 0 & 0 & 0 & 0 & 0 & 0 \\ 0 & 0 & 0 & 0 & 0 & 0 & 0 & 0 \\ 0 & 0 & 0 & 0 & 0 & 0 & 0 & 0 \\ T/6 & 0 & T/6 & 0 & 0 & 0 & T/4 & 0 \end{bmatrix}$	9	56	16.1%
10	$\begin{bmatrix} 0 & 0 & 0 & 0 & 0 & 0 & 0 & T/5 & 0 & 0 \\ 0 & 0 & 0 & 0 & 0 & 0 & T/5 & 0 & 0 & 0 \\ 0 & 0 & 0 & 0 & 0 & 0 & 0 & T/5 & 0 & 0 \\ 0 & 0 & 0 & 0 & 0 & 0 & T/5 & 0 & 0 & 0 \\ 0 & T/5 & 0 & 0 & 0 & 0 & 0 & 0 & 0 & 0 \\ 0 & 0 & T/5 & T/5 & 0 & 0 & 0 & 0 & 0 & 0 \\ 0 & 0 & 0 & 0 & 0 & 0 & 0 & 0 & 0 & 0 \\ 0 & 0 & 0 & 0 & 0 & 0 & 0 & 0 & 0 & 0 \\ T/5 & T/5 & 0 & 0 & T/6 & 0 & T/4 & 0 & 0 & 0 \\ 0 & 0 & T/5 & T/5 & 0 & T/6 & 0 & T/4 & 0 & 0 \end{bmatrix}$	15	90	16.7%

NC = number of connections, NPC = number of possible connections

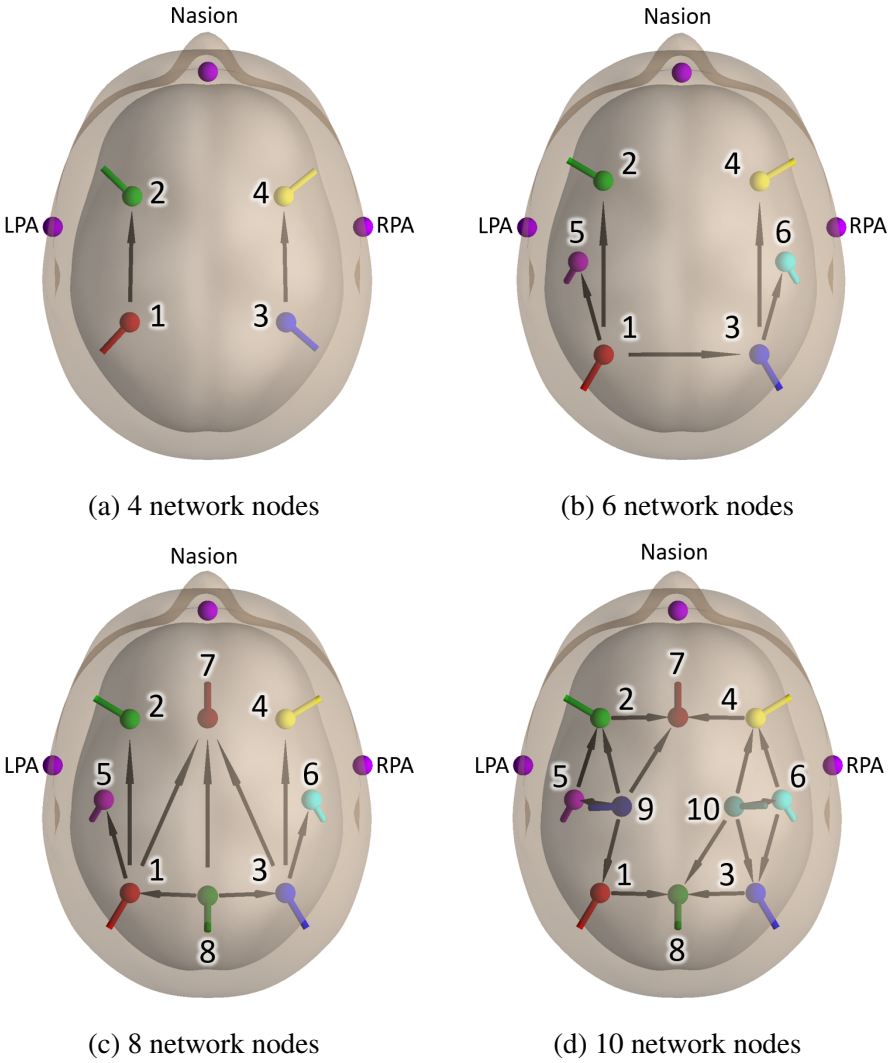

(a) 4 network nodes

(b) 6 network nodes

(c) 8 network nodes

(d) 10 network nodes

Figure 40: Overview of cortical networks implemented in this experiment to analyse the effect of network size on connectivity estimators. Arrows indicate direct connections between the respective network nodes. Fiducials (nasion, left and right pre-auricular points) are indicated as purple spheres.

positions is given in table A10. Forward modelling was performed based on a three-shell concentric spherical volume conduction model. SNR was varied from 0.1 to 15. 100 iterations were carried out for each of these parameter combinations to obtain stable and reliable results.

For inverse source reconstruction, source montages were created with identical locations and orientations for all network nodes and the same three-shell head model as used during forward modelling. Furthermore, a regularization factor of 2% was used to estimate source waveforms for each source.

Subsequently, multiple connectivity methods were applied to reconstruct information flow between network nodes. Accuracy and stability of reconstructions for each estimator were measured by applying Frobenius norm and AUC. An overview on the configuration for this

simulation is shown in table 4.9.

Table 4.9

Overview of key parameters and settings for simulation VIII - Network Size. The parameter examined in this simulation is indicated in bold type.

Parameter	
Data length	100 s
Signal-to-noise ratio	0.1 - 15
Number of network nodes	**4, 6, 8, 10**
Number of noise nodes	20
Number of electrodes	64
Number of iterations	100
Head model	Concentric three-sphere
Regularization	2%
Localization error	0 mm
Connectivity methods	Coherence, DTF, PDC and GC

Results

This section presents the performance of connectivity methods depending on the network size, starting with connectivity spectra of coherence, DTF, PDC and Granger causality illustrated in figure 41 for a six-node network. It shows the superimposed spectra of 10 out of 100 iterations for the respective estimators. Connectivity estimations for all possible links within the entire network are displayed resulting in a visualization of a six by six connectivity matrix. Simulated direct connections of real information flow between two distinct areas are highlighted by an additional frame around the respective spectrum. Calculations were performed based on a data set with SNR of 2.

Connectivity spectra of coherence (figure 41a) show relatively high correlation over the entire frequency band for almost all pairs of network nodes. Due to the high SNR of 2, peaks indicating information flow can be visually recognized. However, coherence is not able to distinguish between direct and indirect connections. Therefore, many false positive links are found by coherence before forward modelling (blue spectra) as well as after inverse source reconstruction (red spectra). Moreover, forward and inverse modelling does attenuate the spectra calculated after source reconstructions, but the deviation is rather low. Spectra of Granger causality (figure 41b) also indicate that this method could not fully distinguish between direct (1 to 3, 3 to 4 and 3 to 6) and indirect (1 to 4 and 1 to 6) information flow amongst nodes. However, in contrast to coherence, it reconstructed all simulated links and did not show any indication of false positive correlation between other network nodes. Another advantage of Granger causality, that was already outlined

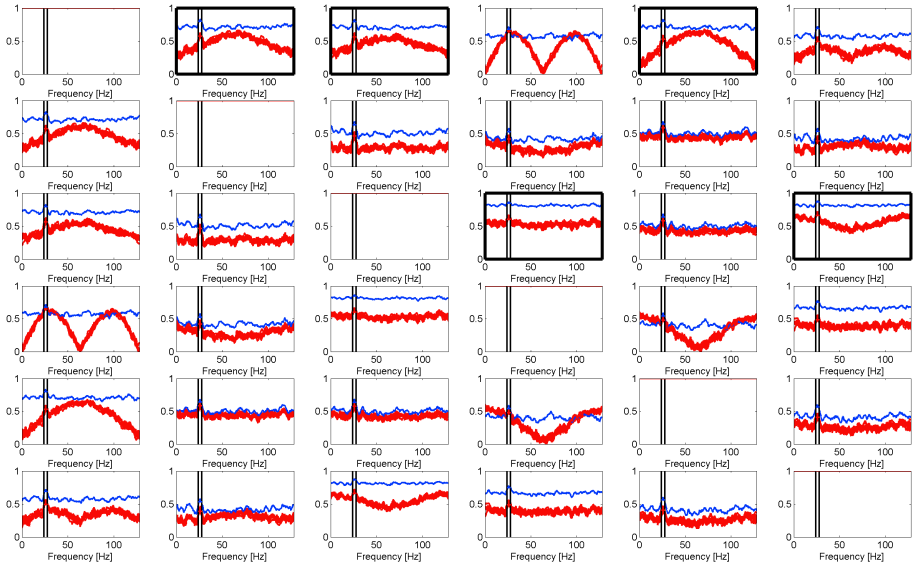

(a) Coherence

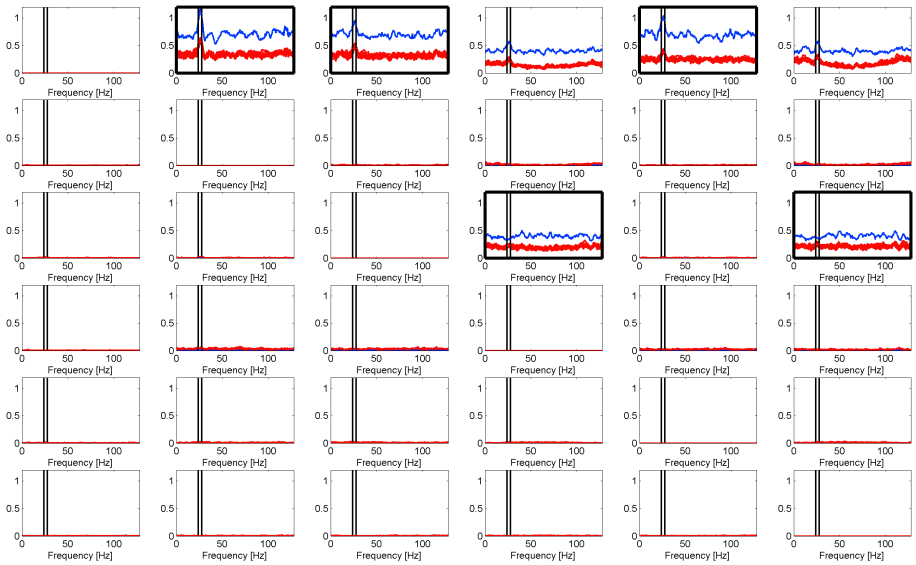

(b) Granger causality

Figure 41: Connectivity spectra for simulated (blue) and reconstructed (red) networks of coherence (top) and Granger causality (bottom). Correlations between nodes shown in this graph are based on a network with 6 sources, as illustrated in figure 40b. Connectivity estimation of visualized data was performed on data sets with a length of 100 s and SNR of 2. Simulated direct connections between nodes are accentuated by a bold frame.

in previous experiments is the suppression of noise outside the frequency range of interest. Network reconstructions obtained by DTF (figure 41c) largely coincide with spectra of Granger causality. DTF also revealed difficulties in differentiating direct from indirect connections, indicating information flow from source 1 to source 4 and from source 1 to source 6. However, the overall noise level of DTF spectra are higher compared to Granger causality. Slightly superior results are achieved with PDC (figure 41d). In contrast to DTF

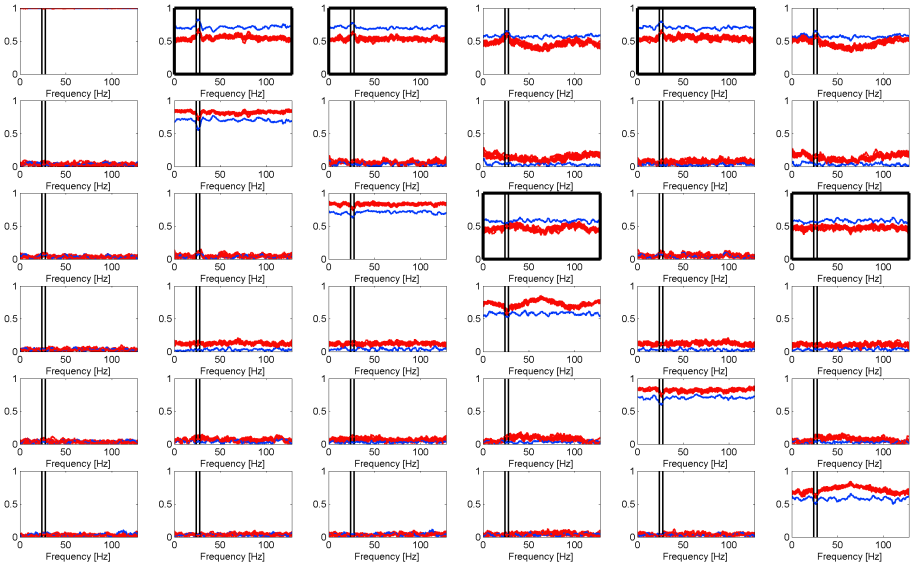

(c) DTF

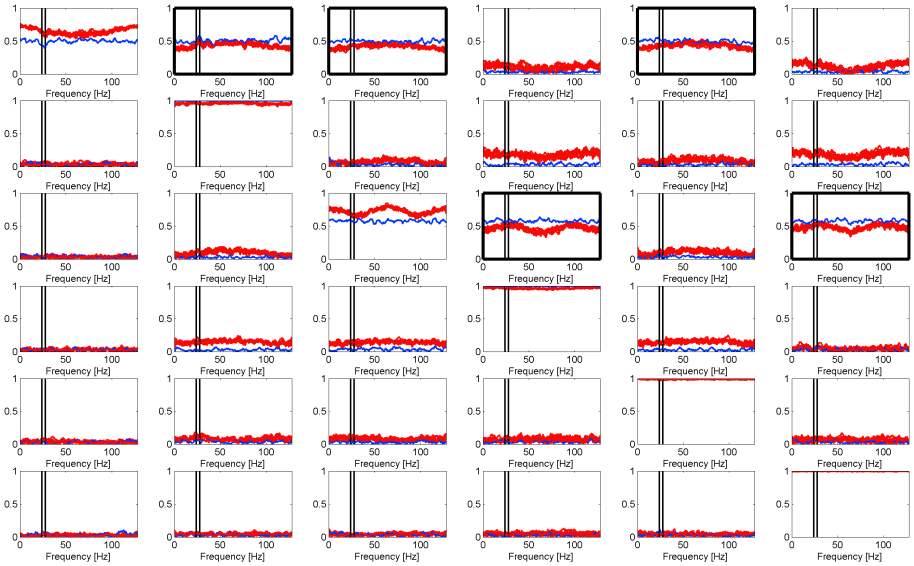

(d) PDC

Figure 41: Connectivity spectra for simulated (blue) and reconstructed (red) networks of DTF (top) and PDC (bottom) (cont.).

and Granger causality, this estimator is able to distinguish direct from indirect connections. The main disadvantage of this method is the high noise level over the entire frequency range, particularly for connected network nodes (e.g. for information flow from source 1 to source 3 and from source 1 to source 5). This makes a visual inspection of PDC spectra more difficult and prone to errors.

Spectra of network reconstructions for other network sizes showed similar results with coherence indicating a large number of false positive connections. To measure the overall performance of connectivity methods, Frobenius norm and AUC were calculated. Figure 42 shows Frobenius norm for coherence, DTF, PDC and Granger causality over network size.

The respective boxplots for AUC are illustrated in figure 43.

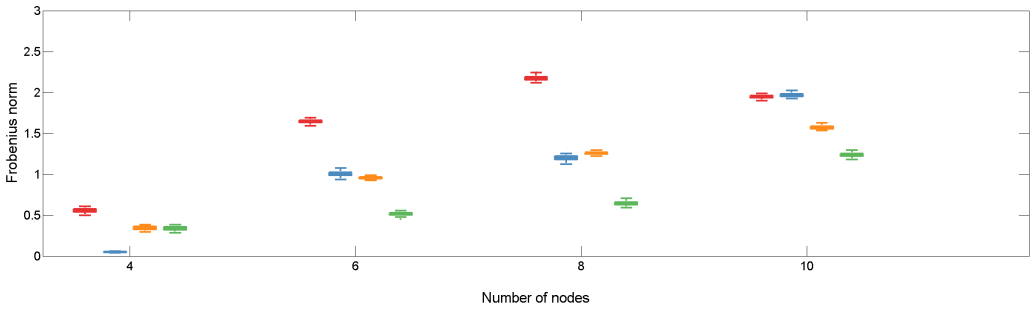

Figure 42: Frobenius norm of coherence (red), DTF (orange), PDC (green) and Granger causality (blue) over network size. Results are based on data sets with a length of 100 s and SNR of 2.

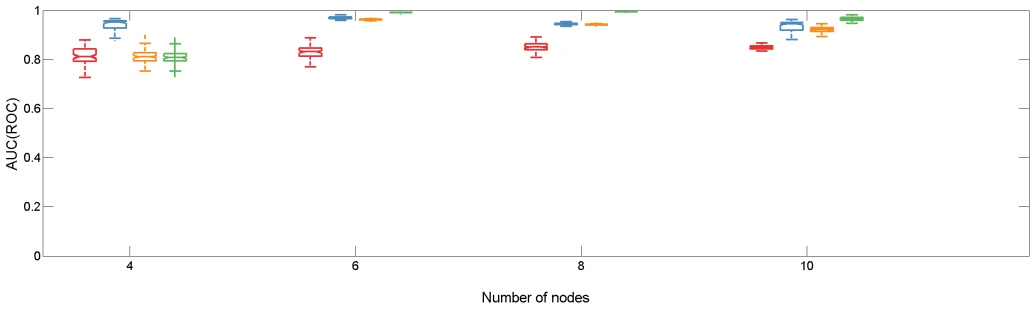

Figure 43: AUC of coherence (red), Granger causality (blue), DTF (orange), PDC (green) and Granger causality (blue) over network size. Results are based on data sets with a length of 100 s and SNR of 2.

Results of Frobenius norm indicate that an increase in network size leads to a larger distance between the simulated and the reconstructed network. However, it must be noted that results in figure 42 are not normalized by the number of network nodes. For a network with four nodes, Frobenius norm is computed by comparing the spectra of all 12 possible connections, whereas for a network consisting of 8 nodes, the number of possible connections increases to 56 (see table 4.8). Therefore, the deterioration as illustrated in the results of Frobenius can largely be explained by this effect. Furthermore, there is no indication of an increase of variance for larger network sizes. When focusing on the results from AUC, no significant change in accuracy or stability can be observed for larger networks.

Discussion

This simulation investigated the effect of network size on connectivity estimators. It was demonstrated that an increase in network size and therefore a larger number of possible connections make it difficult for methods like coherence to identify existing links between nodes and determine unconnected nodes correctly. Granger causality, DTF and also

PDC performed well in reconstructing simulated links and only had minor difficulties distinguishing direct and indirect connections. Due to low noise level over the entire frequency band, connectivity spectra of Granger causality were easy to evaluate and led to less error-prone results.

However, it must be stressed that an accurate and stable inverse source reconstruction is crucial for a subsequent connectivity estimation. In this series of experiments, source montages were used to minimize the effect of erroneous source localization and to enable an undistorted view on other important parameters. Such an error-free source reconstruction may not be possible when analysing real EEG and MEG data sets. Furthermore, reconstructing network sources becomes increasingly complicated with larger number of active nodes.

4.9 Simulation IX - Number of EEG Sensors

The number of electrodes placed on the surface of the head is an another critical factor for the reconstruction of cortical networks. Studies show that the number of EEG sensors has a substantial effect on the accuracy of localized source positions (Song et al., 2015) and the quality of brain network reconstructions from EEG recordings (Hassan et al., 2014).
Currently available EEG systems provide a large bandwidth of number of sensors ranging from only a few sensors up to high-density (hd) EEG systems with 256 channels. The choice of the system also often depends on the area of applications. In research applications, one can easily use EEG systems with 64 electrodes or more, whereas for practical or clinical applications, there may be stronger restrictions due to maintenance and upkeep cost of systems with a large number of sensors or the preparation time for EEG recordings.
In this simulation, electrode configurations from 16 to 256 sensors will be used to determine the effect of number of sensors on connectivity estimators. As described in the simulation study by Song et. al (Song et al., 2015), the number of sensors strongly affects source localization results and the reconstruction of the temporal activity pattern for each active brain region. Since source-waveforms serve as input data for connectivity methods to estimate network connections, a deterioration of the network reconstruction due to incorrect source localization is to be expected. This effect was also demonstrated in simulation VII - Source Localization Error (chapter 4.7) with larger localization errors leading to an increase of variance and less reliability of network reconstructions.

Simulation Setup

This simulation is based on a brain network model consisting of eight dipoles as introduced in simulation VIII - Network Size (chapter 4.8). Figure 44 illustrates the dipole positions and network connections for the respective nodes. Connections between cortical nodes for this network were designed to mainly consist of a posterior-to-anterior pattern of information flow. A detailed overview on the positions and orientations of sources is given in table A4 in the appendix of this thesis.
Cortical background white-noise signal was simulated by adding 20 noise sources to the simulation distributed evenly in brain space. For every electrode configuration, 100 data sets were computed with noise sources carrying random white noise signal for each iteration. Scaling of the noise topographies to obtain a SNR of 1 for each data set was carried out in the frequency domain after forward modelling activities from noise and network dipoles for 16 to 256 scalp channels. The sensor labels and positions for EEG setups consisting of 16 (table A8), 31 (table A9), 64 (table A10), 128 (according to the $10-5$ electrode configuration as proposed by Oostenveld and Praamstra, 2001) and 256 electrodes (according to Suarez et al., 2000) are listed in the appendix. Figure 45 provides a topographic view on the five

Table 4.10

Overview of key parameters and settings for simulation IX - Number of EEG Sensors. The parameter examined in this simulation is indicated in bold type.

Parameter	
Data length	100 s
Signal-to-noise ratio	1
Number of network nodes	8
Number of noise nodes	20
Number of electrodes	**16 - 128**
Number of iterations	100
Head model	Realistic standardised FEM head model
Regularization	1%
Localization error	0 mm
Connectivity methods	Coherence, imaginary part of coherency, DTF, PDC and GC

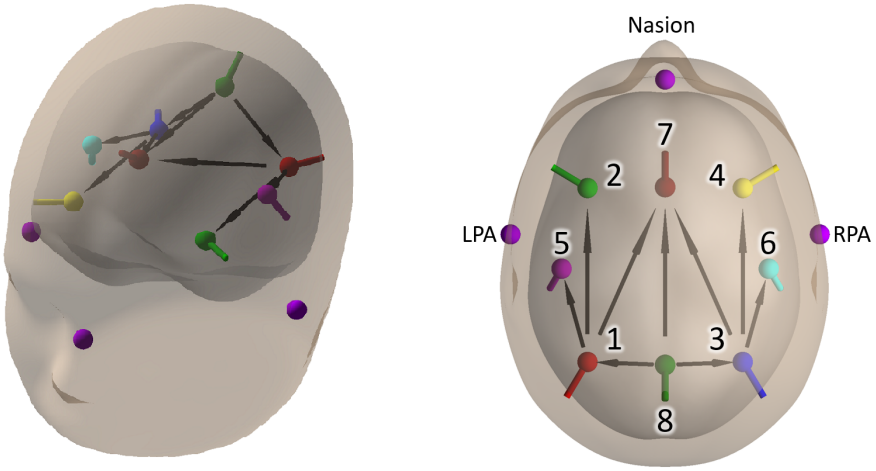

Figure 44: Front-left and top view of head-model including network nodes and connections used in this simulation. Arrows indicate direct connections between the respective network nodes. Fiducials (nasion, left and right pre-auricular points) are indicated as purple spheres.

different sensors layouts.

Each simulated data set consisted of a 100 s recording at a sampling rate of 256 samples per second.

Reconstruction of cortical activity was carried out based on a source montage with eight dipoles located at locations and orientations identical to the simulated sources and a regularization factor of 1%.

In contrast to previous simulations in which the reconstructed cortical network was compared with the simulated network in order to make statements about the accuracy and reliability

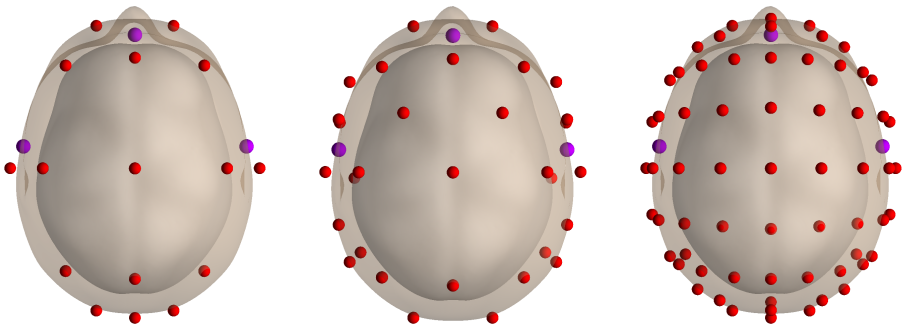

(a) 16 electrodes (b) 31 electrodes (c) 64 electrodes

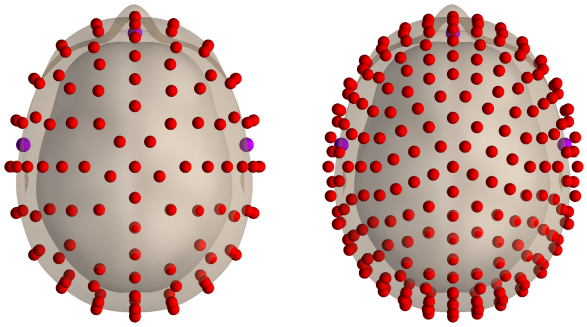

(d) 128 electrodes (e) 256 electrodes

Figure 45: Sensor configurations for 16 to 256 electrodes (red spheres) used in this simulation. Detailed labels and positions of sensors for each layout are outlines in the appendix of this thesis.

of connectivity estimators, further statistical analyses were carried out in this experiment. This evaluation relates in particular to the parameter set based on an electrode layout of 64 sensors. The extended statistical analysis is based on the comparison of the reconstructed data with connectivity thresholds obtained from phase-randomized surrogate data (Theiler, Eubank, Longtin, Galdrikian, and Doyne Farmer, 1992, Prichard and Theiler, 1994), a method designed to test for non-zero information transfer in a dynamical system. Instead of a direct permutation of samples which would entirely destroy the correlation structure of source-waveforms, only the phases of each time-series are randomized to preserve their amplitude distribution. Each realization of surrogate data is obtained by transforming source-waveforms after inverse source reconstruction into the Fourier domain where the phases of the Fourier coefficients are randomly permuted before finally applying the inverse Fourier transform. Connectivity estimators are then recomputed. The resulting connectivity threshold of each iteration was calculated in two different ways: a) by calculating the mean in the frequency range of interest (24 Hz to 28 Hz) and b) by determining the maximum connectivity value over the entire frequency range. Repeating this procedure many times generates the empirical distribution against which the reconstructed value of the connectivity estimator is compared. In this simulation, 1000 iterations were computed to obtain distributions for both approaches based on a significance level of $p = 0.05$ for rejection

of the null hypothesis. Frobenius norm and area under ROC curve were determined for the comparison between the reconstructed cortical network and the connectivity thresholds. This additional analysis was only carried out for the simulation with 64 sensors. The statistical comparison between the simulated and reconstructed network as used in previous simulations, however, was applied to all parameter sets of this experiment.
In the further course of the chapter, the different statistical evaluations are abbreviated as follows:

- TFree: threshold free approach contrasting the connectivity spectra of the simulated and the reconstructed network as outlined in section 3.4.
- TMean: statistical evaluation based on thresholds obtained by computing mean connectivity in the frequency range of interest.
- TMax: comparison of the reconstructed connectivity spectra with thresholds derived from determining the maximum connectivity value over the entire frequency range.

Furthermore, the analysis of different statistical methods includes results of additional connectivity estimators. Network reconstructions based on computations of dDTF (2.27) and sPDc (2.30) were carried out for the data set including 64 sensors.

Results

This section presents the performance of connectivity methods depending on how many EEG sensors were taken into account during inverse source reconstruction. As a first measure, connectivity spectra indicating the information flow from source one to source two for all numbers of EEG sensor levels are illustrated in figure 46.
Each plot shows the superimposed spectra of 10 out of 100 iterations for the respective connectivity method. For the selected connection from source one to source two, an information flow was simulated in the frequency range of 24 Hz to 28 Hz. This connection is clearly recognizable in the spectra of the simulated network (blue curves) for all estimators. Superimposed spectra of reconstructed networks (red curves), however, show clear differences between the respective number of channels. No distinct peak can be determined in the corresponding frequency range for all connectivity spectra based on 16 channels. When 31 or more scalp electrodes are taken into account during inverse source reconstruction peaks of high correlation are more prominent and can be recognized more easily. As already demonstrated in previous experiments, DTF and PDC tend to produce spectra with higher noise level over the entire frequency range compared to Granger causality. Despite the high noise levels of DTF and PDC, peaks of high correlation in the frequency range of interest can be clearly identified without much effort.
With an increase in number of channels, the variance of the connectivity spectra for DTF,

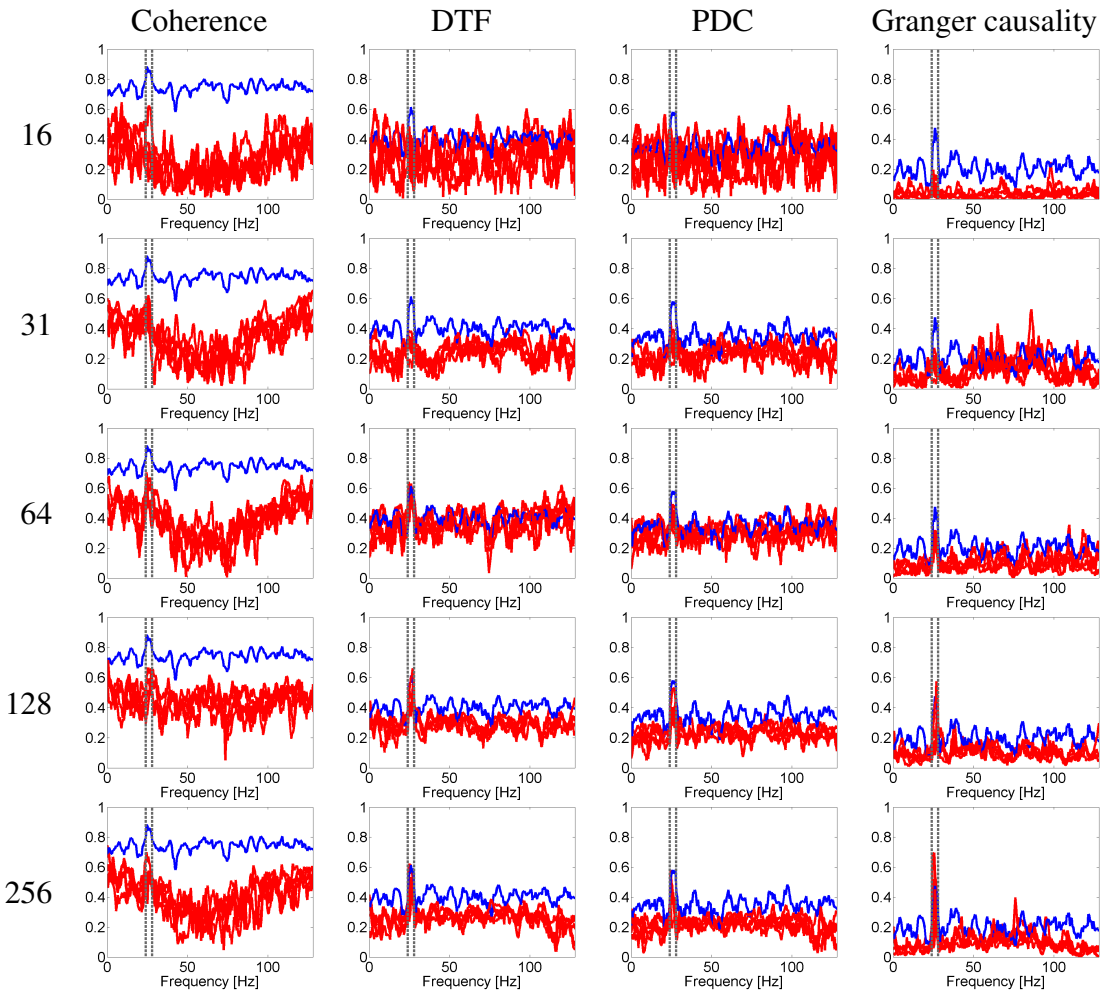

Figure 46: Connectivity spectra showing simulated (blue) and reconstructed (red) information flow from source one to source two for coherence, DTF, PDC and Granger causality. Each row represents a different number of EEG sensors (16 to 256 channels) used during source analysis based on a source montage with a regularization constant of 1%.

PDC and Granger causality can be reduced. Coherence, on the other hand, does not show a noticeable decrease in variance over the entire frequency range with higher numbers of sensors. Due to a constant SNR level for all simulations, the mean noise level is not reduced for all methods if more scalp electrodes are taken into account.

Statistical analysis results contrasting differences in the accuracy of network reconstructions depending on the number of used sensors are shown in figure 47, illustrating Frobenius norm, and in figure 48, displaying AUC.

Boxplots of Frobenius norm and AUC provide a clearer representation of the quality of network reconstructions than connectivtiy spectra, which may be difficult to interpret. Both figures clearly indicate that the accuracy of the network reconstruction increases with a higher number of sensors for all connectivity estimators.

Figure 47 shows that PDC provides lowest Frobenius norm values, even for small numbers of sensors (16 and 31 sensors), followed by DTF and Granger causality. Coherence, on the

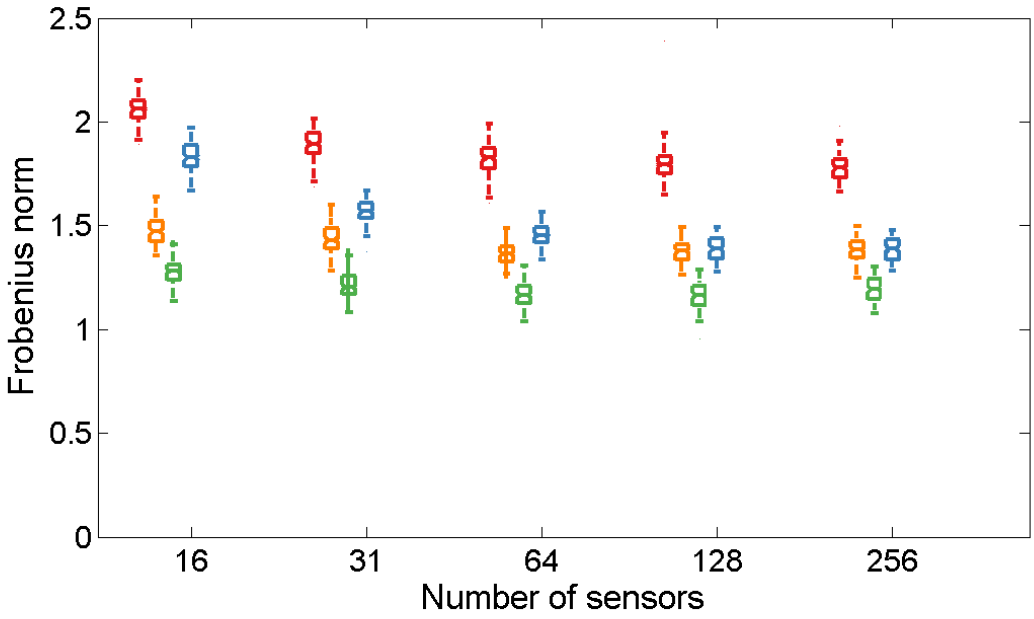

Figure 47: Frobenius norm of coherence (red), DTF (orange), PDC (green) and Granger causality (blue) over number of EEG sensors. Results are based on data sets with a length of 100 s and SNR of 1.

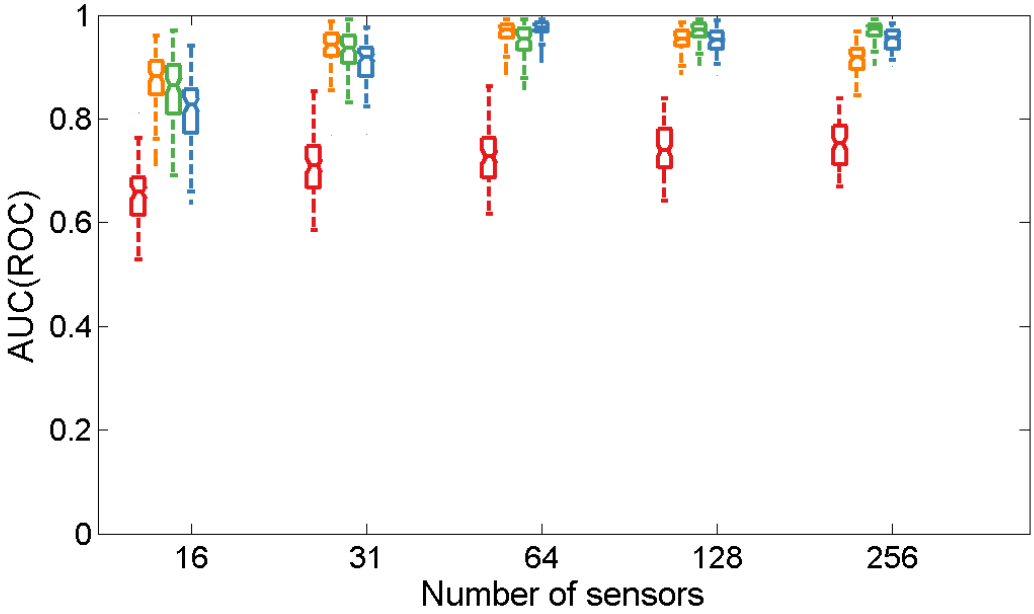

Figure 48: AUC of coherence (red), DTF (orange), PDC (green) and Granger causality (blue) over number of EEG sensors. Results are based on data sets with a length of 100 s and SNR of 1.

other hand, provides a significantly higher deviation from the simulated network. There is a non-linear improvement in the results for all methods with an increase in the number of sensors, with results of all estimators converging against a limiting Frobenius norm value. An increase in the number of electrodes from 16 to 31 and from 31 to 64 sensors yields a significant improvement in the accuracy of network reconstruction. However, a further

increase up to 128 or even 256 sensors led only to minor benefits regarding the precision of connectivity estimators. Variance of results, indicated by the vertical distance between the lower and upper whisker remains stable for all methods regardless of the number of electrodes used during source reconstruction.
Results based on AUC (figure 48) confirm the findings derived from Frobenius norm boxplots. Statistical evaluation based on AUC also validate a convergence to a limiting value with an increasing number of sensors. Results of DTF, PDC and Granger causality do not indicate any significant differences between these methods and provide a more sufficient degree of stability and accuracy than coherence. The non-linear improvement in network reconstruction with an increase in the number of sensors can also be observed for AUC.
The statistical evaluations listed in the paragraph above built on a comparison of the simulated network with the reconstructed network across a range of thresholds. In the following, additional statistical assessments are shown which represent an alternative to this approach. These computations are based on connectivity thresholds obtained from phase-randomized surrogate data. The data set including an electrode layout of 64 sensors was used for this evaluation.
Figure 49 shows connectivity spectra of coherence, DTF, dDTF, PDC, sPDC and Granger causality for a connected pair of sources and for an unconnected pair of sources.

In addition to the simulated (blue curves) and reconstructed (red curves) connectivity spectra, limits defining the thresholds for spurious and real information flow have been added for each connection. The limiting value defined by computing TMean is indicated by green dashed lines, whereas the threshold obtained from evaluating the TMax is indicated by orange dashed lines. TMax thresholds are consistently above TMean values and should therefore be seen as a more conservative estimate.
For the simulated connection from source one to source two, only the largest connectivity values that are in the frequency range of 24 Hz to 28 Hz are above TMax. In addition, connectivity estimation indicate real information flow around a frequency of 120 Hz that exceed the threshold but have not been simulated. TMean values are well below TMax for all methods. Due to the liberal thresholds, connectivity values repeatedly exceed this limit over the entire frequency range. It is therefore less suitable to correctly differentiate between spurious connectivity and real information flow.
The connection from source two to source six represents an example of a network links that does not imply any simulated information flow. Due to overall lower connectivity values compared to the example with a simulated connection between sources, both thresholds are providing lower limits for all connectivity estimators. Spectra of DTF, dDTF, PDC, sPDC and Granger causality do not exceed the TMax threshold, whereas connectivity estimation based on coherence wrongly indicates a significant correlation in the frequency range of

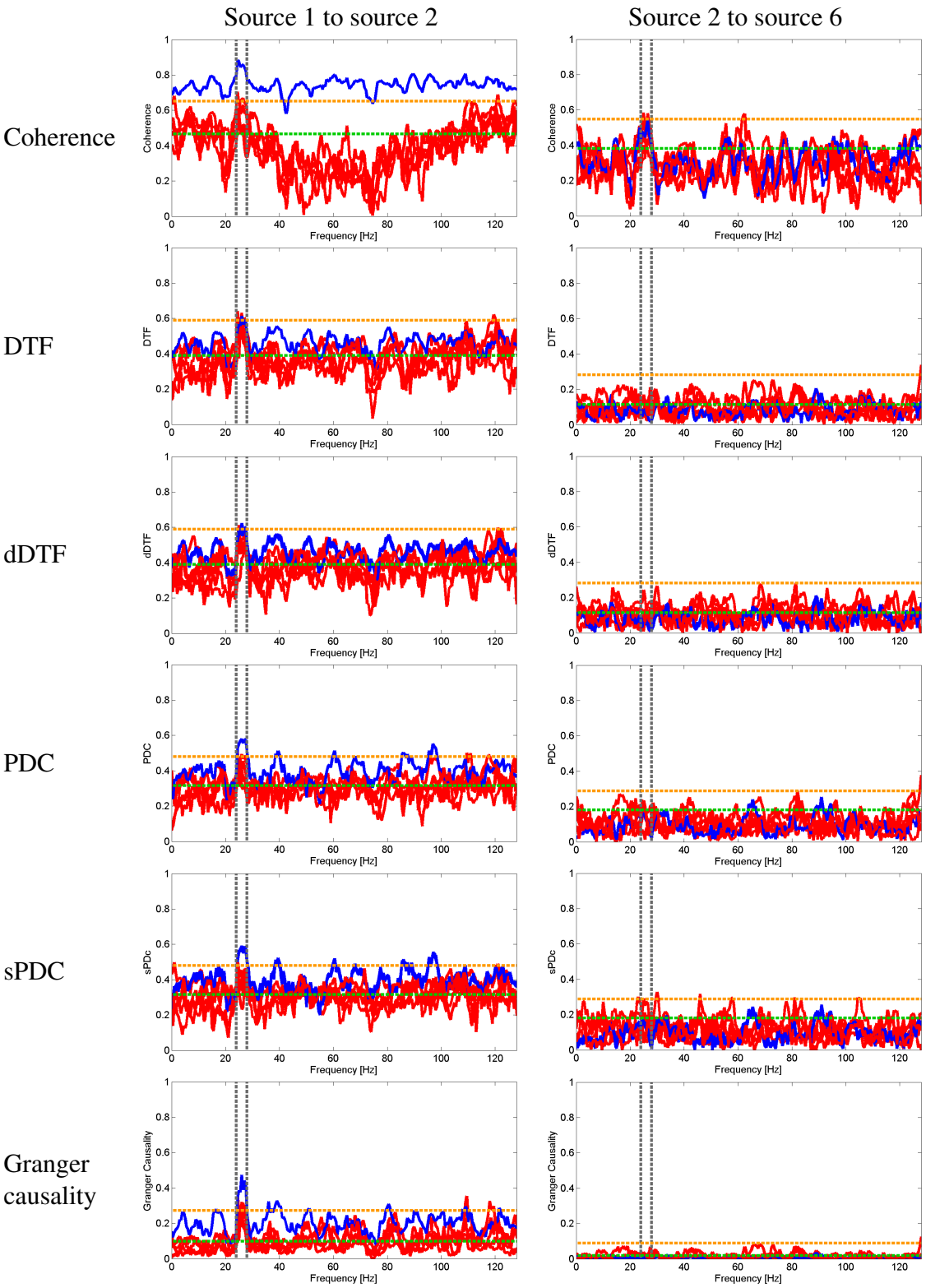

Figure 49: Connectivity spectra showing simulated (blue) and reconstructed (red) information flow for a connected pair of sources (left column) and for an unconnected pair of sources (right column) for coherence, DTF, dDTF, PDC, sPDC and Granger causality. Dashed lines indicate thresholds obtained from phase randomized surrogate data via computation of TMean (green) or calculation of TMax (orange).

interest (24 Hz to 28 Hz) as well as for frequencies around 65 Hz. Similar trends can only be identified for sPDC. As in the previous example, TMean is less conservative than TMax. As a result, connections exceeding the thresholds for specific frequencies across the entire spectrum may be considered significant.

Newly added connectivity estimators, dDTF and sPDc are based on a modified derivation or normalization of DTF and PDC, respectively. The comparisons of connectivity spectra between DTF and dDTF or PDC and sPDC show only negligible differences between the methods.

Figures 50 and 51 illustrate results for Frobenius norm and AUC, comparing the three different statistical evaluations: threshold free approach (TFree), thresholds based on mean connectivity in the frequency range of interest (TMean) and maximum connectivity value over the entire frequency range (TMax).

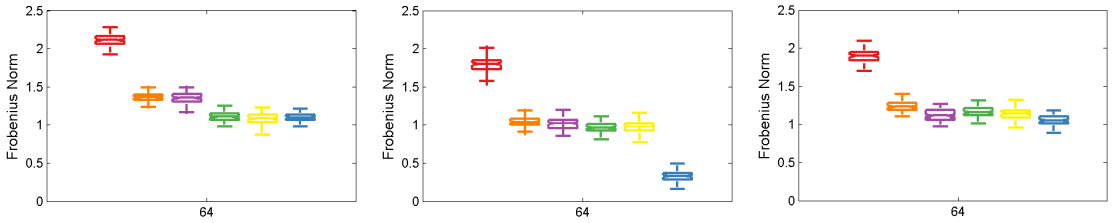

(a) Threshold free (b) Mean connectivity (c) Maximum connectivity

Figure 50: Frobenius norm over 64 EEG sensors for coherence (red), DTF (orange), dDTF (purple), PDC (green), sPDC (yellow) and Granger causality (blue). Statistical evaluation was performed using TFree (50a) and threshold based approaches TMean (50b) and TMax (50c) derived from phase randomized surrogate data.

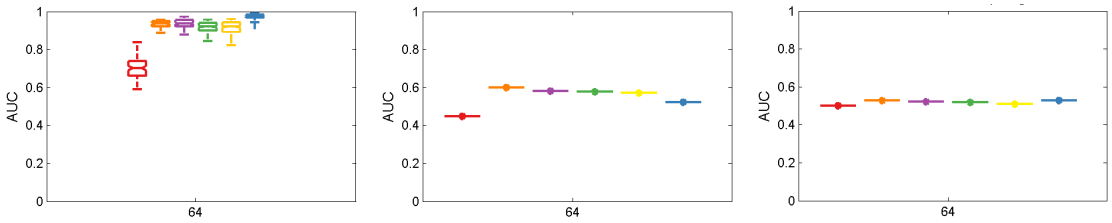

(a) Threshold free (b) Mean connectivity (c) Maximum connectivity

Figure 51: AUC over 64 EEG sensors for coherence (red), DTF (orange), dDTF (purple), PDC (green), sPDC (yellow) and Granger causality (blue). Statistical evaluation was performed using TFree (50a) and threshold based approaches TMean (50b) and TMax (50c) derived from phase randomized surrogate data.

Frobenius norm boxplots show great agreement between the three statistical methods. For coherence, DTF and PDC in particular, the results of TFree, TMean and TMax are almost identical. Due to the more conservative values, the results of TMax indicate a slightly larger difference between the thresholds and the reconstructed network than TMean. This is particularly evident for Granger causality, which provides significantly lower Frobenius

norm for TMean than TFree and TMax. It is worth noting the high consistency between TFree and TMax.
Findings of AUC presented in figure 51 are more difficult to compare. TMean and TMax provide mean AUC values instead of boxplots since each iteration enables only a single comparison between the respective threshold and connectivity spectrum. The results of TMean and TMax lead to similar conclusion that all connectivity estimators can only very poorly reconstruct the simulated connections between network sources. However, connectivity spectra shown in figure 49 must be taken into consideration to correctly interpret these results. Thresholds from TMean are less conservative and therefore susceptible to improperly indicated connections between network nodes that have not been simulated. This leads to a large number of false positives. In contrast to TMean, the poor performance of the connectivity methods for TMax is due to the highly conservative thresholds this statistical evaluation provides. Therefore, only a few of the simulated connections between sources are correctly identified as such. This results in a small number of true positives, affecting the true positive rate (sensitivity) used in the ROC curves. More meaningful findings are achieved with TFree. From these results it is clear that DTF, dDTF, PDC, sPDC and Granger causality are able to reconstruct the simulated cortical network most accurate and reliable. The outcome of these estimators are substantially better than coherence, which shows significantly worse results with a higher variance.

Discussion

This simulation was designed to reveal the effect of number of EEG sensors on the performance of connectivity methods. In order to investigate this effect, data sets with 16 up to 256 sensors were simulated involving a cortical network consisting of 8 nodes. On the basis of this experiment, it could be shown that the number of sensors that are taken into account during inverse source reconstruction is of great importance for network reconstructions. This analysis found evidence for an improvement in accuracy and precision of network reconstructions with an increase of number of sensors for all estimators. Connectivity methods provide significantly better results for an increase in number of electrodes from 16 to 31 and from 31 to 64 sensors. A further increase only led to negligible improvements. This non-linear trend was demonstrated both in results of Frobenius norm and AUC. Overall these findings are in accordance with findings reported by previous studies indicating considerably superior results when increasing the number of sensors (Hassan et al., 2014).
However, the optimal number of sensors mainly depends on the algorithm that is applied to localize and reconstruct cortical activity from scalp data but is also related to other parameters used in the analysis pipeline of EEG and MEG data. Many studies have shown that at least 64 to 128 EEG sensors are required to achieve satisfactory results to localize

cortical activity (Lantz, Grave de Peralta, Spinelli, Seeck, and Michel, 2003, Song et al., 2015) or reconstruct functional networks (Hassan et al., 2014).

Moreover, this experiment included further statistical methods to assess the accuracy and reliability of connectivity estimators. Reconstructed spectra were compared against thresholds obtained from phase-randomized surrogate data (Theiler et al., 1992, Prichard and Theiler, 1994) to distinguish between spurious connectivity and real information flow. Thresholds were derived by computing mean connectivity in the frequency range of interest or determining the maximum connectivity value over the entire frequency range. Both approaches were compared to a threshold free approach contrasting the connectivity spectra of the simulated and the reconstructed network. The impact of the respective statistical technique was different for the performance measures used in the simulation. Similar patterns of results were obtained for Frobenius norm. In contrast, AUC showed significantly different values depending on how strict the thresholds were defined.

Chapter 5

Application of Connectivity Measures to EEG Recordings

The usefulness and knowledge of the results from the simulation studies will be demonstrated by analysing resting-state connectivity EEG recordings on the source level.

Oscillations in the alpha frequency range (7-14 Hz) were first observed by Berger (Berger, 1929) using EEG recordings. Activity within this alpha band, represents fluctuations in cortical excitability (Romei et al., 2008) triggered by selective attention (Klimesch, Sauseng, and Hanslmayr, 2007, Jensen and Mazaheri, 2010). The modulatory role of alpha has been shown for multiple modalities, such as the visual (Ploner, Gross, Timmermann, Pollok, and Schnitzler, 2006, Snyder and Foxe, 2010), somatosensory (Della Penna et al., 2004, Haegens, Handel, and Jensen, 2011) and auditory domain (Bastiaansen, Böcker, Brunia, de Munck, and Spekreijse, 2001, Weisz, Hartmann, Müller, Lorenz, and Obleser, 2011) and has been linked to perceptual consequences including vigilance (Papadelis et al., 2007, Schubert, Haufe, Blankenburg, Villringer, and Curio, 2009) and fatigue (Simon et al., 2011). These studies modulate alpha activity in a repeatable, task-evoked experimental design by controlled manipulation of selective attention. However, these techniques are not applicable for the analysis of resting-state data due to the absence of a controlled manipulation, which makes the reconstruction of underlying cortical networks particularly problematic.
Nevertheless, resting-state networks (RSNs) have been successfully reconstructed in recent years with fMRI data (Biswal, Yetkin, Haughton, and Hyde, 1995), combined fMRI and EEG (Mantini, Perrucci, Del Gratta, Romani, and Corbetta, 2007), fMRI and MEG (de Pasquale et al., 2010), MEG (Hillebrand, Barnes, Bosboom, Berendse, and Stam, 2012, Florin and Baillet, 2015, Hillebrand et al., 2016) and EEG (Pascual-Marqui et al., 2014).
In this chapter, we analyse publicly available EEG recordings (Trujillo, Stanfield, and Vela, 2017) and attempt to reconstruct information flow of a RSN with dominant posterior-to-anterior connection pattern in the alpha frequency band. This network has been

analysed and studied in detail by Hillebrand et al. (Hillebrand et al., 2016). In this study, an atlas-based time-domain beamformer (Hillebrand et al., 2012) was applied to transform MEG sensor data to source space for a predefined grid with equidistant spacing of 2 mm. To reduce data dimensionality, ROIs were defined from the automated anatomical labeling (AAL) atlas (Tzourio-Mazoyer et al., 2002), resulting in a single time-series per ROI. Subsequently, phase transfer entropy (PTE; Lobier, Siebenhühner, Palva, and Palva, 2014) was applied to reconstruct information flow between ROIs. In table *S*4 of the supplementary information material of this work, Hillebrand lists the 100 strongest connections between pairs of regions in the alpha2 (10 - 13 Hz) and theta (4 - 8 Hz) band in rank order.
This work focusses on the 10 strongest connections of the default mode network in the alpha2 frequency band to compare network reconstructions obtained from different connectivity estimators. Due to the restriction of taking only a subset of the most pronounced network links into account, the total number of cortical areas involved in the DMN can be narrowed down to 8 nodes. Table 5.1 lists the 8 brain regions and their corresponding abbreviations that are used in this study.

Table 5.1

Brain regions involved in the information transfer of the 10 *strongest network connections in the alpha*2 *DMN.*

Cortical region	Abbreviation
Anteriorcingulate and paracingulate gyri, right	ACG right
Calcarine fissure and surrounding cortex, left	CAL left
Calcarine fissure and surrounding cortex, right	CAL right
Cuneus, left	CUN left
Cuneus, right	CUN right
Inferiorfrontal gyrus, triangular part, right	IFGtriang right
Superiorfrontal gyrus, medial part, left	SFGmed left
Superiorfrontal gyrus, medial part, right	SFGmed right

The 10 most significant connections identified by pairs of sending and receiving nodes of the alpha2 network are listed in table 5.2.
The following sections of this chapter introduce the dataset (section 5.1), present the data analysis process (section 5.2), including pre-processing, inverse source reconstruction and connectivity analysis and illustrate results of network reconstructions obtained by different connectivity measures (section 5.3). Finally, a discussion on the performance and differences between estimators is provided in section 5.4.

Table 5.2

List of 10 *strongest connections of the alpha*2 *network in rank order according to Hillebrand et al. (Hillebrand, Barnes, Bosboom, Berendse, and Stam, 2012).*

Source node	Target node
CAL left	IFGtriang right
CUN left	ACG right
CAL left	SFGmed left
CAL left	ACG right
CUN left	IFGtriang right
CUN right	IFGtriang right
CUN right	ACG right
CUN left	SFGmed right
CAL right	SFGmed left
CUN left	SFGmed left

5.1 Datasets

The complete set of EEG recordings was shared by Trujillo et al. (Trujillo et al., 2017) and can be freely downloaded at the Texas Data Repository Dataverse (available from: https://dataverse.tdl.org/). The dataset includes recordings from 16 healthy subjects (aged 18-26) from the Texas State University. Each participant underwent 8 minutes of resting state EEG recording in a seated position in a darkened room. One minute epochs with eyes open and eyes closed were recorded alternatingly, resulting in a duration of four minutes for both conditions. During data acquisition, subjects remained in a relaxed, yet awake state. Written informed consent was obtained from each participant.

The subjects' continuous EEG were recorded using 72 active Ag/AgCl electrodes (67 scalp channels and 5 polygraphic channels) in the international 10/5 system (Jurcak, Tsuzuki, and Dan, 2007), as illustrated in figure 52 with the sensors either attached to a BioSemi electrode headcap or via freestanding electrodes. Labels and positions of sensors are listed in table A11 in the appendix of this thesis.

A BioSemi ActiveTwo amplifier system with a resolution of 24-bit ADC (analog to digital converter) recorded the signal of each electrode at a sampling rate of 2048 Hz and down-sampled it to 256 Hz. The signals of each scalp electrode was referenced to a common mode sense (CMS) sensor placed between electrodes PO3 and POZ.

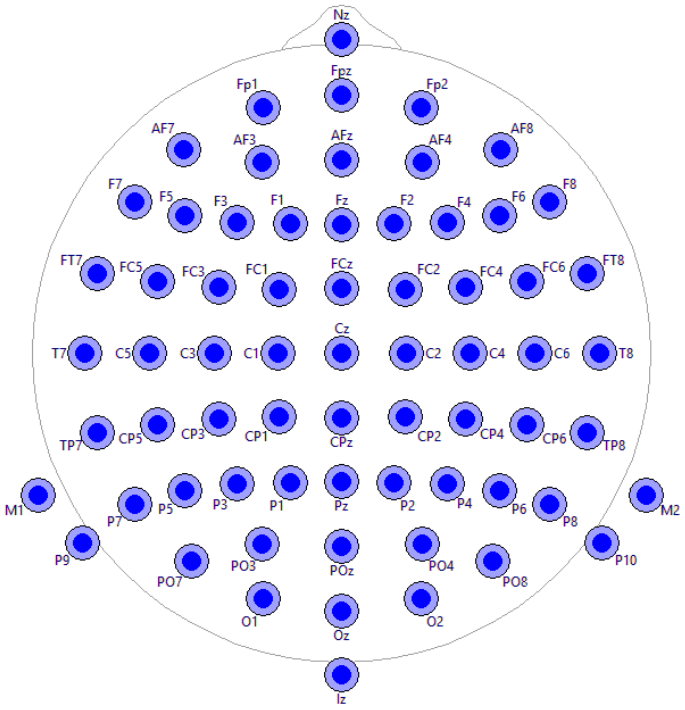

Figure 52: Sensor configuration of BioSemi headcap with 72 electrodes.

5.2 Method

Similar to simulated data sets described in chapter 4, real EEG data was analysed using BESA Research 7.0 June 2018 (BESA GmbH, Germany) and the open-source toolbox Fieldtrip (Oostenveld et al., 2011) in combination with MATLAB 7.4.0.287 (The MathWorks, Inc., Natick, Massachusetts, United States).

Preprocessing

Preprocessing of raw EEG data was done in BESA Research 7.0. During an initial visual inspection of each data set, bad channels as well as muscle and other artifacts were marked and the corresponding samples were excluded from further data analysis. Subsequently, each data file was scanned to detect and reject artifact-loaded channels and trials according to three criteria:

- Amplitude criterion: excludes trials that exceed the defined threshold (default: $120\mu V$) from further processing.
- Gradient criterion: defines the maximum difference (default: $75\mu V$) between two neighbouring time samples within a trial for a given channel.
- Low Signal criterion: rejects epochs during which the signal is smaller than the specified threshold (default: $0.01\mu V$).

Due to differences in the quality of EEG recordings between subjects, the default thresholds were adjusted for some data sets to exclude more artifact-loaded trials.

Inverse Source Reconstruction

Reconstruction of the 10 strongest connections of the alpha2 default mode network is based on a source configuration with 8 active brain regions. The AAL atlas (Tzourio-Mazoyer et al., 2002) was used to define the volume of distinct cortical areas. In line with the inverse source reconstruction technique applied in the simulations, each active brain region was represented by a single dipole. This reduction of data dimensionality also provides a more concise and informative approach for later calculation of connectivity. Coordinates of sources were defined by calculating the centroid for the respective region, by taking all voxels of the related brain area into account. To estimate the predominant orientation for each voxel position, Hillebrand used a scalar-type beamforming technique (Hillebrand et al., 2012). This approach is most accurate and reliable only if individual anatomical information is available for each subject (Sekihara and Nagarajan, 2008, Steinsträter, Sillekens, Junghoefer, Burger, and Wolters, 2010). For this experiment, no individual MRI recordings were available to compute subject-dependent head models. Therefore, orientations of active brain regions were chosen to be radial, based on a four-shell spherical head-model (Scherg et al., 2002). The resulting dipole model provided the basis for source montages that were used to transform sensor data into brain space and to calculate the time-dependent activity of each brain region. In addition to the 8 dipoles representing the DMN, 3 regional sources were added (middle temporal gyrus left, superior temporal gyrus right and supplementary motor area right) in order to explain background activity from unmodelled brain areas. Adding these noise sources lead to a less noisy and more reliable estimation for the time-courses of network nodes. Figure 53 illustrates the resulting source configuration.

For the calculation of the source montages, a four-shell (brain, CSF, skull and scalp) spherical head model (Berg and Scherg, 1994) was applied. To provide adequate values for bone conductivities of adults, a conductivity ratio (CR) of radial skull conductivity and brain conductivity of $1 : 80$ was chosen. This CR produces comparable locations in depth compared to a standardised, 3 compartment (brain/CSF, skull and scalp) isotropic FEM head-model with default parameters. Furthermore, the regularization constant was set to 1% for all dipoles. After applying the resulting source montage on the pre-processed data sets, the time-courses of each network node were exported to MATLAB for subsequent connectivity estimation.

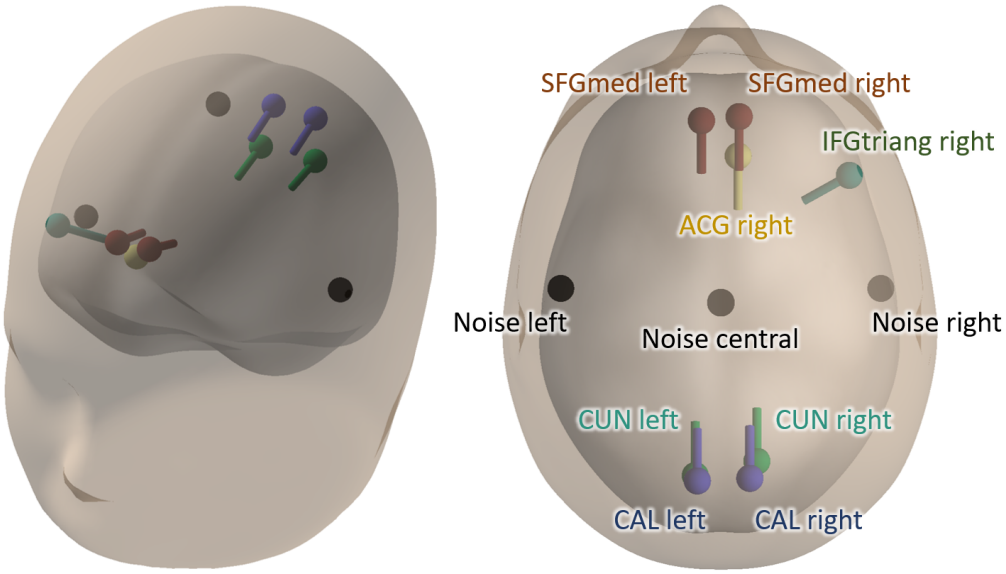

Figure 53: Positions of network nodes (colour-coded) involved in the alpha2 DMN. Additional noise sources are indicated in black colour. The coordinates and orientations of each source are listed in table A6.

Connectivity Analysis

Connectivity analysis was performed in MATLAB using several functional and effective connectivity estimators. Computations were executed based on the same source-code used for simulated data sets in chapter 4.
Reconstruction of brain networks was performed based on the temporal cortical activity of each network node obtained by inverse source reconstruction. For each subject, a data interval of 100 s was used as input to evaluate dependencies between distinct brain areas.

Statistical Analysis

In contrast to simulated data sets, the accuracy and reliability for the real EEG data analysis is challenging to estimate because the ground truth is not known. Despite the fact that the DMN has been extensively analysed in previous studies providing a high level of a priori knowledge, it is nevertheless particularly difficult to correctly interpret results of connectivity estimators and to draw correct conclusions. Moreover, connectivity methods based on a model-based or non-parametric estimation of the transfer matrix and the noise covariance matrix have a non-linear dependency to the data from which they are derived. Therefore, the distribution of connectivity estimates for each method must be determined individually for every subject to distinguish real connections from spurious connectivity.
In order to define thresholds for the statistical significance of connectivity values, a non-parametric statistical test using surrogate data (Prichard and Theiler, 1994, Schreiber and Schmitz, 2000) was applied. The time-series of the eyes-closed condition for each

subject were Fourier transformed. Magnitudes of the Fourier coefficients remained unchanged, but the phases were shuffled randomly. Subsequently, the inverse Fourier transformation was calculated to create new surrogate time-series. Connectivity estimation was performed for the surrogate data sets. This process was repeated 100 times to obtain an empirical distribution for all connectivity methods under the condition that the null hypothesis of no correlation between network nodes is true. It should be noted that this statistical evaluation usually requires a higher number of iterations (typically 1000 iterations) in order to obtain a uniform distribution. Due to the high computational effort, however, this number was reduced to 100 repetitions. Based on a significance level of $p = 0.05$, method-based thresholds were computed and connectivity values below the thresholds were defined as spurious interactions and discarded.

5.3 Results

Results presented in this section outline the performance of connectivity estimators to correctly reconstruct the 10 most prominent connections of the alpha2 DMN.
Connectivity spectra indicating the information flow between the two most prominent connections (CAL left to IFGtriang right and CUN left to ACG right) are illustrated in figure 54. This visualization shows the superimposed results of all subjects for different connectivity estimators.
Spectra of all methods show well recognisable peaks in the alpha2 frequency range for both network connections, although it is evident that the connection between CAL left and IFGtriang right is much less pronounced than the connection between CUN left and ACG right. Moreover, it is also clearly noticeable that the onset of the peaks start even earlier at approximately 6 to 7 Hz. This communication between network nodes in the alpha1 band (8 to 10 Hz) consists mainly of posterior-to-anterior patterns of information flow and coincides with findings from Hillebrand et al. (Hillebrand et al., 2012). This figure also demonstrates the advantage of Granger causality over other connectivity estimators in being able to successfully suppress noise outside the frequency range of interest, which was already outlined in the simulation studies.
The statistical evaluation carried out during the analysis of simulated data sets was also applied on the connectivity results of real EEG data to calculate the performance of each connectivity method regarding the accuracy and reliability of network reconstructions. For all simulations carried out in this thesis (chapter 4), Frobenius norm and area under ROC curve (AUC) were calculated by comparing the simulated network (ground truth) to the reconstructed network. Evidently this was not possible for real EEG data, due to the unavailable ground truth. Therefore, Frobenius norm was calculated comparing the

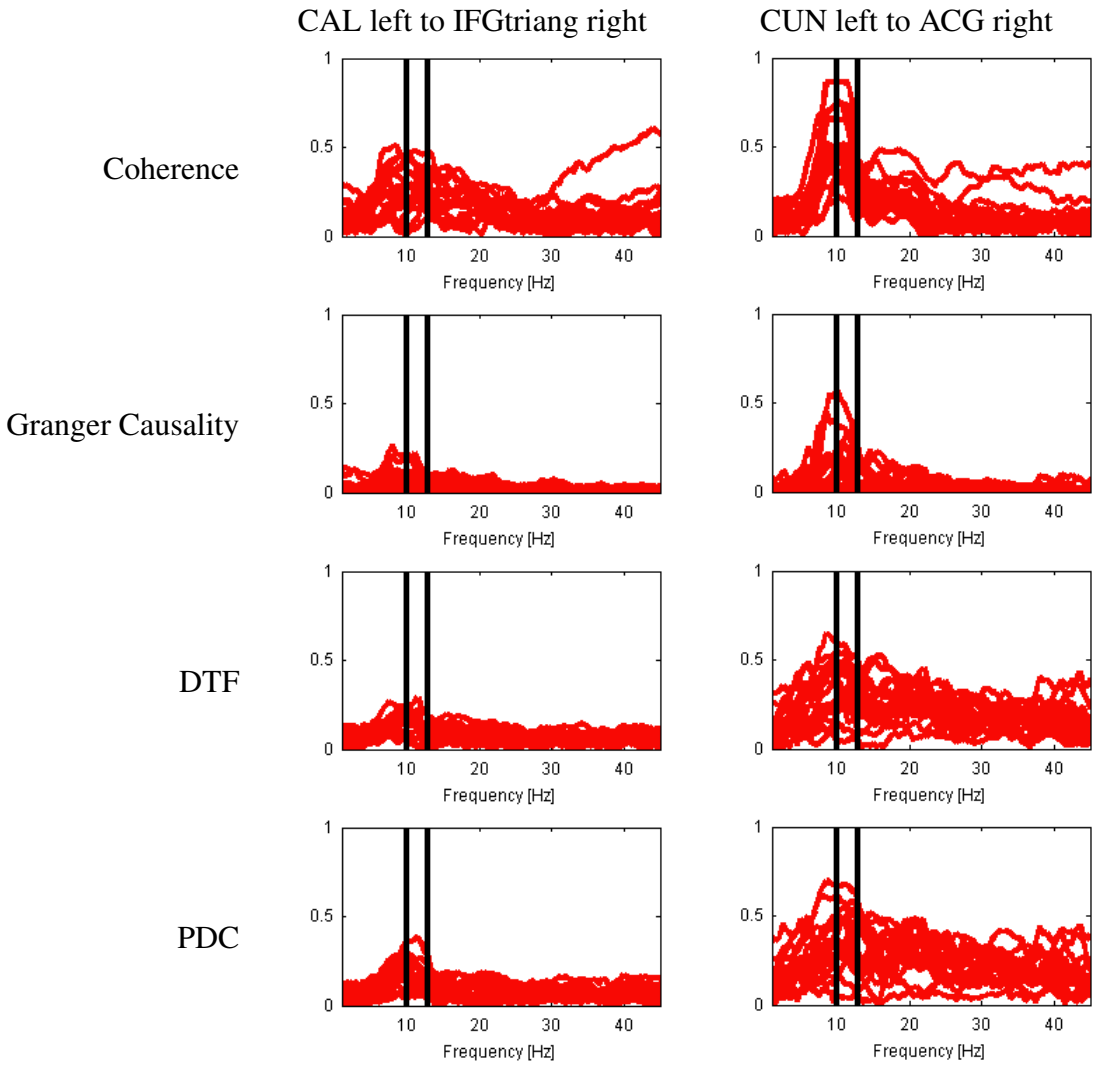

Figure 54: Superimposed connectivity spectra of all subjects for coherence, Granger causality, DTF and PDC over a frequency range of 1 to 45 Hz. Graphs indicate the information flow from CAL left to IFGtriang right (left column) and from CUN left to ACG right (right column). The frequency range of the alpha2 DMN (10 to 13 Hz) is indicated by vertical bars.

network reconstructions to the subject-dependent connectivity thresholds obtained via phase randomization. Figure 55 shows results of Frobenius norm for coherence, Granger causality, DTF and PDC.

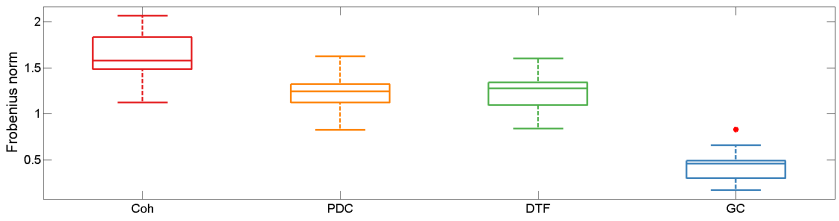

Figure 55: Frobenius norm of coherence (red), DTF (orange), PDC (green), and Granger causality (blue).

Boxplots of Frobenius norm indicate significant differences between methods, with Granger causality providing the most accurate connectivity estimations with the lowest deviation and variance compared to the computed thresholds. A one-way analysis of variance (ANOVA) was carried out to compare the Frobenius norm measures of connectivity estimators (table 5.3). This analysis confirmed the presence of a statistical difference between connectivity methods ($F(3,60) = 96.13$, $p < 0.0001$). A Scheffe post-hoc test further indicated that results from Granger causality ($M = 0.433$, $SD = 0.160$) and coherence ($M = 1.624$, $SD = 0.242$) differed significantly from all other methods at $p < 0.05$. No significant difference relationship between PDC ($M = 1.237$, $SD = 0.189$) and DTF ($M = 1.248$, $SD = 0.192$) was found.

Table 5.3

Result of one-way ANOVA test showing the variation between connectivity estimators for results of Frobenius norm.

	SS	df	MS	F	Prob > F
Methods	12.08	3	4.0267	96.13	< 0.0001
Residual	2.5133	60	0.0419		
Total	14.5932	63			

SS=sum of squares, df=degrees of freedom, MS=mean square

Similar to the binary performance test area under ROC curve (AUC) used in the simulation studies, network reconstructions of real EEG data were evaluated regarding the ability to correctly reconstruct the 10 most prominent connections of the alpha2 DMN. The number of reconstructed links for each connectivity estimator is illustrated in figure 56.

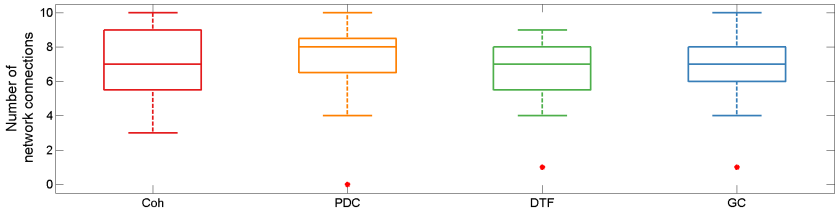

Figure 56: Boxplots of coherence (red), DTF (orange), PDC (green), and Granger causality (blue) presenting the number of correctly reconstructed network links for the 10 most prominent connections of the alpha2 DMN.

In contrast to results of Frobenius norm, boxplots for the number of correctly reconstructed network connections did not indicate significantly different performances for any of the methods. On average, all methods were able to reconstruct approximately 7 out of the 10 network links (coherence: $M = 7.063$, $SD = 2.135$; DTF: $M = 6.750$, $SD = 2.077$; PDC:

$M = 7.125$, $SD = 2.315$; Granger causality: $M = 6.750$, $SD = 2.165$). This was confirmed in a one-way ANOVA test ($F(3,60) = 0.13$, $p = 0.9538$) as displayed in table 5.4. Due to the lack of a significant result no further post-hoc tests were performed.

Table 5.4

Result of one-way ANOVA test showing the variation between connectivity estimators for the amount of correctly identified network connections.

	SS	df	MS	F	Prob > F
Methods	1.922	3	0.6406	0.13	0.9538
Residual	302.688	60	5.0448		
Total	304.609	63			

SS=sum of squares, df=degrees of freedom, MS=mean square

5.4 Discussion

This chapter investigated the ability of connectivity estimators to reconstruct a subset of posterior-to-anterior connections which are apparent in the alpha2 frequency range (10 - 13 Hz) of the DMN. Publicly available eyes-closed, resting-state data containing 16 subjects was used to transfer findings from simulated data sets onto the analysis of real electrophysiological recordings.

In summary, analysis results showed that all connectivity estimators performed well in correctly reconstructing information flow between distinct brain areas. On average, each method identified approximately 7 out of the 10 most prominent network links of the DMN for all subjects. A statistical analysis of the amount of correctly reconstructed network connections provided no evidence of significant differences between estimators. It is worth noting that the selection and design of the analytical process to reconstruct the alpha2 network was made without conducting a preliminary review of the data set. The choice of the data set was driven on the sole criterion of a resting-state experimental design including an eyes-closed condition. Given these circumstances, results of connectivity estimators have to be assessed even more positively. However, the reduced network consisted of the 10 strongest connections of the alpha2 DMN (Hillebrand et al., 2016). An advanced analysis, also incorporating information flow with weaker connectivity strength, may lead to more complex and differentiated results.

Moreover, it was demonstrated that connectivity spectra of Granger causality provided lower noise levels over the entire frequency band than other estimators. This aspect was

also verified with results of Frobenius norm indicating a significantly lower deviation from connectivity thresholds compared to coherence, DTF and PDC. Due to this integral characteristic, a visual inspection of connectivity spectra obtained from Granger causality may lead to less error-prone conclusions and implications.

Chapter 6

Conclusion

In this thesis, functional and effective connectivity methods were tested for their performance and efficiency under various conditions when applied to neural recordings. An overview of electromagnetic recording techniques was given in chapter 2.1 describing non-invasive methods to measure brain activity. The decisive parameter for reconstructing temporal changes of brain activity is the temporal and spatial resolution of a recording method. For this reason, the present work focused on the analysis and reconstruction of coherent cortical networks from EEG recordings, due to its higher temporal resolution compared to other techniques.
This chapter will discuss known limitations of the simulation model introduced in chapter 3 and present possible solutions. Further enhancements of the simulation model incorporating alternative connectivity measures and state-of-the art modelling techniques to resolve some of the restrictions depicted in the previous section are proposed. Furthermore, results of the eight simulation studies described in chapter 4 and the outcome of the analysis of real resting-state data in chapter 5 will be reviewed. Based on these considerations, advanced analyses of particular parameters affecting the reconstruction of cortical networks will be suggested.

Simulation model

After introducing state-of-the-art methods of inverse source reconstruction and brain connectivity measures in chapter 2, a simulation model to generate realistic electromagnetic recordings with a predefined underlying cortical network and known characteristics was presented in chapter 3. It proposes a modular, standardised framework that enables a transparent and comprehensible approach to generate data sets with specific properties. This has allowed us to focus on particular parameters and to reveal their impact on the accuracy and reliability of network reconstructions using different connectivity estimators.
Despite the efforts made, there are limitations of the simulation model that shall be addressed

in future research. Firstly, Gaussian white noise signals were added to simulate background brain activity. A more realistic approach would be to define time-series of noise sources with pink noise ($1/f$ noise) which has a power spectral density (PSD) that is inversely proportional to the frequency of the signal. Such a $1/f$ spectrum depicts a more accurate description of spontaneous cortical activity in humans for MEG and EEG recordings (Linkenkaer-Hansen, Nikouline, Palva, and Ilmoniemi, 2001).
The simulation provides two models to generate correlated signals for active brain areas: a multivariate-autoregressive (MVAR) approach and a model based on band-pass filtered Gaussian noise time-courses. Both types only allow a simulation of linear interactions between nodes. Enhancing the framework to support non-linear interactions will enable investigating differences between linear and non-linear connectivity estimators like mutual information (Shannon and Weaver, 1949) and transfer entropy (Schreiber, 2000). Furthermore, advanced modelling techniques may provide a way to produce more realistic brain signals and will also reflect more accurate yet simple representations of coupled neuronal populations. Possible realisations of more complex neural mass models (NMM) have been suggested by Wendling et al. (Wendling et al., 2002) and Spiegler et al. (Spiegler, Knösche, Schwab, Haueisen, and Atay, 2011). Due to the modular structure of the simulation framework, sophisticated models can easily be integrated by enhancing the respective function for the generation of time-courses for active brain areas.
Another important aspect for the generation of most realistic neurophysiological recordings is the choice of the head model, as outlined in the forward modelling and inverse source reconstruction section (section 2.2.1). The simulations carried out in chapter 4 were based on a concentric spherical 3-shell or a realistic standardised FEM head model. However, more complex, age-appropriate template models (Richards and Xie, 2015) and individual finite-element models (Wolters et al., 2006) can easily be used both to simulate and to reconstruct sources. These models allow for a more precise description of the geometries and conductivities of different head tissues (skin, skull spongiosa and compacta, cerebrospinal fluid, gray and white matter), resulting in a better quality of the forward model.
Finally, it should be pointed out that the simulation comprises a large number of functional as well as effective connectivity methods. However, there are many other estimators which have not been considered in this thesis and new methods are continuously being developed. In order to evaluate objectively the benefits and drawbacks of new estimators, it is essential to add them to the portfolio and benchmark their performance against other connectivity methods.

Simulation studies

The simulations described in chapter 4 were designed to illustrate the impact of some of the most widely discussed parameters involved in the analysis and reconstruction of cortical

networks. They cover the effect of noise at different intensities, differences in the length of data taken into account, various phase shifts between correlated signals, the impact of the regularization factor used in inverse source reconstruction, deviations in the localization of dipole positions, varying network sizes and number of sensors used during inverse source reconstruction. Each simulation revealed common effects of the examined parameter on connectivity methods but also identified systematic differences between estimators.

The initial simulation (chapter 4.1), based on the simulation framework introduced in chapter 3, focussed on the number of required iterations to obtain reliable and converging results for all connectivity estimators in subsequent simulations. It was demonstrated that connectivity methods like DTF and Granger causality require less iterations to produce exact and reliable results compared to coherence. Based on the conclusions drawn from this experiment, 100 iterations were identified as a tangible number of repetitions to obtain reproducible and consistent results. All succeeding simulation experiments build on this determined value for all parameter combinations and connectivity methods.

Simulations demonstrating the effect of SNR (chapter 4.2) indicated that increasing data quality generally led to better network reconstructions for all connectivity estimators. However, this analysis found evidence that Granger causality, DTF and PDC provide more accurate and reliable results for data with low SNR compared to connectivity spectra obtained from coherence which include a high degree of noise over the entire frequency spectrum. Overall these findings are in accordance with findings reported in previous studies (Astolfi et al., 2007, Wu et al., 2011, Silfverhuth et al., 2012, Hincapié et al., 2016). Results presented by Wu et al., 2011 lead to a consistent conclusion that Granger causality provides most reliable results and is not affected by manipulations of the SNR. Furthermore, it was demonstrated that connectivity methods can effectively benefit from an increase in SNR and tend to converge towards a limiting value. A similar pattern of results was obtained by Silfverhuth et al., 2012. In this paper, a strong effect was proven when increasing the SNR at generally lower levels (from 1 to 5 or even 10), but no statistically significant effect was obtained when increasing the SNR at higher levels (from 5 to 10). In general, this aspect of the study stresses the crucial importance of precise data acquisition to record data with optimal SNR.

Results from the experiment analysing the effect of SNR accord with the finding from simulations with varying data length as outlined in chapter 4.3. It was shown that taking more data into account increased the accuracy of coherence and imaginary part of coherency only up to a certain limit depending on the SNR of the data set. A higher precision was only possible with higher quality data. Extensive results carried out indicate that connectivity spectra of all estimators, coherence in particular, show a significant decrease in variation of noise with higher data length for simulated as well as for reconstructed networks. DTF, PDC and Granger causality are not affected by poor SNR values to that extent. These basic

findings are consistent with previous research (Astolfi et al., 2007, Fraschini et al., 2016). Moreover, the study by Fraschini et al., 2016 indicated that shorter epochs not only led to a decreased efficiency of connectivity methods but also show less clear (more blurred) connectivity patterns.

In addition, simulations were carried out to examine parameters directly connected to inverse source localization and the reconstruction of temporal activity for active brain regions. A detailed and comprehensive description of EEG source imaging techniques and pitfalls can be found in the review papers by Grech et al., 2008 and Michel and Brunet, 2019.

Chapter 4.6 investigated the effect of regularization on the performance of connectivity methods. In general, regularization is necessary to stabilize the inverse solution of the ill-posed problem. However, over-regularization leads to spatial blurring and may mask activity from weaker signals (van Vliet, Liljeström, Aro, Salmelin, and Kujala, 2018). In the experiment, it was demonstrated that the degree of regularization required for accurate network reconstructions depends on the quality of recordings. Results obtained in this simulation tie well with previous studies analysing the effect of regularization on source estimation (Haufe et al., 2011, Hincapié et al., 2016), but go beyond previous reports, disclosing the effect of regularization on network reconstructions. An increase in regularization resulted in a higher accuracy up to a specific threshold. Further increase led to a decline in network reconstruction. It should be noted that DTF, PDC and Granger causality particularly robust and insensitive to inadequate values of regularization and only dropped in performance in case of excessive regularization combined with high SNR data.

Another simulation with focus on inverse source imaging examined the dependency between source localization errors and network reconstructions (chapter 4.7). From this simulation it was confirmed that larger localization errors deteriorate the variance and reliability of connectivity methods. Significantly decreased performance could be observed for coherence. DTF, PDC and Granger causality showed no significantly difference for larger errors, with Granger causality outperforming all other methods. Furthermore, this study showed the relationship between localization errors and regularization and demonstrated that results suffer from an incorrect or not properly optimized regularization. This effect of source localization on connectivity methods has previously been assessed only to a very limited extent. Recently, Mahjoory et al. (Mahjoory et al., 2017) presented a comprehensive overview of the effect of source reconstruction parameters on functional and effective source connectivity estimates. This study compares several localization methods from various toolboxes regarding the consistency between source reconstruction parameters. However, a more detailed analysis regarding errors in source localization is not taken into account. Collectively, results from Mahjoory et al. and this experiment provide additional information for researchers and highlight promising aspects that future research could continue to explore.

The simulation on number of active network nodes (section 4.8) revealed that an increase in network size complicates a reliable and accurate identification of relationships between nodes. It was shown that a larger number of sources, including a higher number of possible connections may impede a methods ability to correctly identify existing links between nodes. In order to maintain a comparability between the simulated networks with different numbers of nodes, the ratio of connected nodes to possible connections was kept constant. Superior results are seen by Granger causality, DTF and PDC, which produced reliable results in reconstructing simulated links and only revealed minor inconsistencies distinguishing direct and indirect connections. Overall, connectivity spectra of Granger causality contained a low noise level over the entire frequency band, resulting in a straight-forward identification of network links. When comparing our results to those of Wu et al. (Wu et al., 2011), it must be pointed out the performance comparison of connectivity methods in this paper did not take forward modelling and inverse source reconstruction into account. However, findings from this study are directly in line with results from this simulation. More recently, Farahibozorg et al. (Farahibozorg et al., 2018) looked at the sensitivity of parcellation methods for network consisting of 3, 5, 10 and 15 nodes and varying number of connections. It was shown that an increase of both, network size and network complexity (number of connections between active sources) lead to a deterioration of network reconstruction. The effect of network complexity was not outlined in section 4.8. However, future studies should aim to replicate and enhance the results based on these findings and to examine the effect of network complexity on the performance of a variety of connectivity estimators.

The final simulation (section 4.8) revealed that an increase in network size complicates a reliable and accurate identification of relationships between nodes. Therefore, simulated data sets with 16 to 256 numbers of EEG sensors were analysed. The evaluation of this data leads to the conclusion that the number of sensors which are taken into account during source reconstruction is of vital importance for network reconstructions. Overall, results demonstrate an improvement in accuracy and precision of network reconstructions with an increase of number of sensors for all estimators. Increasing the number of sensors at a relatively low level (16 to 31 sensors) led to a strong improvement in network reconstruction. However, a further increase from 64 to 128 or 256 sensors only provided minimal improvements. These results are consistent with previous studies that indicated more accurate and consistent results when increasing the number of sensors for localization of cortical activity (Lantz et al., 2003, Song et al., 2015) or for reconstruction of functional networks (Hassan et al., 2014).

One of the objectives of this work was to explore the effect of parameters on connectivity methods. The simulation studies carried out revealed dependencies and interrelationships between variables future studies can benefit from. Nonetheless, there are still unanswered questions which need to be addressed in future research. In addition to the examination

of source localization errors, further simulations should analyse the effect of deviations in reconstructed dipole orientations. In this context, it is to be expected that a difference between the simulated and reconstructed orientation may have an even stronger influence on connectivity estimators than erroneous dipole localizations. Inverse source reconstruction in general is a vitally important element for subsequent connectivity analysis. In the studies outlined in the introductory overview and comparison of simulation experiments (chapter 1.2), other approaches to estimate active brain regions and to compute their temporal activity were presented. Connectivity estimation based on results from LCMV beamforming (Colclough et al., 2015, Anzolin et al., 2019) and MNE (Farahibozorg et al., 2018) are among the most common used distributed source reconstruction methods and should therefore be included in future research. Furthermore, a comparison between distributed and discrete source reconstruction approaches, as used in this thesis, would be helpful to unravel any differences. However, a comprehensive comparison study of source analysis methods and their implications and influence on connectivity estimators remains briefly addressed in the literature. Therefore, future research is required to strategically examine the effect of different source reconstruction approaches on connectivity estimators.

An apparent simplification of the studies is the number of sources modelled by the sources montages, as well as their positions and orientations which matches the simulated active regions in all but one of the experiments. This high degree of overlap cannot be ensured when analysing real MEG or EEG data sets. Nonetheless, it reduces the influence of source reconstruction parameters and allows an undistorted examination of other factors that are involved in the entire processing pipeline. In order to make it easier to generalize results and transfer insights onto other data sets, this approach can be enhanced by e.g. creating more generic source montages based on histological brain atlases.

Moreover, a comparison between network reconstructions derived from EEG and MEG data may provide an interesting research question for subsequent experiments. This work was mainly dedicated to the analysis of EEG data. Therefore, more research is needed to recognise similarities and differences between those functional neuroimaging techniques.

Real EEG data analysis

The aim of chapter 5 was to transfer knowledge and implications gained from the simulations studies onto the evaluation of real electrophysiological recordings. Resting-state EEG recordings were analysed to illustrate the presence of a network with dominant posterior-to-anterior information flow in the alpha frequency band, which has been outlined in previous studies (Hillebrand et al., 2016).

The comparison of network reconstructions using various connectivity estimators did not indicate any significant differences in the ability of each method to correctly identify information flow between distinct cortical regions. In addition, real EEG data analysis

confirmed findings from simulated data that Granger causality tends to produce connectivity spectra with lower noise levels over the entire frequency band compared to coherence, DTF and PDC. This is particularly beneficial in the case of a visual inspection of spectra, leading to less error-prone evaluations and interpretations of results.

On the basis of the knowledge and experience gained during this PhD, a software application called BESA Connectivity 1.0 (available from: https://www.besa.de/products/) was being developed at BESA GmbH. This program includes multiple algorithms to perform time-frequency analysis and connectivity estimation for EEG/MEG data. For time-frequency decomposition of signals, two approaches are provided: complex demodulation (Papp and Ktonas, 1977) and wavelet analysis (Morlet and complex Mexican Hat wavelet). Subsequently, various connectivity measures like coherence, imaginary part of coherency, DTF, PDC or Granger causality may be computed to detect information flow between distinct network nodes. Screenshots of the application, illustrating results of time-frequency decomposition and connectivity estimation on sensor and source level, are shown in figure 57 in the appendix of this thesis.

In conclusion, results and findings of this thesis delivered guidelines and recommendations that allow researchers to choose appropriate connectivity estimators. Furthermore, the present work revealed dependencies between the accuracy of network reconstructions and properties of the neurophysiological data set to be processed or other parameters involved in the computational analysis. Notably, the method that has proven most effective for a majority of the different simulations was Granger causality. It produced reliable and consistent results even for short recordings or qualitatively inferior data. Beyond that, the results presented in this work provide additional insights on the performance of various connectivity measures, researchers and future studies will benefit from.

Appendix

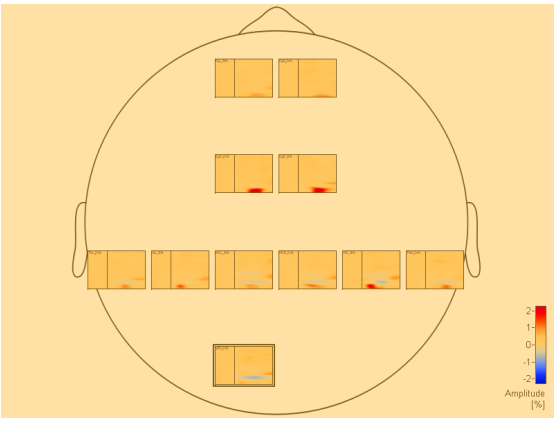

(a) Topographic representation of a time-frequency decomposition calculated using Complex Demodulation.

(b) Connectivity matrix showing imaginary part of coherency for a source montage including 11 network nodes.

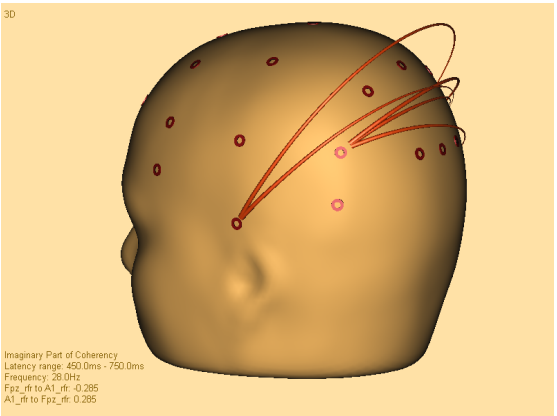

(c) 3D visualization (back-left view) of imaginary part of coherency on sensor level. EEG sensors are displayed as red discs.

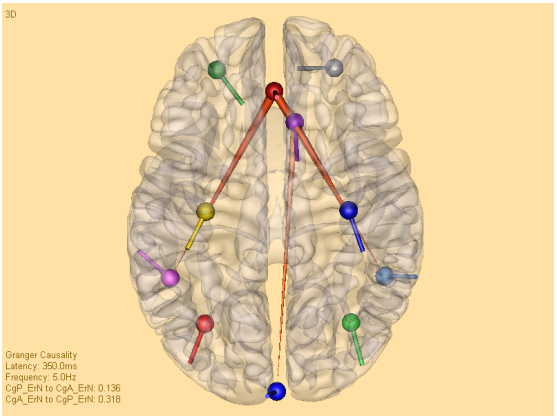

(d) 3D visualization (top view) of Granger causality on source level. Active brain areas are represented by (colour-coded) dipoles.

Figure 57: Screenshots of BESA Connectivity 1.0.

Table A1

Overview on simulation studies.

Study	Model type	Source reconstruction	Connectivity methods	Statistical evaluation	Parameters
Ursino et al. (2007)	NMM	LAURA, ROIs three-shell BEM		n.a.	
Astolfi et al. (2007)	MVAR	LAURA BEM	DTF, dDTF, PDC	ANOVA, Frobenius norm	SNR, Data length
Florin et al. (2010)	MVAR	n.a.	DTF, dDTF, PDC, sPDC	MW U Test, Bonferroni	Effect of filtering
Wu et al. (2011)	MVAR	n.a.	DTF, dDTF, ffDTF, PDC, sPDC, GC	n.a.	Network size, SNR, AR model order
Silfverhuth et al. (2012)	MVAR	n.a.	COR, COH, PSI, TE, DTF, PDC	Chi-Square tests	SNR, Sampling rate MVAR Model order
Drakesmith et al. (2012)	bilateral sources, 33Hz sine waves		DICS	TPR, FPR, Log ROC, AUC	EEG vs. MEG, CSD sampling
Haufe et al. (2013)	AR	MNE, LCMV BEM	PSI, GC, PDC	F-test	
Farahibozorg et al. (2018)	Sine waves	MNE BEM	COH, iCOH	TPR, FPR, Permutation testing	
Anzolin et al. (2019)	MVAR	LCMV, eLORETA New York Head	MVAR GC, TRGC	FPR, FNR, AUC, ANOVA	SNR, Dipole positions, Inverse methods

Table A2

Coordinates and orientations (in Talairach coordinate system) for a brain network consisting of 4 *nodes used throughout several simulations in this work.*

		Coordinates			Orientations		
Label	Type	x	y	z	x	y	z
1	Dipole	−35.89	−48.27	1.09	−0.58	−0.80	−0.07
2	Dipole	−34.78	24.98	8.19	−0.63	0.77	0.07
3	Dipole	35.89	−48.27	1.09	0.66	−0.74	−0.07
4	Dipole	34.78	24.98	8.19	0.69	0.71	0.06

Table A3

Coordinates and orientations (in Talairach coordinate system) for a brain network consisting of 6 *nodes used in simulation VII (chapter 4.8).*

		Coordinates			Orientations		
Label	Type	x	y	z	x	y	z
1	Dipole	−35.90	−66.97	−0.73	−0.42	−0.90	−0.08
2	Dipole	−36.15	34.37	9.14	−0.80	0.59	0.05
3	Dipole	35.77	−66.78	−0.73	0.42	−0.90	−0.08
4	Dipole	35.90	34.02	9.14	0.80	0.59	0.05
5	Dipole	−47.51	−13.90	14.78	−0.26	−0.45	−0.85
6	Dipole	47.51	−13.90	14.78	0.26	−0.45	−0.85

Table A4

Coordinates and orientations (in Talairach coordinate system) for a brain network consisting of 8 *nodes used in simulation VII (chapter 4.8).*

		Coordinates			Orientations		
Label	Type	x	y	z	x	y	z
1	Dipole	−35.76	−67.12	−0.73	−0.42	−0.90	−0.08
2	Dipole	−35.76	34.78	9.14	−0.79	0.60	0.05
3	Dipole	35.76	−67.12	−0.73	0.42	−0.90	−0.08
4	Dipole	35.76	34.78	9.14	0.79	0.60	0.05
5	Dipole	−47.51	−13.90	14.78	−0.27	−0.45	−0.84
6	Dipole	47.51	−13.90	14.78	0.27	−0.45	−0.84
7	Dipole	0.00	−71.17	35.13	0.00	−0.80	0.59
8	Dipole	0.00	30.77	45.62	0.00	0.90	0.42

Table A5

Coordinates and orientations (in Talairach coordinate system) for a brain network consisting of 10 *nodes used in simulation VII (chapter 4.8).*

		Coordinates			Orientations		
Label	Type	x	y	z	x	y	z
1	Dipole	−35.76	−67.13	−0.73	−0.42	−0.90	−0.08
2	Dipole	−35.76	34.78	9.14	−0.80	0.59	0.05
3	Dipole	35.76	−67.13	−0.73	0.42	−0.90	−0.08
4	Dipole	35.76	34.78	9.14	0.78	0.61	0.05
5	Dipole	−47.51	−13.90	14.78	−0.25	−0.46	−0.84
6	Dipole	47.51	−13.90	14.78	0.27	−0.44	−0.85
7	Dipole	0.00	30.73	45.01	0.00	0.76	0.63
8	Dipole	0.00	−71.17	35.13	0.00	−0.88	0.47
9	Dipole	−25.41	−21.32	47.22	−0.71	−0.11	0.69
10	Dipole	25.41	−21.32	47.22	0.71	−0.04	0.70

Table A6

*Coordinates and orientations (in Talairach coordinate system) of network nodes involved in the alpha*2 *DMN including* 3 *additional noise sources.*

		Coordinates			Orientations		
Label	Type	x	y	z	x	y	z
ACG right	Dipole	5.97	31.32	21.52	0.00	−0.95	−0.29
CAL left	Dipole	−8.87	−75.47	2.80	0.00	0.99	−0.03
CAL right	Dipole	12.48	−70.90	6.23	0.00	0.99	−0.13
CUN left	Dipole	−8.09	−78.82	21.20	0.00	0.97	−0.22
CUN right	Dipole	9.96	−78.05	22.49	0.00	0.97	−0.21
IFGtriang right	Dipole	44.44	24.90	20.07	−0.77	−0.50	−0.36
SFGmed left	Dipole	−6.68	41.38	35.83	0.00	−0.92	−0.38
SFGmed right	Dipole	6.28	42.75	35.76	0.00	−0.94	−0.31
Noise left	RS	−55.83	−10.98	−2.87	0.00	0.00	0.00
Noise right	RS	55.83	−10.98	−2.87	0.00	0.00	0.00
Noise central	RS	0.00	−22.87	60.98	0.00	0.00	0.00

RS = regional source

Table A7

Coordinates (in Talairach coordinate system) of noise sources.

		Coordinates		
Label	Type	x	y	z
TAL	RS	−50.66	13.52	−5.71
A1L	RS	−42.95	−12.95	−27.00
TPL	RS	−50.66	−43.60	−11.25
Fp1L	RS	−23.65	48.47	4.09
FL	RS	−33.82	32.70	25.80
FC1L	RS	−20.98	4.74	54.29
FC5L	RS	−49.43	5.79	22.18
CL	RS	−39.59	−20.86	43.12
CP1L	RS	−20.98	−48.40	49.13
CP5L	RS	−49.43	−42.26	17.52
PL	RS	−33.82	−69.40	15.90
O1L	RS	−23.65	−79.99	−8.35
FpM	RS	0.00	52.65	17.35
FM	RS	0.00	30.24	47.30
CM	RS	0.00	−22.87	60.98
PM	RS	0.00	−71.79	37.41
OpM	RS	0.00	−87.03	3.81
Fp2R	RS	23.65	48.47	4.09
FR	RS	33.82	32.70	25.80
FC2R	RS	20.98	4.74	54.29
FC6R	RS	49.43	5.79	22.18
CR	RS	39.59	−20.86	43.12
CP2R	RS	20.98	−48.40	49.13
CP6R	RS	49.43	−42.26	17.52
PR	RS	33.82	−69.40	15.90
O2R	RS	23.65	−79.99	−8.35
TAR	RS	50.66	13.52	−5.71
A2R	RS	42.95	−12.95	−27.00
TPR	RS	50.66	−43.60	−11.25

RS = regional source

Table A8

Electrode labels and coordinates for a sensor configuration consisting of 16 *electrodes. Coordinates are given in head coordinate system.*

	Coordinates [mm]		
Electrode label	x	y	z
Ele_FP1	−26.30	80.80	33.00
Ele_FP2	26.30	80.80	33.00
Ele_F4	46.30	57.20	78.40
Ele_Fz	0.00	61.10	95.00
Ele_F3	−46.30	57.20	78.40
Ele_T7	−84.90	0.00	33.00
Ele_C3	−61.10	0.00	95.00
Ele_Cz	0.00	0.00	120.90
Ele_C4	61.10	0.00	95.00
Ele_T8	84.90	0.00	33.00
Ele_P4	46.30	−57.20	78.40
Ele_Pz	0.00	−61.10	95.00
Ele_P3	−46.30	−57.20	78.40
Ele_O1	−26.30	−80.80	33.00
Ele_Oz	0.00	−84.90	33.00
Ele_O2	26.30	−80.80	33.00

Table A9

Electrode labels and coordinates for a sensor configuration consisting of 31 *electrodes. Coordinates are given in head coordinate system.*

	Coordinates [mm]		
Electrode label	x	y	z
Ele_FP1	−26.30	80.80	33.00
Ele_FP2	26.30	80.80	33.00
Ele_F3	−46.30	57.20	78.40
Ele_F4	46.30	57.20	78.40
Ele_C3	−61.10	0.00	95.00
Ele_C4	61.10	0.00	95.00
Ele_P3	−46.30	−57.20	78.40
Ele_P4	46.30	−57.20	78.40
Ele_O1	−26.30	−80.80	33.00
Ele_O2	26.30	−80.80	33.00
Ele_A1	−66.90	−3.50	−16.40
Ele_A2	66.90	−3.50	−16.40
Ele_F7	−68.70	49.90	33.00
Ele_F8	68.70	49.90	33.00
Ele_T7	−84.90	0.00	33.00
Ele_T8	84.90	0.00	33.00
Ele_P7	−68.70	−49.90	33.00
Ele_P8	68.70	−49.90	33.00
Ele_Fz	0.00	61.10	95.00
Ele_Pz	0.00	−61.10	95.00
Ele_P9	−62.30	−45.30	0.00
Ele_P10	62.30	−45.30	0.00
Ele_FC1	−31.90	31.90	108.00
Ele_FC2	31.90	31.90	108.00
Ele_FC5	−75.00	28.80	63.60
Ele_FC6	75.00	28.80	63.60
Ele_T1	−76.00	27.60	9.70
Ele_T2	76.00	27.60	9.70
Ele_CP5	−75.00	−28.80	63.60
Ele_CP6	75.00	−28.80	63.60
Ele_Cz	0.00	0.00	120.90

Table A10

Electrode labels and coordinates for a sensor configuration consisting of 64 *electrodes. Coordinates are given in head coordinate system.*

	Coordinates [mm]				Coordinates [mm]		
Electrode label	x	y	z	Electrode label	x	y	z
Ele_FP1	−26.30	80.80	33.00	Ele_FPz	0.00	84.90	33.00
Ele_AF7	−49.90	68.70	33.00	Ele_FP2	26.30	80.80	33.00
Ele_AF3	−34.50	74.10	59.40	Ele_AF8	49.90	68.70	33.00
Ele_F1	−24.40	60.40	90.60	Ele_AF4	34.50	74.10	59.40
Ele_F3	−46.30	57.20	78.40	Ele_AFz	0.00	79.40	66.40
Ele_F5	−62.00	53.90	57.90	Ele_Fz	0.00	61.10	95.00
Ele_F7	−68.70	49.90	33.00	Ele_F2	24.40	60.40	90.60
Ele_FT7	−80.80	26.30	33.00	Ele_F4	46.30	57.20	78.40
Ele_FC5	−75.50	29.00	62.20	Ele_F6	62.00	53.90	57.90
Ele_FC3	−57.50	30.60	90.60	Ele_F8	68.70	49.90	33.00
Ele_FC1	−31.90	31.90	108.00	Ele_FT8	80.80	26.30	33.00
Ele_C1	−33.20	0.00	114.20	Ele_FC6	75.50	29.00	62.20
Ele_C3	−61.10	0.00	95.00	Ele_FC4	57.50	30.60	90.60
Ele_C5	−79.40	0.00	66.40	Ele_FC2	31.90	31.90	108.00
Ele_T7	−84.90	0.00	33.00	Ele_FCz	0.00	33.20	114.20
Ele_TP7	−80.80	−26.30	33.00	Ele_Cz	0.00	0.00	120.90
Ele_CP5	−75.50	−29.00	62.20	Ele_C2	33.20	0.00	114.20
Ele_CP3	−57.50	−30.60	90.60	Ele_C4	61.10	0.00	95.00
Ele_CP1	−31.90	−31.90	108.00	Ele_C6	79.40	0.00	66.40
Ele_P1	−24.40	−60.40	90.60	Ele_T8	84.90	0.00	33.00
Ele_P3	−46.30	−57.20	78.40	Ele_TP8	80.80	−26.30	33.00
Ele_P5	−62.00	−53.90	57.90	Ele_CP6	75.50	−29.00	62.20
Ele_P7	−68.70	−49.90	33.00	Ele_CP4	57.50	−30.60	90.60
Ele_P9	−59.00	−49.50	0.00	Ele_CP2	31.90	−31.90	108.00
Ele_PO7	−49.90	−68.70	33.00	Ele_P2	24.40	−60.40	90.60
Ele_PO3	−34.50	−74.10	59.40	Ele_P4	46.30	−57.20	78.40
Ele_O1	−26.30	−80.80	33.00	Ele_P6	62.00	−53.90	57.90
Ele_Iz	0.00	−77.00	0.00	Ele_P8	68.70	−49.90	33.00
Ele_Oz	0.00	−84.90	33.00	Ele_P10	59.00	−49.50	0.00
Ele_POz	0.00	−79.40	66.40	Ele_PO8	49.90	−68.70	33.00
Ele_Pz	0.00	−61.10	95.00	Ele_PO4	34.50	−74.10	59.40
Ele_CPz	0.00	−33.20	114.20	Ele_O2	26.30	−80.80	33.00

Table A11

Electrode labels and coordinates for a sensor configuration consisting of 72 *electrodes (*67 *scalp channels and* 5 *polygraphic channels). Positions of sensors are given in spherical coordinates, defined in degrees by the azimuth and the elevation angle.*

	Coordinates [°]			Coordinates [°]	
Electrode label	Azimuth	Elevation	Electrode label	Azimuth	Elevation
FP1	−92.00	−72.00	AFz	69.00	90.00
AF7	−92.00	−52.00	Fz	46.00	90.00
AF3	−74.00	−67.00	F2	50.00	68.00
F1	−50.00	−68.00	F4	60.00	51.00
F3	−60.00	−51.00	F6	75.00	41.00
F5	−75.00	−41.00	F8	92.00	36.00
F7	−92.00	−36.00	FT8	92.00	18.00
FT7	−92.00	−18.00	FC6	71.00	21.00
FC5	−71.00	−21.00	FC4	50.00	28.00
FC3	−50.00	−28.00	FC2	32.00	45.00
FC1	−32.00	−45.00	FCz	23.00	90.00
C1	−23.00	0.00	Cz	0.00	0.00
C3	−46.00	0.00	C2	23.00	0.00
C5	−69.00	0.00	C4	46.00	0.00
T7	−92.00	0.00	C6	69.00	0.00
TP7	−92.00	18.00	T8	92.00	0.00
CP5	−71.00	21.00	TP8	92.00	−18.00
CP3	−50.00	28.00	CP6	71.00	−21.00
CP1	−32.00	45.00	CP4	50.00	−28.00
P1	−50.00	68.00	CP2	32.00	−45.00
P3	−60.00	51.00	P2	50.00	−68.00
P5	−75.00	41.00	P4	60.00	−51.00
P7	−92.00	36.00	P6	75.00	−41.00
P9	−115.00	36.00	P8	92.00	−36.00
PO7	−92.00	54.00	P10	115.00	−36.00
PO3	−74.00	67.00	PO8	92.00	−54.00
O1	−92.00	72.00	PO4	74.00	−67.00
Iz	115.00	−90.00	O2	92.00	−72.00
Oz	92.00	−90.00	M1	−120.00	25.00
POz	69.00	−90.00	M2	120.00	−25.00
Pz	46.00	−90.00	Nz	112.00	90.00
CPz	23.00	−90.00	LVEOG	*n.a.*	*n.a.*
FPz	92.00	90.00	RVEOG	*n.a.*	*n.a.*
FP2	92.00	72.00	LHEOG	*n.a.*	*n.a.*
AF8	92.00	52.00	RHEOG	*n.a.*	*n.a.*
AF4	74.00	67.00	NFPz	*n.a.*	*n.a.*

Bibliography

Akaike, H. (1974). A new look at the statistical model identification. *IEEE Transactions on Automatic Control*, *19*(6), 716–723.

Akalin-Acar, Z., & Gençer, N. G. (2004). An advanced boundary element method (bem) implementation for the forward problem of electromagnetic source imaging. *Physics in Medicine and Biology*, *49*(21), 5011–5028.

Amunts, K., Hawrylycz, M. J., Van Essen, D. C., Van Horn, J. D., Harel, N., Poline, J.-B., De Martino, F., Bjaalie, J. G., Dehaene-Lambertz, G., Dehaene, S., Valdes-Sosa, P., Thirion, B., Zilles, K., Hill, S. L., Abrams, M. B., Tass, P. A., Vanduffel, W., C., E. A., & Eickhoff, S. B. (2014). Interoperable atlases of the human brain. *NeuroImage*, *99*, 525–532.

Anzolin, A., Presti, P., Van De Steen, F., Astolfi, L., Haufe, S., & Marinazzo, D. (2019). Quantifying the effect of demixing approaches on directed connectivity estimated between reconstructed eeg sources. *Brain Topography*, *32*, 655–674.

Astolfi, L., Cincotti, F., Mattia, D., Marciani, M. G., Baccalá, L. A., de Vico Falliani, F., Salinari, S., Ursino, M., Zavaglia, M., & Babiloni, F. (2006). Assessing cortical functional connectivity by partial directed coherence: Simulations and application to real data. *IEEE Transactions on Biomedical Engineering*, *53*(9), 1802–1812.

Astolfi, L., Cincotti, F., Mattia, D., Marciani, M. G., Baccalá, L. A., de Vico Falliani, F., Salinari, S., Ursino, M., Zavaglia, M., Ding, L., Edgar, J. C., Miller, G. A., He, B., & Babiloni, F. (2007). Comparison of different cortical connectivity estimators for high-resolution eeg recordings. *Human Brain Mapping*, *28*(2), 143–157.

Babiloni, F., Cincotti, F., Babiloni, C., Carducci, F., Mattia, D., Astolfi, L., Basilisco, A., Rossini, P. M., Ding, L., Ni, Y., Cheng, J., Christine, K., Sweeney, J., & He, B. (2005). Estimation of the cortical functional connectivity with the multimodal integration of high-resolution eeg and fmri data by directed transfer function. *NeuroImage*, *24*(1), 118–131.

Baccalá, L. A., & Sameshima, K. (2001). Partial directed coherence: A new concept in neural structure determination. *Biological Cybernetics*, *84*(6), 463–474.

Baillet, S., Mosher, J., & Leahy, R. (2001). Electromagnetic brain mapping. *IEEE Signal Processing Magazine*, *18*(6), 14–30.

Bastiaansen, M. C. M., Böcker, K. B. E., Brunia, C. H. M., de Munck, J. C., & Spekreijse, H. (2001). Event-related desynchronization during anticipatory attention for an upcoming stimulus: A comparative eeg/meg study. *Clinical Neurophysiology*, *112*(2), 393–403.

Bastos, A. M., & Schoffelen, J.-M. (2016). A tutorial review of functional connectivity analysis methods and their interpretational pitfalls. *Frontiers in Systems Neuroscience*, *9*(Pt 2), 413.

Beckmann, C. F., DeLuca, M., Devlin, J. T., & Smith, S. M. (2005). Investigations into resting-state connectivity using independent component analysis. *Philosophical Transactions of the Royal Society B: Biological Sciences*, *360*(1457), 1001–1013.

Berg, P., & Scherg, M. (1994). A fast method for forward computation of multiple-shell spherical head models. *Electroencephalography and Clinical Neurophysiology*, *90*(1), 58–64.

Berger, H. (1929). Über das elektrenkephalogramm des menschen. *Archiv für Psychiatrie und Nervenkrankheiten*, *87*(1), 527–570.

Biswal, B., Yetkin, F. Z., Haughton, V. M., & Hyde, J. S. (1995). Functional connectivity in the motor cortex of resting human brain using echo-planar mri. *Magnetic Resonance in Medicine*, *34*(4), 537–541.

Blinowska, K. J. (2011). Review of the methods of determination of directed connectivity from multichannel data. *Medical & Biological Engineering & Computing*, *49*(5), 521–529.

Bonita, J. D., Ambolode, L. C. C., Rosenberg, B. M., Cellucci, C. J., Watanabe, T. A. A., Rapp, P. E., & Albano, A. M. (2014). Time domain measures of inter-channel eeg correlations: A comparison of linear, nonparametric and nonlinear measures. *Cognitive Neurodynamics*, *8*(1), 1–15.

Büchel, C., & Friston, K. J. (1997). Modulation of connectivity in visual pathways by attention: Cortical interactions evaluated with structural equation modelling and fmri. *Cerebral Cortex (New York, N.Y.: 1991)*, *7*(8), 768–778.

Bunge, S., & Kahn, I. (2009). Cognition: An overview of neuroimaging techniques. In *Encyclopedia of neuroscience* (pp. 1063–1067).

Caramazza, A. (1992). Is cognitive neuropsychology possible? *Journal of Cognitive Neuroscience*, *4*(1), 80–95.

Chauveau, N., Franceries, X., Doyon, B., Rigaud, B., Morucci, J. P., & Celsis, P. (2004). Effects of skull thickness, anisotropy, and inhomogeneity on forward eeg/erp computations using a spherical three-dimensional resistor mesh model. *Human Brain Mapping*, *21*(2), 86–97.

Chu, C. J., Kramer, M. A., Pathmanathan, J., Bianchi, M. T., Westover, M. B., Wizon, L., & Cash, S. S. (2012). Emergence of stable functional networks in long-term human electroencephalography. *Journal of Neuroscience*, *32*(8), 2703–2713.

Clark, R. D., & Webster-Clark, D. J. (2008). Managing bias in roc curves. *Journal of Computer-Aided Molecular Design*, *22*(3–4), 141–146.

Cohen, D. (1968). Magnetoencephalography: Evidence of magnetic fields produced by alpha-rhythm currents. *Science (New York, N.Y.) 161*(3843), 784–786.

Colclough, G., Brookes, M., Smith, S., & Woolrich, M. (2015). A symmetric multivariate leakage correction for meg connectomes. *NeuroImage*, *117*, 439–448.

de Pasquale, F., Della Penna, S., Snyder, A. Z., Lewis, C., Mantini, D., Marzetti, L., Belardinelli, P., Ciancetta, L., Pizzella, V., Romani, G. L., & Corbetta, M. (2010). Temporal dynamics of spontaneous meg activity in brain networks. *Proceedings of the National Academy of Sciences*, *107*(13), 6040–6045.

Della Penna, S., Torquati, K., Pizzella, V., Babiloni, C., Franciotti, R., Rossini, P., & Romani, G. (2004). Temporal dynamics of alpha and beta rhythms in human si and sii after galvanic median nerve stimulation. a meg study. *NeuroImage*, *22*(4), 1438–1446.

Desikan, R. S., Ségonne, F., Fischl, B., Quinn, B. T., Dickerson, B. C., Blacker, D., Buckner, R. L., Dale, A. M., Maguire, R. P., Hyman, B. T., & et al. (2006). An automated labeling system for subdividing the human cerebral cortex on mri scans into gyral based regions of interest. *NeuroImage*, *31*(3), 968–980.

Destrieux, C., Fischl, B., Dale, A., & Halgren, E. (2010). Automatic parcellation of human cortical gyri and sulci using standard anatomical nomenclature. *NeuroImage*, *53*(1), 1–15.

Dhamala, M., Rangarajan, G., & Ding, M. (2008). Estimating granger causality from fourier and wavelet transforms of time series data. *Physical Review Letters*, *100*(1).

Ding, M., Bressler, S. L., Yang, W., & Liang, H. (2000). Short-window spectral analysis of cortical event-related potentials by adaptive multivariate autoregressive modeling: Data preprocessing, model validation, and variability assessment. *Biological Cybernetics*, *83*(1), 35–45.

Ding, M., Chen, Y., & Bressler, S. L. (2006). Granger causality: Basic theory and application to neuroscience. *arXiv:q-bio/0608035*. arXiv: q-bio/0608035.

Drakesmith, M. (2012). *Reconstructing coherent cortical networks from electroencephalography and magnetoencephalography recordings* (Doctoral dissertation, University of Manchester, Manchester).

Duncan, J., & Owen, A. M. (2000). Common regions of the human frontal lobe recruited by diverse cognitive demands. *Trends in Neurosciences*, *23*(10), 475–483.

Eickhoff, S. B., Paus, T., Caspers, S., Grosbras, M.-H., Evans, A. C., Zilles, K., & Amunts, K. (2007). Assignment of functional activations to probabilistic cytoarchitectonic areas revisited. *NeuroImage*, *36*(3), 511–521.

Eickhoff, S. B., Thirion, B., Varoquaux, G., & Bzdok, D. (2015). Connectivity-based parcellation: Critique and implications: Connectivity-based parcellation. *Human Brain Mapping*, *36*(12), 4771–4792.

Fan, L., Li, H., Zhuo, J., Zhang, Y., Wang, J., Chen, L., Yang, Z., Chu, C., Xie, S., Laird, A. R., Fox, P. T., Eickhoff, S. B., Yu, C., & Jiang, T. (2016). The human brainnetome atlas: A new brain atlas based on connectional architecture. *Cerebral Cortex*, *26*(8), 3508–3526.

Farahibozorg, S.-R., Henson, R. N., & Hauk, O. (2018). Adaptive cortical parcellations for source reconstructed eeg/meg connectomes. *NeuroImage*, *169*, 23–45.

Fischl, B., van der Kouwe, A., Destrieux, C., Halgren, E., Ségonne, F., Salat, D. H., Busa, E., Seidman, L. J., Goldstein, J., Kennedy, D., V., C., N., M., B., R., & M., D. A. (2004). Automatically parcellating the human cerebral cortex. *Cerebral Cortex (New York, N.Y.: 1991)*, *14*, 11–22.

Florin, E., & Baillet, S. (2015). The brain's resting-state activity is shaped by synchronized cross-frequency coupling of neural oscillations. *NeuroImage*, *111*, 26–35.

Florin, E., Gross, J., Pfeifer, J., Fink, G. R., & Timmermann, L. (2010). The effect of filtering on granger causality based multivariate causality measures. *NeuroImage*, *50*(2), 577–588.

Fonov, V., Evans, A. C., Botteron, K., Almli, C. R., McKinstry, R. C., & Collins, D. L. (2011). Unbiased average age-appropriate atlases for pediatric studies. *NeuroImage*, *54*(1), 313–327.

Fonov, V., Evans, A., McKinstry, R., Almli, C., & Collins, D. (2009). Unbiased nonlinear average age-appropriate brain templates from birth to adulthood. *NeuroImage*, *47*, S102.

Franaszczuk, P. J., Blinowska, K. J., & Kowalczyk, M. (1985). The application of parametric multichannel spectral estimates in the study of electrical brain activity. *Biological Cybernetics*, *51*(4), 239–247.

Frank, E. (1952). Electric potential produced by two point current sources in a homogeneous conducting sphere. *Journal of Applied Physics*, *23*(11), 1225–1228.

Fraschini, M., Demuru, M., Crobe, A., Marrosu, F., Stam, C. J., & Hillebrand, A. (2016). The effect of epoch length on estimated eeg functional connectivity and brain network organisation. *Journal of Neural Engineering*, *13*(3).

Friston, K. J. (1994). Functional and effective connectivity in neuroimaging: A synthesis. *Human Brain Mapping*, *2*(1–2), 56–78.

Fuchs, M., Kastner, J., Wagner, M., Hawes, S., & Ebersole, J. S. (2002). A standardized boundary element method volume conductor model. *Clinical Neurophysiology: Official Journal of the International Federation of Clinical Neurophysiology*, *113*(5), 702–712.

Fuchs, M., Wagner, M., & Kastner, J. (2001). Boundary element method volume conductor models for eeg source reconstruction. *Clinical Neurophysiology*, *112*(8), 1400–1407.

Geselowitz, D. B. (1967). On bioelectric potentials in an inhomogeneous volume conductor. *Biophysical Journal*, *7*(1), 1–11.

Geweke, J. (1982). Measurement of linear dependence and feedback between multiple time series. *Journal of the American Statistical Association*, *77*(378), 304.

Goldberg, D. E. (1989). *Genetic algorithms in search, optimization and machine learning* (1st ed.). Addison-Wesley Longman Publishing Co., Inc.

Gong, G., He, Y., Concha, L., Lebel, C., Gross, D. W., Evans, A. C., & Beaulieu, C. (2009). Mapping anatomical connectivity patterns of human cerebral cortex using in vivo diffusion tensor imaging tractography. *Cerebral Cortex*, *19*(3), 524–536.

Gonzalez, R. C., & Woods, R. E. (2006). *Digital image processing* (3rd ed). Prentice Hall.

Granger, C. W. J. (1969). Investigating causal relations by econometric models and cross-spectral methods. *Econometrica*, *37*(3), 424.

Granger, C. (1980). Testing for causality. *Journal of Economic Dynamics and Control*, *2*, 329–352.

Grech, R., Cassar, T., Muscat, J., Camilleri, K. P., Fabri, S. G., Zervakis, M., Xanthopoulos, P., Sakkalis, V., & Vanrumste, B. (2008). Review on solving the inverse problem in eeg source analysis. *Journal of NeuroEngineering and Rehabilitation*, *5*(1), 25.

Gross, J., Kujala, J., Hamalainen, M., Timmermann, L., Schnitzler, A., & Salmelin, R. (2001). Dynamic imaging of coherent sources: Studying neural interactions in the human brain. *Proceedings of the National Academy of Sciences*, *98*(2), 694–699.

Güllmar, D., Haueisen, J., & Reichenbach, J. R. (2010). Influence of anisotropic electrical conductivity in white matter tissue on the eeg/meg forward and inverse solution. a high-resolution whole head simulation study. *NeuroImage*, *51*(1), 145–163.

Haegens, S., Handel, B. F., & Jensen, O. (2011). Top-down controlled alpha band activity in somatosensory areas determines behavioral performance in a discrimination task. *Journal of Neuroscience*, *31*(14), 5197–5204.

Hallez, H., Vanrumste, B., Grech, R., Muscat, J., De Clercq, W., Vergult, A., D'Asseler, Y., Camilleri, K. P., Fabri, S. G., Van Huffel, S., & Lemahieu, I. (2007). Review on solving the forward problem in eeg source analysis. *Journal of NeuroEngineering and Rehabilitation*, *4*(1), 46.

Hämäläinen, M. S., & Ilmoniemi, R. J. (1994). Interpreting magnetic fields of the brain: Minimum norm estimates. *Medical & Biological Engineering & Computing*, *32*(1), 35–42.

Hämäläinen, M. S., & Ilmoniemi, R. J. (1984). *Interpreting measured magnetic fields of the brain: Estimates of current distributions*. Report TKK-F-A. Helsinki Univ. of Technology, Dep. of Technical Physics.

Hämäläinen, M., Hari, R., Ilmoniemi, R. J., Knuutila, J., & Lounasmaa, O. V. (1993). Magnetoencephalography — theory, instrumentation, and applications to noninvasive studies of the working human brain. *Reviews of Modern Physics*, *65*(2), 413–497.

Hassan, M., Dufor, O., Merlet, I., Berrou, C., Wendling, F., & D'Ausilio, A. (2014). Eeg source connectivity analysis: From dense array recordings to brain networks. *PLoS ONE*, *9*(8), 105041.

Haufe, S., Nikulin, V. V., Müller, K.-R., & Nolte, G. (2013). A critical assessment of connectivity measures for eeg data: A simulation study. *NeuroImage*, *64*, 120–133.

Haufe, S., Nikulin, V. V., & Nolte, G. (2012). Alleviating the influence of weak data asymmetries on granger-causal analyses. In F. Theis, A. Cichocki, A. Yeredor, & M. Zibulevsky (Eds.), *Latent variable analysis and signal separation* (Vol. 7191, pp. 25–33).

Haufe, S., Nikulin, V. V., Ziehe, A., Müller, K.-R., & Nolte, G. (2009). Estimating vector fields using sparse basis field expansions. In D. Koller, D. Schuurmans, Y. Bengio, & L. Bottou (Eds.), *Advances in neural information processing systems 21* (pp. 617–624). Curran Associates, Inc.

Haufe, S., Tomioka, R., Dickhaus, T., Sannelli, C., Blankertz, B., Nolte, G., & Müller, K.-R. (2011). Large-scale eeg/meg source localization with spatial flexibility. *NeuroImage*, *54*(2), 851–859.

Hauk, O., Wakeman, D. G., & Henson, R. (2011). Comparison of noise-normalized minimum norm estimates for meg analysis using multiple resolution metrics. *NeuroImage*, *54*(3), 1966–1974.

Hesse, W., Möller, E., Arnold, M., & Schack, B. (2003). The use of time-variant eeg granger causality for inspecting directed interdependencies of neural assemblies. *Journal of Neuroscience Methods*, *124*(1), 27–44.

Hillebrand, A., Barnes, G. R., Bosboom, J. L., Berendse, H. W., & Stam, C. J. (2012). Frequency-dependent functional connectivity within resting-state networks: An atlas-based meg beamformer solution. *NeuroImage*, *59*(4), 3909–3921.

Hillebrand, A., Tewarie, P., van Dellen, E., Yu, M., Carbo, E. W. S., Douw, L., Gouw, A. A., van Straaten, E. C. W., & Stam, C. J. (2016). Direction of information flow in large-scale resting-state networks is frequency-dependent. *Proceedings of the National Academy of Sciences*, *113*(14), 3867–3872.

Hincapié, A.-S., Kujala, J., Mattout, J., Daligault, S., Delpuech, C., Mery, D., Cosmelli, D., & Jerbi, K. (2016). Meg connectivity and power detections with minimum norm estimates require different regularization parameters. *Computational Intelligence and Neuroscience*, *2016*, 1–11.

Holmes, C. J., Hoge, R., Collins, L., Woods, R., Toga, A. W., & Evans, A. C. (1998). Enhancement of mr images using registration for signal averaging. *Journal of Computer Assisted Tomography*, *22*(2), 324–333.

Hosek, R. S., Sances, A., Jodat, R. W., & Larson, S. J. (1978). The contributions of intracerebral currents to the eeg and evoked potentials. *IEEE Transactions on Biomedical Engineering*, *BME-25*(5), 405–413.

Huang, Y., Parra, L. C., & Haufe, S. (2016). The new york head—a precise standardized volume conductor model for eeg source localization and tes targeting. *NeuroImage*, *140*, 150–162.

Iordanov, T., Hoechstetter, K., & Berg, P. (2014). Clara: Classical loreta analysis recursively applied. 5:895 (poster).

Iturria-Medina, Y., Sotero, R. C., Canales-Rodríguez, E. J., Alemán-Gómez, Y., & Melie-García, L. (2008). Studying the human brain anatomical network via diffusion-weighted mri and graph theory. *NeuroImage*, *40*(3), 1064–1076.

Jensen, O., & Mazaheri, A. (2010). Shaping functional architecture by oscillatory alpha activity: Gating by inhibition. *Frontiers in Human Neuroscience*, *4*.

Jurcak, V., Tsuzuki, D., & Dan, I. (2007). 10/20, 10/10, and 10/5 systems revisited: Their validity as relative head-surface-based positioning systems. *NeuroImage*, *34*(4), 1600–1611.

Kamiński, M. J., & Blinowska, K. J. (1991). A new method of the description of the information flow in the brain structures. *Biological Cybernetics*, *65*(3), 203–210.

Kamiński, M., & Liang, H. (2005). Causal influence: Advances in neurosignal analysis. *Critical Reviews in Biomedical Engineering*, *33*(4), 347–430.

Klimesch, W., Sauseng, P., & Hanslmayr, S. (2007). Eeg alpha oscillations: The inhibition–timing hypothesis. *Brain Research Reviews*, *53*(1), 63–88.

Kolb, B., & Whishaw, I. Q. (1990). *Fundamentals of human neuropsychology* (3rd ed.). A Series of books in psychology. Freeman.

Korzeniewska, A., Mańczak, M., Kamiński, M., Blinowska, K. J., & Kasicki, S. (2003). Determination of information flow direction among brain structures by a modified directed transfer function (ddtf) method. *Journal of Neuroscience Methods*, *125*(1-2), 195–207.

Kovac, S., Chaudhary, U. J., Rodionov, R., Mantoan, L., Scott, C. A., Lemieux, L., Wehner, T., Scherg, M., & Diehl, B. (2014). Ictal eeg source imaging in frontal lobe epilepsy leads to improved lateralization compared with visual analysis. *Journal of Clinical Neurophysiology*, *31*(1), 10–20.

Kuś, R., Kamiński, M., & Blinowska, K. J. (2004). Determination of eeg activity propagation: Pair-wise versus multichannel estimate. *IEEE transactions on bio-medical engineering*, *51*(9), 1501–1510.

Lachaux, J.-P., Rodriguez, E., Martinerie, J., & Varela, F. J. (1999). Measuring phase synchrony in brain signals. *Human Brain Mapping*, *8*(4), 194–208.

Lantz, G., Grave de Peralta, R., Spinelli, L., Seeck, M., & Michel, C. (2003). Epileptic source localization with high density eeg: How many electrodes are needed? *Clinical Neurophysiology*, *114*(1), 63–69.

Lin, F.-H., Witzel, T., Hämäläinen, M. S., Dale, A. M., Belliveau, J. W., & Stufflebeam, S. M. (2004). Spectral spatiotemporal imaging of cortical oscillations and interactions in the human brain. *NeuroImage*, *23*(2), 582–595.

Linkenkaer-Hansen, K., Nikouline, V. V., Palva, J. M., & Ilmoniemi, R. J. (2001). Long-range temporal correlations and scaling behavior in human brain oscillations. *The Journal of Neuroscience*, *21*(4), 1370–1377.

Liu, A. K., Belliveau, J. W., & Dale, A. M. (1998). Spatiotemporal imaging of human brain activity using functional mri constrained magnetoencephalography data: Monte carlo simulations. *Proceedings of the National Academy of Sciences*, *95*(15), 8945–8950.

Liu, H., Schimpf, P. H., Dong, G., Gao, X., Yang, F., & Gao, S. (2005). Standardized shrinking loreta-focuss (sslofo): A new algorithm for spatio-temporal eeg source reconstruction. *IEEE Transactions on Biomedical Engineering*, *52*(10), 1681–1691.

Lobier, M., Siebenhühner, F., Palva, S., & Palva, J. M. (2014). Phase transfer entropy: A novel phase-based measure for directed connectivity in networks coupled by oscillatory interactions. *NeuroImage*, *85*, 853–872.

Logothetis, N. K., & Wandell, B. A. (2004). Interpreting the bold signal. *Annual Review of Physiology*, *66*(1), 735–769.

Mahjoory, K., Nikulin, V. V., Botrel, L., Linkenkaer-Hansen, K., Fato, M. M., & Haufe, S. (2017). Consistency of eeg source localization and connectivity estimates.

Mantini, D., Perrucci, M. G., Del Gratta, C., Romani, G. L., & Corbetta, M. (2007). Electrophysiological signatures of resting state networks in the human brain. *Proceedings of the National Academy of Sciences*, *104*(32), 13170–13175.

Marinazzo, D., Pellicoro, M., & Stramaglia, S. (2006). Nonlinear parametric model for granger causality of time series. *Physical Review E*, *73*(6).

Michel, C. M., & Brunet, D. (2019). Eeg source imaging: A practical review of the analysis steps. *Frontiers in Neurology*, *10*.

Mosher, J., & Leahy, R. (1999). Source localization using recursively applied and projected (rap) music. *IEEE Transactions on Signal Processing*, *47*(2), 332–340.

Mosher, J., Lewis, P., & Leahy, R. (1992). Multiple dipole modeling and localization from spatio-temporal meg data. *IEEE Transactions on Biomedical Engineering*, *39*(6), 541–557.

Niedzwiecki, M., & Ciolek, M. (2017). Akaike's final prediction error criterion revisited. (pp. 237–242).

Nolte, G., Bai, O., Wheaton, L., Mari, Z., Vorbach, S., & Hallett, M. (2004). Identifying true brain interaction from eeg data using the imaginary part of coherency. *Clinical Neurophysiology*, *115*(10), 2292–2307.

Nolte, G., Ziehe, A., Nikulin, V. V., Schlögl, A., Krämer, N., Brismar, T., & Müller, K.-R. (2008). Robustly estimating the flow direction of information in complex physical systems. *Physical Review Letters*, *100*(23).

Nunez, P. L., Srinivasan, R., Westdorp, A. F., Wijesinghe, R. S., Tucker, D. M., Silberstein, R. B., & Cadusch, P. J. (1997). Eeg coherency. i: Statistics, reference electrode, volume conduction, laplacians, cortical imaging, and interpretation at multiple scales. *Electroencephalography and Clinical Neurophysiology*, *103*(5), 499–515.

Nunez, P. L., & Srinivasan, R. (2006). *Electric fields of the brain: The neurophysics of eeg* (2nd ed.). Oxford University Press.

Oostenveld, R., & Praamstra, P. (2001). The five percent electrode system for high-resolution eeg and erp measurements. *Clinical Neurophysiology: Official Journal of the International Federation of Clinical Neurophysiology*, *112*(4), 713–719.

Oostenveld, R., Fries, P., Maris, E., & Schoffelen, J.-M. (2011). Fieldtrip: Open source software for advanced analysis of meg, eeg, and invasive electrophysiological data. *Computational Intelligence and Neuroscience*, *2011*, 1–9.

Palva, S., & Palva, J. M. (2012). Discovering oscillatory interaction networks with m/eeg: Challenges and breakthroughs. *Trends in Cognitive Sciences*, *16*(4), 219–230.

Papadelis, C., Chen, Z., Kourtidou-Papadeli, C., Bamidis, P. D., Chouvarda, I., Bekiaris, E., & Maglaveras, N. (2007). Monitoring sleepiness with on-board electrophysiological recordings for preventing sleep-deprived traffic accidents. *Clinical Neurophysiology*, *118*(9), 1906–1922.

Papp, N., & Ktonas, P. (1977). Critical evaluation of complex demodulation techniques for the quantification of bioelectrical activity. *Biomedical Sciences Instrumentation*, *13*, 135–145.

Pascual-Marqui, R., Michel, C., & Lehmann, D. (1994). Low resolution electromagnetic tomography: A new method for localizing electrical activity in the brain. *International Journal of Psychophysiology*, *18*(1), 49–65.

Pascual-Marqui, R. D. (2007). Discrete, 3d distributed, linear imaging methods of electric neuronal activity. part 1: Exact, zero error localization. *arXiv:0710.3341 Math-Ph Physicsphysics Q-Bio*. arXiv: 0710.3341.

Pascual-Marqui, R. D., Biscay, R. J., Bosch-Bayard, J., Lehmann, D., Kochi, K., Kinoshita, T., Yamada, N., & Sadato, N. (2014). Assessing direct paths of intracortical causal information flow of oscillatory activity with the isolated effective coherence (icoh). *Frontiers in Human Neuroscience*, *8*.

Ploner, M., Gross, J., Timmermann, L., Pollok, B., & Schnitzler, A. (2006). Pain suppresses spontaneous brain rhythms. *Cerebral Cortex*, *16*(4), 537–540.

Plonsey, R., & Heppner, D. B. (1967). Considerations of quasi-stationarity in electrophysiological systems. *The Bulletin of Mathematical Biophysics*, *29*(4), 657–664.

Press, W. H., Teukolsky, S. A., Vetterling, W. T., & Flannery, B. P. (2007). *Numerical recipes 3rd edition: The art of scientific computing* (3rd ed.). Cambridge University Press.

Prichard, D., & Theiler, J. (1994). Generating surrogate data for time series with several simultaneously measured variables. *Physical Review Letters*, *73*(7), 951–954.

Richards, J. E., & Xie, W. (2015). Brains for all the ages. In *Advances in child development and behavior* (Vol. 48, pp. 1–52).

Romei, V., Brodbeck, V., Michel, C., Amedi, A., Pascual-Leone, A., & Thut, G. (2008). Spontaneous fluctuations in posterior -band eeg activity reflect variability in excitability of human visual areas. *Cerebral Cortex*, *18*(9), 2010–2018.

Sarvas, J. (1987). Basic mathematical and electromagnetic concepts of the biomagnetic inverse problem. *Physics in Medicine and Biology*, *32*(1), 11–22.

Scherg, M. (1990). Fundamentals of dipole source potential analysis. In *Auditory evoked magnetic fields and electric potentials* (Vol. 6, pp. 40–69). Advances in Audiology. Karger.

Scherg, M., & Berg, P. (1996). New concepts of brain source imaging and localization. *Electroencephalography and Clinical Neurophysiology. Supplement*, *46*, 127–137.

Scherg, M., & Ebersole, J. S. (1993). Models of brain sources. *Brain Topography*, *5*(4), 419–423.

Scherg, M., Bast, T., Hoechstetter, K., Ille, N., Weckesser, D., Bornfleth, H., & Berg, P. (2004). Brain source montages improve the non-invasive diagnosis in epilepsy. *International Congress Series*, *1270*, 15–19.

Scherg, M. (1992). Functional imaging and localization of electromagnetic brain activity. *Brain Topography*, *5*(2), 103–111.

Scherg, M., Ille, N., Bornfleth, H., & Berg, P. (2002). Advanced tools for digital eeg review: Virtual source montages, whole-head mapping, correlation, and phase analysis. *Journal of Clinical Neurophysiology: Official Publication of the American Electroencephalographic Society*, *19*(2), 91–112.

Schlögl, A. (2006). A comparison of multivariate autoregressive estimators. *Signal Processing*, *86*(9), 2426–2429.

Schoffelen, J.-M., & Gross, J. (2009). Source connectivity analysis with meg and eeg. *Human Brain Mapping*, *30*(6), 1857–1865.

Schreiber, T. (2000). Measuring information transfer. *Physical Review Letters*, *85*(2), 461–464.

Schreiber, T., & Schmitz, A. (2000). Surrogate time series. *Physica D: Nonlinear Phenomena*, *142*(3–4), 346–382.

Schubert, R., Haufe, S., Blankenburg, F., Villringer, A., & Curio, G. (2009). Now you'll feel it, now you won't: Eeg rhythms predict the effectiveness of perceptual masking. *Journal of Cognitive Neuroscience*, *21*(12), 2407–2419.

Schwarz, G. (1978). Estimating the dimension of a model. *The Annals of Statistics*, *6*(2), 461–464.

Sekihara, K., & Nagarajan, S. S. (2008). Output snr and array mismatch. In *Adaptive spatial filters for electromagnetic brain imaging* (pp. 83–107).

Shannon, C. E., & Weaver, W. (1949). *The mathematical theory of communication* (1st ed.). University of Illinois Press.

Shibasaki, H. (2008). Human brain mapping: Hemodynamic response and electrophysiology. *Clinical Neurophysiology*, *119*(4), 731–743.

Silfverhuth, M. J., Hintsala, H., Kortelainen, J., & Seppänen, T. (2012). Experimental comparison of connectivity measures with simulated eeg signals. *Medical & Biological Engineering & Computing*, *50*(7), 683–688.

Simon, M., Schmidt, E. A., Kincses, W. E., Fritzsche, M., Bruns, A., Aufmuth, C., Bogdan, M., Rosenstiel, W., & Schrauf, M. (2011). Eeg alpha spindle measures as indicators of driver fatigue under real traffic conditions. *Clinical Neurophysiology*, *122*(6), 1168–1178.

Snyder, A. C., & Foxe, J. J. (2010). Anticipatory attentional suppression of visual features indexed by oscillatory alpha-band power increases:a high-density electrical mapping study. *Journal of Neuroscience*, *30*(11), 4024–4032.

Song, J., Davey, C., Poulsen, C., Luu, P., Turovets, S., Anderson, E., Li, K., & Tucker, D. (2015). Eeg source localization: Sensor density and head surface coverage. *Journal of Neuroscience Methods*, *256*, 9–21.

Spiegler, A., Knösche, T. R., Schwab, K., Haueisen, J., & Atay, F. M. (2011). Modeling brain resonance phenomena using a neural mass model. *PLoS Computational Biology*, *7*(12).

Sporns, O. (2013). Network attributes for segregation and integration in the human brain. *Current Opinion in Neurobiology*, *23*(2), 162–171.

Stam, C. J., & Reijneveld, J. C. (2007). Graph theoretical analysis of complex networks in the brain. *Nonlinear Biomedical Physics*, *1*(1), 3.

Steinsträter, O., Sillekens, S., Junghoefer, M., Burger, M., & Wolters, C. H. (2010). Sensitivity of beamformer source analysis to deficiencies in forward modeling. *Human Brain Mapping*, *31*(12), 1907–1927.

Suarez, E., Viegas, M. D., Adjouadi, M., & Barreto, A. (2000). Relating induced changes in eeg signals to orientation of visual stimuli using the esi-256 machine. *Biomedical Sciences Instrumentation*, *36*, 33–38.

Theiler, J., Eubank, S., Longtin, A., Galdrikian, B., & Doyne Farmer, J. (1992). Testing for nonlinearity in time series: The method of surrogate data. *Physica D: Nonlinear Phenomena*, *58*(1–4), 77–94.

Tikhonov, A. N., Leonov, A. S., & Yagola, A. G. (1998). *Nonlinear ill-posed problems*. Chapman & Hall.

Tononi, G. (1998). Consciousness and complexity. *Science*, *282*(5395), 1846–1851.

Tononi, G., Sporns, O., & Edelman, G. M. (1994). A measure for brain complexity: Relating functional segregation and integration in the nervous system. *Proceedings of the National Academy of Sciences*, *91*(11), 5033–5037.

Trujillo, L. T., Stanfield, C. T., & Vela, R. D. (2017). The effect of electroencephalogram (eeg) reference choice on information-theoretic measures of the complexity and integration of eeg signals. *Frontiers in Neuroscience*, *11*.

Tzourio-Mazoyer, N., Landeau, B., Papathanassiou, D., Crivello, F., Etard, O., Delcroix, N., Mazoyer, B., & Joliot, M. (2002). Automated anatomical labeling of activations in spm using a macroscopic anatomical parcellation of the mni mri single-subject brain. *NeuroImage*, *15*(1), 273–289.

Ursino, M., Zavaglia, M., Astolfi, L., & Babiloni, F. (2007). Use of a neural mass model for the analysis of effective connectivity among cortical regions based on high resolution eeg recordings. *Biological Cybernetics*, *96*(3), 351–365.

Van Veen, B., Van Drongelen, W., Yuchtman, M., & Suzuki, A. (1997). Localization of brain electrical activity via linearly constrained minimum variance spatial filtering. *IEEE Transactions on Biomedical Engineering*, *44*(9), 867–880.

van Vliet, M., Liljeström, M., Aro, S., Salmelin, R., & Kujala, J. (2018). Analysis of functional connectivity and oscillatory power using dics: From raw meg data to group-level statistics in python. *Frontiers in Neuroscience*, *12*.

Vander, A. J., Sherman, J. H., & Luciano, D. S. (2001). *Human physiology: The mechanisms of body function* (8th ed.). McGraw-Hill.

Vinck, M., Huurdeman, L., Bosman, C. A., Fries, P., Battaglia, F. P., Pennartz, C. M., & Tiesinga, P. H. (2015). How to detect the granger-causal flow direction in the presence of additive noise? *NeuroImage*, *108*, 301–318.

Vinck, M., Oostenveld, R., van Wingerden, M., Battaglia, F., & Pennartz, C. M. (2011). An improved index of phase-synchronization for electrophysiological data in the presence of volume-conduction, noise and sample-size bias. *NeuroImage*, *55*(4), 1548–1565.

Wang, S. H., Lobier, M., Siebenhühner, F., Puoliväli, T., Palva, S., & Palva, J. M. (2018). Hyperedge bundling: A practical solution to spurious interactions in meg/eeg source connectivity analyses. *NeuroImage*, *173*, 610–622.

Weisz, N., Hartmann, T., Müller, N., Lorenz, I., & Obleser, J. (2011). Alpha rhythms in audition: Cognitive and clinical perspectives. *Frontiers in Psychology*, *2*.

Welch, P. (1967). The use of fast fourier transform for the estimation of power spectra: A method based on time averaging over short, modified periodograms. *IEEE Transactions on Audio and Electroacoustics*, *15*(2), 70–73.

Wen, Q., & Chklovskii, D. B. (2005). Segregation of the brain into gray and white matter: A design minimizing conduction delays. *PLoS Computational Biology*, *1*(7), e78.

Wendling, F., Bartolomei, F., Bellanger, J. J., & Chauvel, P. (2002). Epileptic fast activity can be explained by a model of impaired gabaergic dendritic inhibition: Epileptic activity explained by dendritic dis-inhibition. *European Journal of Neuroscience*, *15*(9), 1499–1508.

Wiener, N. (1956). The theory of prediction: Modern mathematics for the engineer. In E. F. Beckenbach (Ed.). McGraw-Hill.

Wilson, G. T. (1972). The factorization of matricial spectral densities. *SIAM Journal on Applied Mathematics*, *23*(4), 420–426.

Winkler, I., Panknin, D., Bartz, D., Müller, K.-R., & Haufe, S. (2016). Validity of time reversal for testing granger causality. *IEEE Transactions on Signal Processing*, *64*(11), 2746–2760. arXiv: 1509.07636.

Winterhalder, M., Schelter, B., Hesse, W., Schwab, K., Leistritz, L., Klan, D., Bauer, R., Timmer, J., & Witte, H. (2005). Comparison of linear signal processing techniques to

infer directed interactions in multivariate neural systems. *Signal Processing*, *85*(11), 2137–2160.

Wolters, C., Anwander, A., Tricoche, X., Weinstein, D., Koch, M., & MacLeod, R. (2006). Influence of tissue conductivity anisotropy on eeg/meg field and return current computation in a realistic head model: A simulation and visualization study using high-resolution finite element modeling. *NeuroImage*, *30*(3), 813–826.

Wu, M.-H., Frye, R. E., & Zouridakis, G. (2011). A comparison of multivariate causality based measures of effective connectivity. *Computers in Biology and Medicine*, *41*(12), 1132–1141.

Xue, G., Chen, C., Lu, Z.-L., & Dong, Q. (2010). Brain imaging techniques and their applications in decision-making research: Brain imaging techniques and their applications in decision-making research. *Acta Psychologica Sinica*, *42*(1), 120–137.

Yan, Y., Nunez, P. L., & Hart, R. T. (1991). Finite-element model of the human head: Scalp potentials due to dipole sources. *Medical & Biological Engineering & Computing*, *29*(5), 475–481.

Zeki, S., & Shipp, S. (1988). The functional logic of cortical connections. *Nature*, *335*(6188), 311–317.

Zeki, S., Watson, J. D., Lueck, C. J., Friston, K. J., Kennard, C., & Frackowiak, R. (1991). A direct demonstration of functional specialization in human visual cortex. *The Journal of Neuroscience*, *11*(3), 641–649.